Synthesis and Characterization of Solid Solutions of $M_{(N+1)}AX_N$ Phases

A Thesis

Submitted to the Faculty

of

Drexel University

by

Adrish Ganguly

in partial fulfillment of the

requirements for the degree

of

Doctor of Philosophy

February 2006

Dedications

To my parents, Sri Dilip Kumar Ganguly, Srimati Manjusha Ganguly and my grandfather, Late, Sri Satyendra Chandra Bhattacharjee, who always believed that I could achieve everything I wished for. You have sacrificed a lot to see me get to where I am today and for that I will be forever grateful.

Acknowledgements

It is difficult if not impossible at this moment, to find appropriate words to express my gratitude to my advisor **Dr. Michel W. Barsoum** for his encouragement, continuous support, great teaching, friendly advice, inspiration and his faith in me. Thus I can simply say: THANK YOU.I have been very fortunate to learn from him so much working on my thesis.

I consider myself lucky and honored for having an opportunity to collaborate with a lot of wonderful people during my work on PhD Thesis. Among all of them, I would like specially to thanks:

- **Dr. Roger Doherty, Dr. Yuri Gogotsi**, Drexel University, **Dr. Jeffrey Hettinger**, Rowan University and **Dr. Peter Finkel**, Thomson Consumer Electronics, for their time and interest in reviewing this thesis and participating in my defense committee;
- **Dr. Miladin Radovic,** from Oak Ridge National Laboratory, Oak Ridge, TN for helping me to interpret experimental results, illuminating discussions and great suggestions;
- **Dr. Manoun Bouchaib,** from Florida International University for carrying out the compressibility experiments.
- **Dr. Sam Lofland** and **Mr. Ted Scabarozi**, Rowan University, for helping me with the measurements on the low temperature electronic properties and inspiriting discussions.
- **Dr. T. El-Raghy** for many illuminating discussions and fruitful suggestions.

- **Mr. David Vohn Rohr** and **Mrs. Dee Breger**, Drexel University, for their great help with microscopy.
- **Dr. Tiejun Zhen** and **Mr. Aiguo Zhou**, for their help with the servo hydraulic MTS machine.
- **Mr. Mark Shiber**, Drexel University, for doing the great job in machining the testing samples;
- **Mrs. Judy Trechtman**, **Mrs. Crystal White** and **Mrs. Dorilona Rose**, Drexel University, for their great help in solving everyday problems, friendly advice and support;
- All **Faculty members** of the **Materials Science and Engineering Department**, Drexel University;
- My fellow **graduate students** in the **Materials Science and Engineering Department** at Drexel University for making this work an enjoyable and unforgettable experience. Sincere thanks are due to my fellow research colleagues **Dr. A Murugaiah**, **Mr. S. Gupta, Mr. S. Basu** and **Mrs. E.N. Hoffman**.

Finally, I would like to thank my parents, **Sri Dilip Kumar Ganguly** and **Srimati Manjusha Ganguly** for their comprehension, help and relentless support through all these years. Without their help, this work would not have been possible.

Philadelphia Adrish Ganguly

February 10, 2006

Table of Contents

List of Tables

List of Figures

Abstract

Synthesis and Characterization of Solid Solutions of MAX Phases

Adrish Ganguly

Advisor-Michel Barsoum, Ph. D.

The MAX phases, best described as polycrystalline nanolaminates, deserve attention in today's world because they combine some of the best properties of ceramics and metals. While considerable work exists on selective MAX phases, to date, little is known about MAX solid solutions. This work is focused on the synthesis and characterization of A- or X-site substituted MAX solid solutions.

In general, substitutions on the A sites led, either to solid solution softening or to a monotonic change in properties from one end member to the other. The Vickers microhardness values of the solid solution compositions were in between those of the end members, indicating that no hardening is operative in these systems. Substitutions on the A-sites resulted in a reduction in the residual resistivity ratios and the phonon conductivities as compared to the end members, indicating that solid solution scattering of both phonons and electrons was occurring.

Substitutions on the X sites, on the other hand, resulted in an increase in the elastic moduli and a concomitant reduction in the coefficients of thermal expansion with respect to the end members. This behavior, combined with the higher values of Vickers microhardness clearly indicated solid solution hardening. Somewhat surprisingly, the phonon conductivities of $Ti_3Al(C_{0.5}N_{0.5})_2$ and $Ti_2AlC_{0.5}N_{0.5}$ were higher than the

respective end members. This enhancement was attributed to the stiffening of the structure as reflected in the higher shear moduli than that of the end members.

All the MAX phases tested herein were kinking nonlinear elastic solids. Substitutions on the X-sites significantly influenced the nonlinear kinking behavior under compression. The threshold stress (σ_c) required for kinking and the critical resolved shear stresses needed for dislocations to glide along the basal planes were observed to increase considerably for the solid solutions compared to the end members. The effects of substitutions on the A-sites on the kinking behavior were quite mild relative to those of the X-site substitutions.

1: Introduction

1.1 Background

It is well known that if the average engine temperature of the world's jet engine could be increased by 1 ºC, the fuel savings alone would be worth $1 billon per year. This is due to the simple fact that the efficiency of any fuel burning engine is directly proportional to its operating temperature. A jet engine made from a material 50 percent lighter in weight and able to run 200 to 300 degrees hotter could have a staggering economic impact.

No material is known till date, which can take that kind of heat while spinning furiously. Same holds true for an internal combustion engine; if an automobile engine could be built with a temperature-tolerant material, its radiator, water pump and cooling water could be thrown away. Such an efficient, lighter and higher-temperature engine would squeeze more miles from every gallon of fuel.

By now, it has been well established that above 1000 ºC even the best metal alloys turn into taffy and become useless for load-bearing applications. Building hotter engines would require employing another class of materials, namely ceramics. Even though there has been undeniable progress, the wide use of ceramics in aerospace and automotive industries remains elusive. However, the good high temperature properties of ceramics came at the price of poor machinability, brittleness and hardness, which limited their wide applications. Hence, the need for new high temperature materials, that are easily machinable, relatively soft with respectable high temperature properties is still of considerable interest.

In the last two decades, the ternary compound Ti_3SiC_2 was reported as an interesting material that could be the desired “ductile ceramics”. Due to the difficulties in fabricating monolithic, bulk and dense samples of Ti_3SiC_2, very little was known about the material. In 1995, Barsoum and Raghy synthesized for the first time bulk, dense samples of Ti_3SiC_2 and performed extensive characterization of its properties. It was found that the compound has a combination of properties of both metals and ceramics. Like metals it is machinable, thermally and electrically conductive, resistant to thermal shock and plastic at elevated temperatures. Like a ceramic it is refractory (its decomposition temperature is greater than 2,000 ºC), oxidation resistant, quite stiff and relatively light (4.5 g/c.c). Its thermal expansion is relatively small like that of typical ceramics rather than that of metals.

Barsoum and his research group at Drexel University soon identified more than 50 closely related compounds (Fig. 1.1). As a class, they are best described as a unique class of thermodynamically stable polycrystalline nanolaminates, popularly known as $M_{(n+1)}AX_n$ phases (n=1 to 3); M-early transition metal, A-Group III A/IV A element, X-Carbon or Nitrogen.

MAX Phases : M – Early transitional metal (red)
A – Group IIIA /IVA element (blue)
X – Nitrogen / Carbon (black)

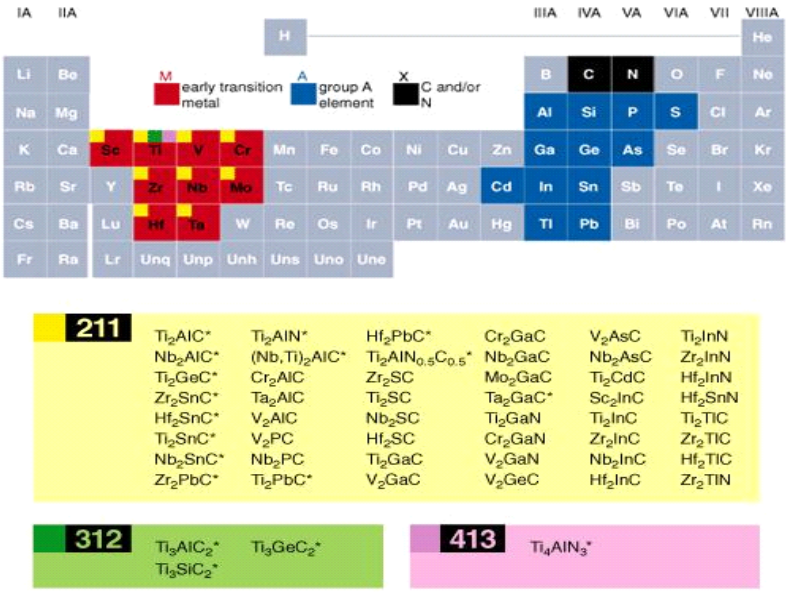

Figure 1.1: The MAX phases are made up of an early transition metal M (*red*) in the periodic table, an element from the A groups, usually IIIA and IVA *(dark blue*), and a third element, X, which is either nitrogen or carbon (*black*), in the composition $M_{n+1}AX_n$, where n is 1, 2 or 3. The classes of materials characterized to date naturally form into three groups, based on the number of atoms of the M, A and X elements in each molecule; these groups are known as 211, 312 and 413 materials. The one's that are marked with asterisks have been synthesized successfully by Dr. Barsoum's research group at Drexel University.

The $M_{(n+1)}AX_n$ phases are layered hexagonal (space group D^4_{6h}-$P6_3/mmc$) with two formula units per unit cell. Figures 1.2 a, b and c compare the unit cells of the 211, 312 and 413 phases, respectively [1]. In each case near close packed layers of M layers are interleaved with layers of pure A-group element, with the X atoms filling

the octahedral sites between the former. The A-group elements are located at the center of trigonal prisms that are larger than the octahedral sites and thus better able to accommodate the larger A- atoms. The M_6X octahedra are edge sharing and are identical to those found in the rock salt structure of the corresponding binary carbides. The main difference between the structures shown in Fig. 1.2 is in the number of M layers separating the A-layers: in the 211's there are two; in the 312's three, and in the 413's four. This layered nature is of fundamental importance in understating many of the unusual attributes of MAX phases.

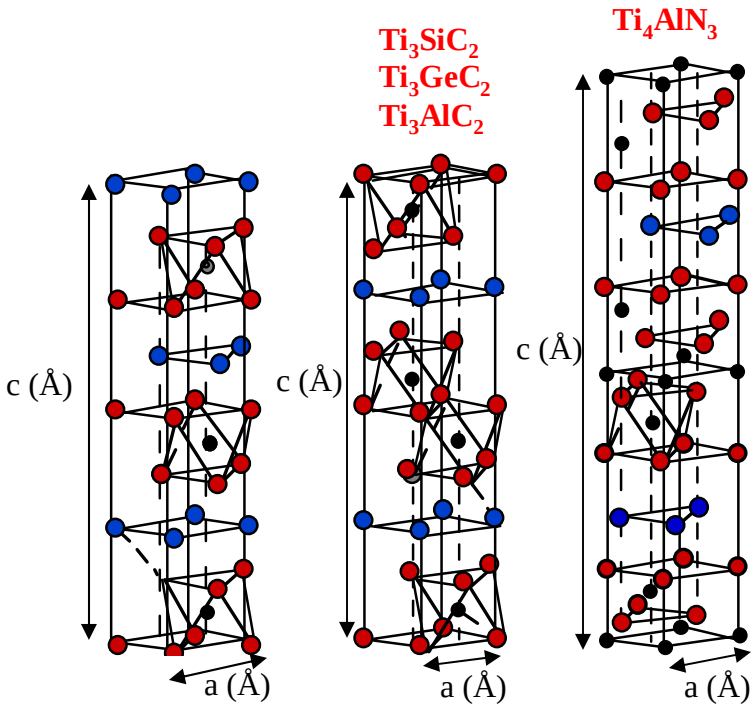

Figure 1.2: Unit cells of (a) 211 (b) 312 and (c) 413 phases. M (*red*) is the early transition metal, A- A groups, usually IIIA and IVA *(dark blue*), and X- either nitrogen or carbon (*black*).

1.2 Objective and scope of this work

This work is focused on the effect of substitution on the A or X site in these ternaries. By replacing Si by Ge in the Ti_3SiC_2- Ti_3GeC_2 system one can understand the effect of the change of atomic radii of the A- group elements, while by substituting Si by Al in the Ti_3SiC_2- Ti_3AlC_2 system one can not only observe the effect of change of atomic radii but also the effect of adding one extra valence electron on material properties. The latter holds true for the X site substitution: replacing N by C affects the material properties due to change in atomic radii and in number of valence electrons of the X group elements. The aim of this work is to study the effect on the material properties in these ternaries as a function of composition, thus providing a better understanding of how to tailor the properties of these novel materials depending on suitable applications.

The thesis is a collection of published, accepted for publication (chapter 2, part of 3, 4, 5, 6 and chapter 7) or in preparation papers (part of chapter 3, 4, 5 and 8). Chapter 2 describes in detail the results of synthesis and microstructural characterizations of Ti_3GeC_2 and $Ti_3Si_{0.5}Ge_{0.5}C_2$, $Ti_3Si_{0.75}Ge_{0.25}C_2$, $Ti_3Si_{0.5}Al_{0.5}C_2$ (A-site substituted solid solutions), $Ti_3Al(C_{0.5}N_{0.5})_2$ and $Ti_2Al(C_{0.5}N_{0.5})$ (X-site substituted solid solutions). Chapter 3 discusses the physical properties (compressibility, elastic properties and thermal expansion coefficients) and chapter 4 describes the low temperature electronic properties of the same. Chapter 5 describes the mechanical properties; the effect of substitution on high temperature deformation, damage tolerance and thermal shock. Chapter 6 deals with the nonlinear kinking behavior of the MAX solid

solutions. Chapter 7 reports on the damping properties of these solid solution compositions. Finally chapter 8 proposes some recommendations for future work. Appendix A investigates the effect of composition on the interdiffusion coefficients in the 312 and 211 system.

The compressibility measurements reported in chapter 3 was carried out by B. Manoun in Florida International University, FL. The data on the elastic properties and damping, reported in the Chs. 4 and 7, respectively, were collected by M. Radovic of Oak Ridge National Laboratory, while the author analyzed the results. The measurements on the low temperature electronic properties were conducted by Scabarozi, Finkel and Hettinger at Rowan University, NJ.

2: Synthesis and Microstructural Characterization of A or X- site Substituted Solid Solutions and Ti_3GeC_2

2.1 Introduction

Of the more than 50 known $M_{n+1}AX_n$ phases, only three are M_3AX_2: Ti_3SiC_2, Ti_3GeC_2 and Ti_3AlC_2. Jeitschko and Nowotny [2] were the first to synthesize powders of, and decipher the structure of, Ti_3SiC_2. However, predominantly single phase samples of Ti_3SiC_2 have only been available relatively recently [3]. This material has the density of Ti, but is roughly three times as stiff (325 GPa) [3, 4] and yet is most readily machinable (even by manual hacksaw). It is stable to inert atmospheres to temperatures upto 2200 ºC [5]. It is fatigue [6] and thermal shock resistant [1, 6], as well as relatively tough K_{IC} = 8-16 MPa $m^{1/2}$ depending on grain size and temperature) [7]. It is more than twice as conductive as Ti metal, both electrically and thermally [1, 8].

The ternary, Ti_3AlC_2 was discovered in the early 90's [9, 10] and has only recently been characterized [11, 12]. In general, its properties are comparable to those of Ti_3SiC_2. Even less is known about Ti_3GeC_2. It was first synthesized in powder form by Wolfsgruber et al. [13] who showed it to be isostructural with Ti_3SiC_2. Its theoretical density is 5.55 Mg m^{-3}. It is readily machinable and relatively soft (Vickers Hardness ~ 5 GPa [14]). Its electrical conductivity at room temperature is nearly identical to that of Ti_3SiC_2 (~ 4.5×10^6 Ω^{-1} m^{-1}) [11, 14]. The room temperature compressive strength of fine-grained samples of Ti_3GeC_2 is ~ 1.2 GPa [14, 15]. Like Ti_3SiC_2 and Ti_3AlC_2, Ti_3GeC_2 exhibits a brittle to ductile transition temperature around 1100 ºC. Prior to this work there were no reports on the thermal shock, damage tolerance and stiffness of Ti_3GeC_2.

2.1.1 Solid Solution Compositions

2.1.1.1 Substitution on the A-Site

Very recently, the existence of solid solubility between Ti_3SiC_2 and Ti_3AlC_2 has been reported by Wang et al. [16] and Zhou et al [17]. The first principle calculations preformed by Wang et al. demonstrated that the solid solution with the composition of $Ti_3Si_{0.75}Al_{0.25}C_2$ was stable. The range of solubilities studied in the solid solution $Ti_3Si_{(1-x)}Al_xC_2$ system by Zhou et al. was in between x = 0.01 to 0.15. The mechanical properties (Vickers hardness, flexural strength) of Al doped Ti_3SiC_2 were reported to be comparable to those of Ti_3SiC_2, but higher than those of Ti_3AlC_2. However, currently in an article in press Zhou et al. [18] have claimed that significant strengthening occurs in the $Ti_3Si_{(1-x)}Al_xC_2$ system when x was greater than 0.15. The Vickers hardness, flexural strength and compressive strength for the composition $Ti_3Si_{0.75}Al_{0.25}C_2$ were reported to be enhanced by 26%, 12% and 29% respectively, over pure Ti_3SiC_2.

2.1.1.2 Substitution on the X-Site

The structure of Ti_2AlC [19] and Ti_2AlN [20] was first reported in the early 1960s by Jeitschko et al. However, the synthesis of predominantly single-phase, bulk samples was achieved only much later [21, 22]. Like Ti_3SiC_2, Ti_2AlC and Ti_2AlN were found to be relatively soft (3 to 6 GPa) and readily machinable [22]. Pietzka and Schuster were the first to report the existence of a continuous series of solid solutions, $Ti_2AlC_{0.8-x}N_x$, where x = 0 to 0.8 at 1490 ºC [23]. Barsoum et al. [22] reported on the bulk synthesis and characterization of $Ti_2AlC_{0.5}N_{0.5}$ for the first time. Solid solution hardening was found to

be operative in the system at room temperature. While the existence of Ti_2AlC, Ti_2AlN and $Ti_2Al(C_{0.5},N_{0.5})$ is documented, Ti_3AlN_2 does not exist despite the fact that Ti_4AlN_3 does [24, 25, 26].

To date no report exists on the synthesis of $Ti_3Si_{0.5}Al_{0.5}C_2$, $Ti_3Si_{0.5}Ge_{0.5}C_2$ or $Ti_3Al(C_{0.5}N_{0.5})_2$. This work, for the first time, reports on the synthesis of solid solution in the Ti_3AlC_2–Ti_3AlCN and Ti_3SiC_2-Ti_3GeC_2/ Ti_3AlC_2 systems respectively, and claims for the first time that a solid solution between the compounds Ti_3SiC_2-Ti_3GeC_2 and Ti_3AlC_2–Ti_3AlCN even exists.

2.2 Experimental Details

2.2.1 Starting Powders

Bulk polycrystalline samples of Ti_3GeC_2, $Ti_3Si_{0.5}Ge_{0.5}C_2$ and $Ti_3Si_{0.75}Ge_{0.25}C_2$ were fabricated by weighing and mixing Ti, C, SiC, and Ge powders, the characteristics of which are listed in Table 2.1.

The starting powders for the $Ti_3Si_{0.5}Al_{0.5}C_2$ solid solution composition were Ti, SiC, Al and C and those for $Ti_3Al(C_{0.5}, N_{0.5})_2$ and $Ti_2AlC_{0.5}N_{0.5}$ were Ti, Al, AlN and C (Table 2.1).

Table 2.1 Sources and characteristics of powders used in this work.

Powder	Purity (%)	Particle characteristic	Source
Ti	99.5	-325 mesh	Johnson Matthey, MA
SiC	99.9	d_{mean}~12-40μm	Atlantic Equipment Engineers, NJ
Ge	99.999	-200 mesh	Advanced Technologies Inc., NJ
Graphite	99.0	-300 mesh	Johnson Matthey, MA
Al	99.5	-325 mesh	Johnson Matthey, MA
AlN	99.0	-200 mesh	Cerac Inc., WI

2.2.2 Processing Procedures

To synthesize the solid solution compositions in the Ti_3SiC_2-Ti_3GeC_2 system, roughly 40 g of powders were stoichiometrically weighed, ball milled for about 30 min; poured and tapped in borosilicate glass tubes, which in turn were sealed under a mechanical vacuum. The tubes were heated in a box furnace at 10 °C min^{-1} to 550 °C, held at that temperature for 2 h, then heated at 5 °C min^{-1} to 650 °C and held there for 9 h. This procedure was used to pre-react the powders and insure that they did not ignite during subsequent heating in the hot isostatic press (HIP).

To fabricate coarse-grained, CG, $Ti_3Si_{0.5}Ge_{0.5}C_2$, and $Ti_3Si_{0.75}Ge_{0.25}C_2$ samples the collapsed tubes were placed in a HIP; heated at 10 °Cmin^{-1} to 650 °C, then at 2 °C min^{-1} to 750 °C, at which time the chamber was pressurized with Ar to ≈100 MPa. The heating

was resumed at a rate of 10 °C min^{-1} to 1600 °C and held at temperature for 8 h, before furnace cooling. The chamber pressure at 1600 °C was ~172 MPa. To fabricate fine-grained, FG, $Ti_3Si_{0.5}Ge_{0.5}C_2$ samples, the same heating schedule and pressure was followed except that the final soaking temperature was 1450 °C. Once removed from the HIP the glass layers were machined off.

For reasons that are not entirely clear, it was not possible to fabricate fully dense, single phase samples of Ti_3GeC_2 by HIPing. Instead, coarse-grained, CG samples of Ti_3GeC_2 were prepared by hot pressing. Roughly 240 g of the stoichiometric mixture of Ti, Ge, and C powders were ball milled for about 40 min; poured and wrapped with BN presprayed graphite foils. The latter were placed in a graphite die in the HP, which was heated at a rate of 10 °C min^{-1} to 900 °C, held there for 3 h after which a pressure of ~45 MPa was applied and heating was resumed at the same rate to 1600 °C, and held at temperature for 6 h before furnace cooling. These samples were further annealed at 1600 °C for 48 h in an Ar atmosphere in a tube furnace to allow the unreacted phases to react and to grow the grains [27].

The $Ti_3Si_{0.5}Al_{0.5}C_2$ solid solution composition was also made by HIPing. The Ti, SiC, Al and C powders were mixed in appropriate ratios, cold pressed under 600 MPa and pre-reacted in a vacuum hot press (10^{-2} torr)) at 625 °C for 10 h. The $Ti_3Si_{0.5}Al_{0.5}C_2$ samples were then HIPed at different temperatures (1400-1600 °C) for 8- 10 h under 100-172 MPa pressure. However, essentially single phase, dense solid solution samples were produced by HIPing at 1400 °C for 10 h under 100 MPa pressure followed by annealing in an Ar atmosphere for 48 h, to reduce the unwanted phases [28].

To synthesize bulk polycrystalline samples of $Ti_3Al(C_{0.5},N_{0.5})_2$ and $Ti_2AlC_{0.5}N_{0.5,}$ roughly 20 g of powders were stoichiometrically weighed, ball milled overnight and cold pressed using a pressure of ≈ 600 MPa. The green bodies were pre-sintered in a vacuum HP which was heated at a rate of ≈ 5 ºC min^{-1}, under vacuum (10^{-2} torr) to 525 ºC, held at that temperature for 2 h, then heated at 4 ºC min^{-1} to 625 ºC and held there for 10 h. This procedure was used to pre-react the powders and insure that they did not ignite during subsequent heating. The pellets were also weighed before and after this pre-sintering process to ensure that there was no loss of Al. The pre-sintered pellets were then placed in a HIP, and heated at 5 ºC min^{-1} to 850 ºC, then at 2 ºC min^{-1} to 1000 ºC, at which time the chamber was pressurized with Ar to ≈ 80 MPa. The heating was resumed at a rate of 10 ºC min^{-1} to 1400 ºC and held at that temperature for 10 h before furnace cooling. The chamber pressure at 1400 ºC was ≈ 100 MPa [29].

The as-processed samples were then characterized using x-ray diffraction, optical microscopy and field emission scanning electron microscopy.

2.3 Results and Discussion

2.3.1 Microstructural Characterization

Powders for X-ray diffraction (XRD) were extracted by drilling into the bulk of the samples. Phase identification was accomplished with XRD using a powder diffractometer (Siemens D-500). Scans were made with Cu Kα radiation (40KV and 30 mA) at a rate of 6º (2θ) min^{-1} using a step size of 0.05º. The lattice parameters were

measured using a step size of 0.008º and a step time of 1 s. Pure silicon was added as an internal standard.

The samples were sliced using a diamond wheel, ground with SiC emery paper and polished down to 1 μm diamond for microstructural evaluation. The polished samples were microstructurally characterized using an optical microscope (PMG3, Olympus, Tokyo, Japan) and a field emission scanning electron microscope, FESEM, (XL-30, FEI-Philips, Hillsboro, OR) equipped with an energy dispersive spectroscope, EDS (Edax Inc., Mahwah, NJ). Most measurements were carried out using an accelerating voltage of 30 KV in backscattered mode. To expose the grains, measure their size and determine the volume fraction of any secondary phases present, the polished samples were etched using a 1:1:1 by volume HF: HNO_3: H_2O solution [1]. The grain size of the samples was measured using ASTM E 112 [30] method (intercept method). The densities of all samples were measured by Archimedes' principle in ambient temperature water.

2.3.1.1 Ti_3GeC_2

Predominantly single phase samples of Ti_3GeC_2 contained ~ 3 vol. % TiO_2 (Fig. 2.1 a). Figure 2.2 a shows a typical OM micrograph of an etched sample, where the grains are exposed. The grains were equiaxed with an average size of 46±25 μm. At 5.3 ± 0.2 Mg m^{-3}, the measured density was >95% of theoretical (5.55 ± 0.2 Mg m^{-3}). The molar percentages of Ti and Ge in the matrix were determined by EDS to be 74±1 and 26 ± 1%, respectively.

2.3.1.2 Ti_3SiC_2-Ti_3GeC_2 Solid Solutions

Coarse grained (CG) $Ti_3Si_{0.5}Ge_{0.5}C_2$ samples were predominantly single phase, with <2 vol.% of TiC and ~3 vol.% of what appears to have been a Si–Ti rich liquid phase with Ti, Si and Ge mol%, determined by EDS, of 40 ± 3.5%, 48 ± 4 to 12 ± 1% (Fig. 2.1 b). The corresponding values for the matrix were 69.7±0.2, 17±1, and 14±1%, respectively. In other words, the matrix was slightly Si rich, and Ti and Ge poor relative to the initial composition. The grains were plate-like, with an average diameter of 40 ± 30 μm and an aspect ratio of 2.3 (Fig. 2.2 b). At 5.0 ± 0.1Mgm^{-3}, the measured density was ~99% of theoretical (5.035 Mg m^{-3}). The fine-grained, FG, samples were also predominantly single phase (Fig. 2.1 c) with ~ 4 vol. % TiC. Their average grain size was 7 ± 3 μm (Fig. 2.2 c). No evidence of a liquid phase was detected, which implies the liquid phase in this composition forms somewhere between 1500 and 1600 ºC.

The $Ti_3Si_{0.75}Ge_{0.25}C_2$ samples were also predominantly single phase with ~3 vol. % TiC (Fig. 2.1 d). The grains were plate-like with an average grain size of 70±56 μm and an aspect ratio of 3 (Fig. 2.2 d). EDS of the matrix showed the molar percentages of Ti, Si, and Ge to be 70.9±0.3%, 22.6± 0.4 to 6.5 ± 0.1, respectively. The measured density in this case exactly matched the theoretical density ~ 4.8 Mg m^{-3}.

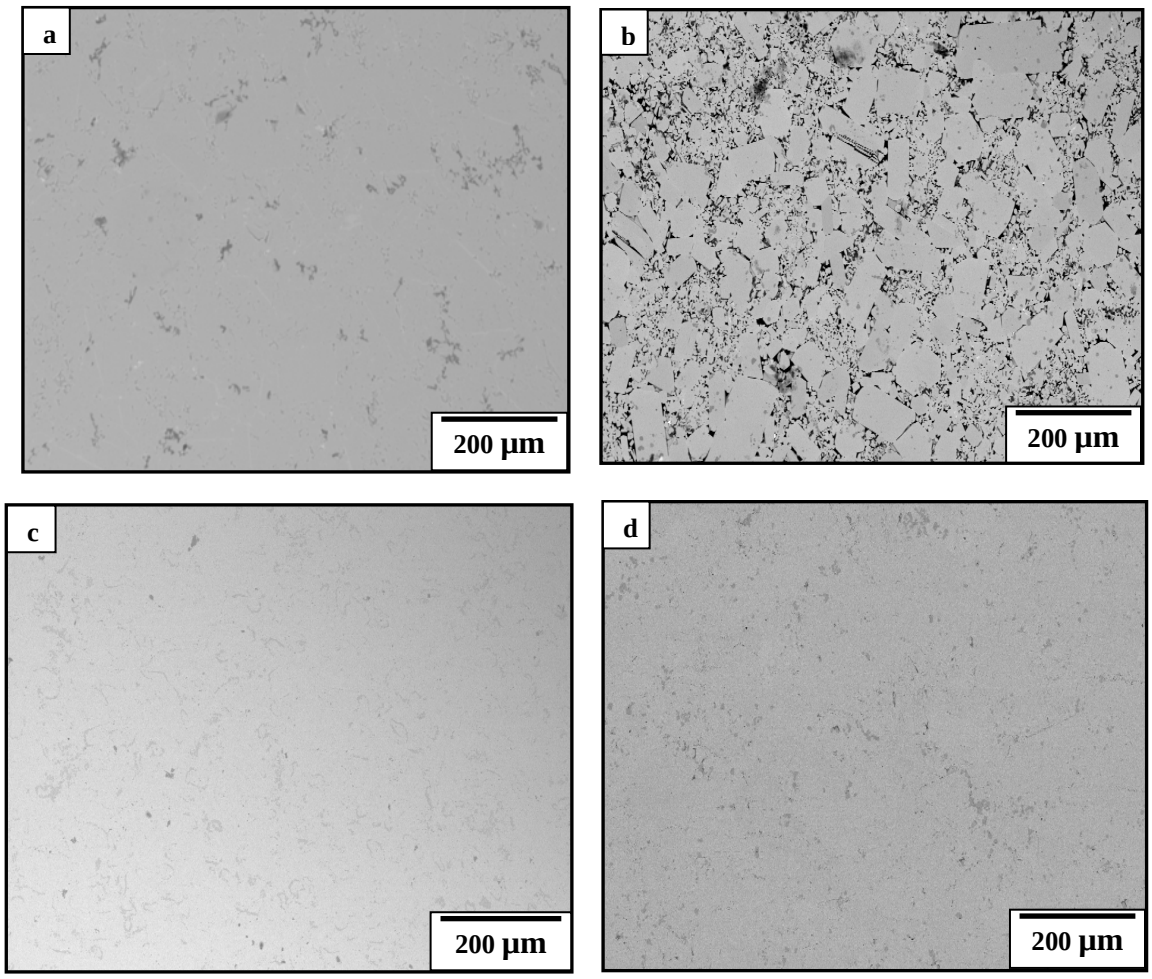

Figure 2.1: Backscattered SEM micrographs of polished samples of: (a) CG Ti_3GeC_2 HPed at 1600 ºC for 6 h followed by 48 h Ar anneal. Some dark areas are TiO_2 particles and some are pullouts; (b) CG $Ti_3Si_{0.5}Ge_{0.5}C_2$ HIPed at 1600 ºC for 8 h. Some dark areas are Ti-Ge rich liquid phase and some are pullouts; (c) FG $Ti_3Si_{0.5}Ge_{0.5}C_2$ HIPed at 1450 ºC for 8 h; and (d) CG $Ti_3Si_{0.75}Ge_{0.25}C_2$ HIPed at 1600 ºC for 8 h.

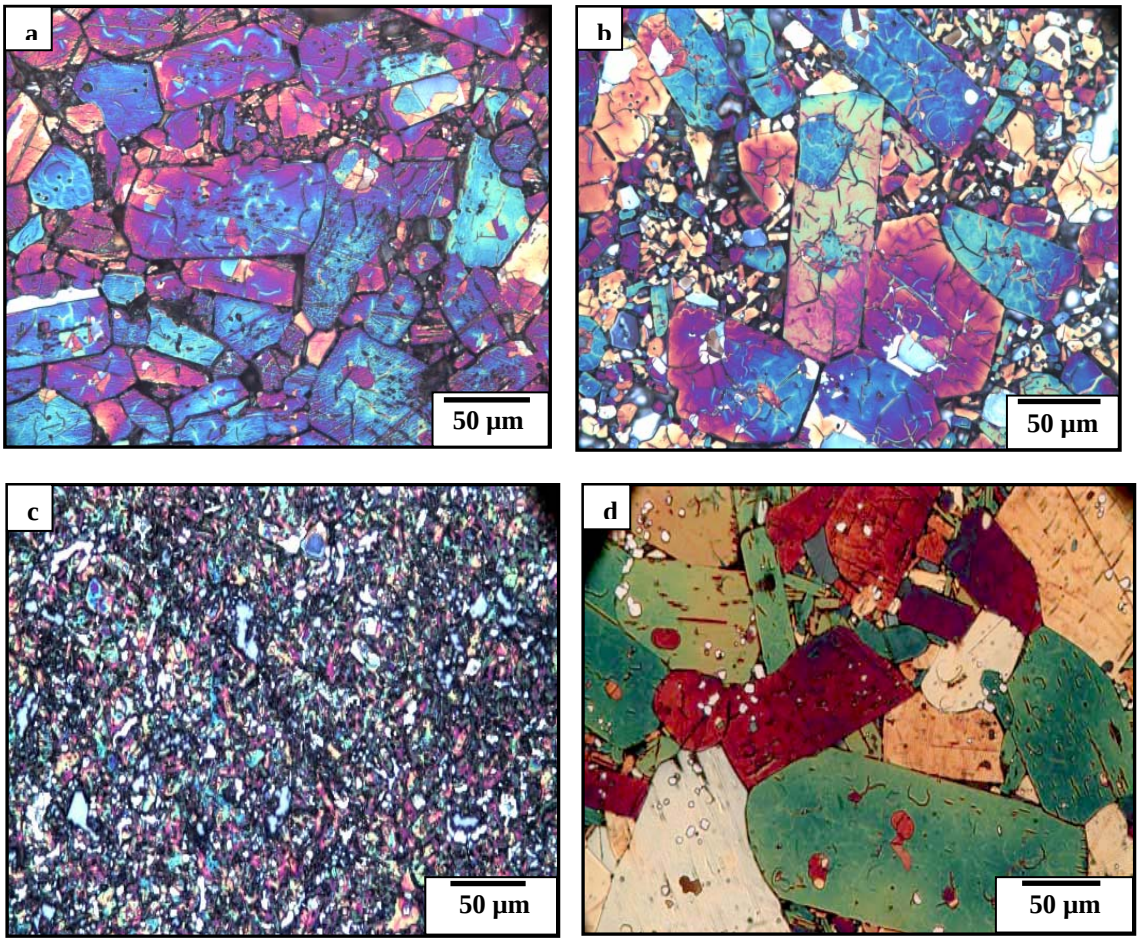

Figure 2.2: Optical micrographs of etched samples of: (a) CG Ti_3GeC_2 HPed at 1600 ºC for 6 h followed by 48 h Ar anneal; (b) CG $Ti_3Si_{0.5}Ge_{0.5}C_2$ HIPed at 1600 ºC for 8 h, dark areas are a Ti-Ge rich liquid phase;(c) FG $Ti_3Si_{0.5}Ge_{0.5}C_2$ HIPed at 1450 ºC for 8 h, small bright regions are TiC_x (~4 vol. %) and, (d) CG $Ti_3Si_{0.75}Ge_{0.25}C_2$ HIPed at 1600 ºC for 8 h, white dots are TiC_x (~3 vol. %).

Figure 2.3 shows the XRD spectra of all the compositions synthesized as well as those of Ti_3SiC_2 [31]; the corresponding lattice parameters are listed in Table 2.2. Also included are lattice parameters of Ti_3SiC_2 [32, 33], Ti_3AlC_2 [32, 33], Ti_3GeC_2 [13] and $Ti_3Si_{0.5}Al_{0.5}C_2$ (Discussed in the next subsection). As expected the lattice parameters of the solid solutions lie in between those of the end members. A summary of the XRD results for Ti_3GeC_2, $Ti_3Si_{0.5}Ge_{0.5}C_2$ and $Ti_3Si_{0.75}Ge_{0.25}C_2$ are listed in Table 2.3, 2.4 and 2.5 respectively.

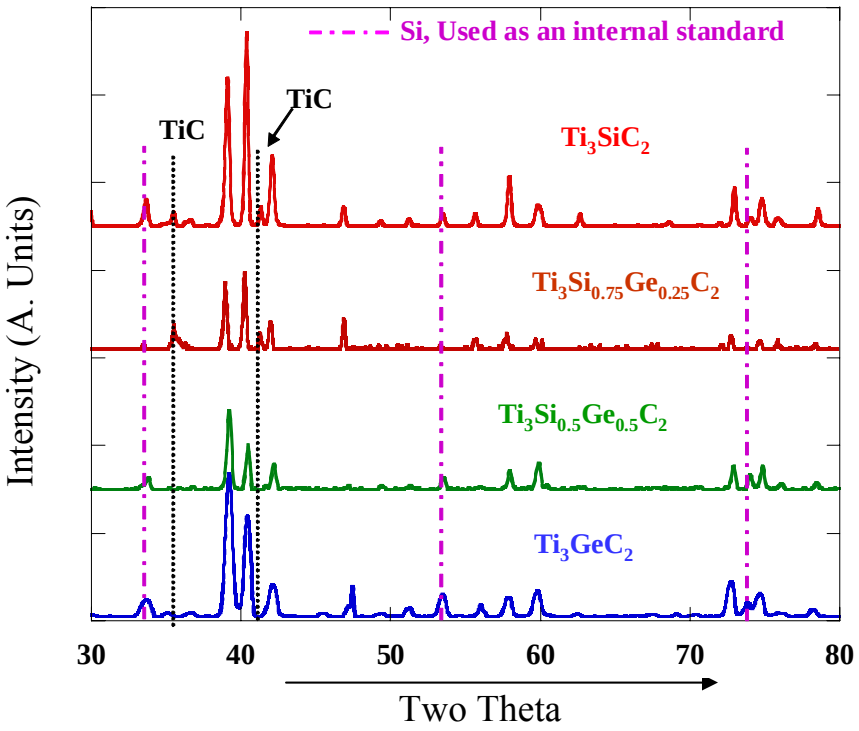

Figure 2.3: XRD pattern of Ti_3GeC_2, $Ti_3Si_{0.5}Ge_{0.5}C_2$ and $Ti_3Si_{0.75}Ge_{0.25}C_2$. Also shown is pattern of Ti_3SiC_2 [31]. Si is used as an internal standard and TiC is the minor impurity phase.

Table 2.2 Summary of lattice parameters of A-site substituted solid solutions. Also included are the lattice parameters of Ti_3SiC_2 [32, 33], Ti_3AlC_2 [32, 33] and Ti_3GeC_2 [13].

Compound	a (Å)	c (Å)	Ref.
Ti_3GeC_2	3.0874	17.806	[13]
Ti_3GeC_2	3.09	17.764	[This Work]
$Ti_3Si_{0.5}Ge_{0.5}C_2$	3.082	17.751	[This Work]
$Ti_3Si_{0.75}Ge_{0.25}C_2$	3.074	17.747	[This Work]
Ti_3SiC_2	3.0665	17.671	[32]
Ti_3SiC_2	3.067	17.675	[33]
$Ti_3Si_{0.5}Al_{0.5}C_2$	3.074	18.456	[This Work]
Ti_3AlC_2	3.075	18.578	[32]
Ti_3AlC_2	3.073	18.557	[33]

Table 2.3 Summary of XRD results for the Ti_3GeC_2 composition HPed for 6 h at 1600 ºC and then annealed in Ar at the same temperature for an additional 48 h. The calculated values assume c = 17.764 Å and a = 3.090 Å.

(h k l)	$2\theta_{measured}$	$d_{measured}$	$d_{calculated}$	d^*	$(I/I_{max})_{measured}$	$(I/I_{max})^*$
1 0 0	33.633	2.663	2.677	2.668	14.5	80
1 0 4	39.199	2.296	2.294	2.287	100	100
0 0 8	40.423	2.229	2.224	2.211	70	70
1 0 5	42.111	2.144	2.140	2.132	25.3	80
1 0 8	53.453	1.712	1.710	1.708	14.6	70
1 0 9	57.8526	1.592	1.590	1.588	13.6	40
1 1 0	59.776	1.545	1.545	1.542	18.8	90
2 0 4	73.865	1.281	1.281	1.278	7.9	80
1 1 8	74.671	1.270	1.270	1.266	18.8	85
2 0 6	78.250	1.220	1.220	1.216	4.5	10
0 0 16	87.698	1.111	1.111	1.107	18.6	5

* Ref [13].

Table 2.4 Summary of XRD results for the $Ti_3Si_{0.5}Ge_{0.5}C_2$ composition HIPed for 8 h at 1600 ºC. The calculated values assume c = 17.751 Å and a = 3.082 Å.

(h k l)	$2\theta_{measured}$	$d_{measured}$	$d_{calculated}$	$(I/I_{max})_{measured}$
1 0 0	33.574	2.667	2.668	5.8
1 0 1	33.960	2.637	2.639	11.8
1 0 3	36.924	2.432	2.432	56.4
1 0 4	39.365	2.287	2.287	100
0 0 8	40.616	2.219	2.219	45.9
1 0 5	42.334	2.133	2.133	22.7
1 0 7	49.533	1.838	1.838	2.9
0 0 10	51.402	1.776	1.775	0.9
1 0 8	53.672	1.706	1.706	8.4
1 0 9	58.091	1.586	1.586	12.6
1 1 0	59.993	1.540	1.540	15.6
1 1 6	69.149	1.357	1.360	4.1
2 0 3	73.042	1.295	1.301	11
2 0 4	74.121	1.278	1.277	5.4
1 1 8	74.951	1.266	1.265	11.1
2 0 5	76.334	1.246	1.249	6.1
2 0 6	78.631	1.215	1.216	0.7
0 0 16	87.939	1.109	1.109	19.4

Table 2.5 Summary of XRD results for the $Ti_3Si_{0.75}Ge_{0.25}C_2$ composition HIPed for 8 h at 1600 ºC. The calculated values assume c = 17.7476 Å and a = 3.0744 Å.

(h k l)	$2\theta_{measured}$	$d_{measured}$	$d_{calculated}$	$(I/I_{max})_{measured}$
104	39.419	2.2840	2.283	88
008	40.6937	2.2154	2.2184	100
105	42.426	2.1288	2.1299	38.5
109	58.2112	1.5836	1.5846	21.4
110	60.1448	1.5372	1.5372	9.2
203	73.220	1.2916	1.2987	20.4
118	75.1295	1.2635	1.2635	12
205	76.3448	1.2463	1.2464	9.4
206	78.8876	1.2124	1.2139	6.2
0016	87.9663	1.1092	1.1092	21

2.3.1.3 Ti_3SiC_2-Ti_3AlC_2 Solid Solutions

Figure 2.4 a shows a typical cross sectional backscattered micrograph of $Ti_3Si_{0.5}Al_{0.5}C_2$. The sample is single phase, dense with TiC <5 vol. %, with a grain size of 15±5 μm. The matrix composition as determined by EDS was observed to be Ti: Si: Al ~72±0.9: 14.4±0.5: 13.6±1, in molar percentages. Figure 2.4 b shows a typical OM of the FG solid solution composition. The white spots in this figure are TiC_x. Figure 2.5 shows the XRD pattern of this solid solution composition as compared to Ti_3SiC_2 [31]. A summary of the XRD results for $Ti_3Si_{0.5}Al_{0.5}C_2$ are listed in Table 2.6.

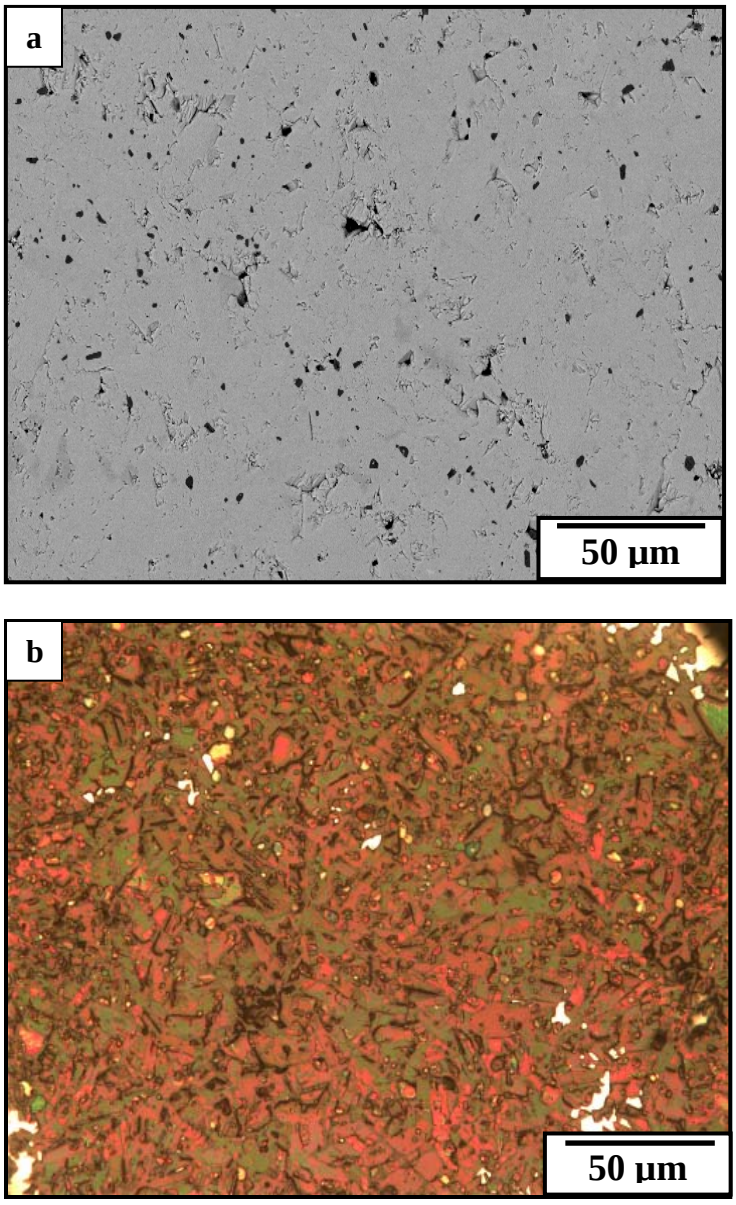

Figure 2.4: (a) Typical backscattered SEM micrograph and (b) etched optical micrograph of polished samples of $Ti_3Si_{0.5}Al_{0.5}C_2$, HIPed at 1400 ºC for 10h followed by annealing under Ar. atmosphere for 48h. The white dots in the optical micrograph represent TiC_x.

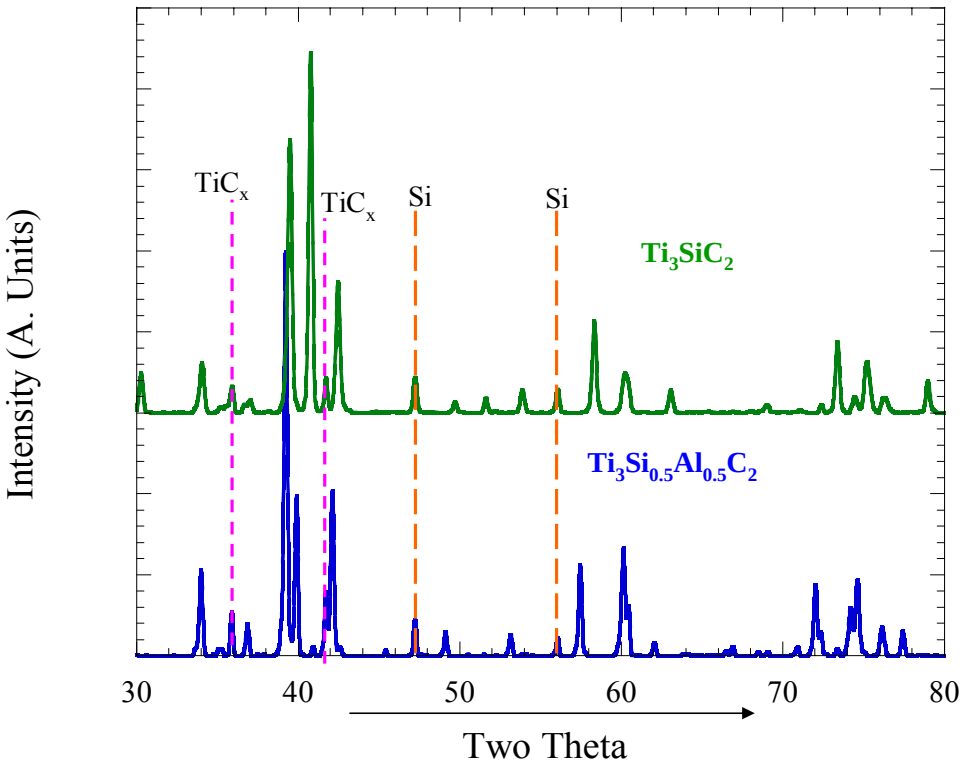

Figure 2.5: XRD pattern of $Ti_3Si_{0.5}Al_{0.5}C_2$. Also shown is pattern of Ti_3SiC_2 [31]. Si is used as an internal standard and the peaks of the minor impurity phase TiC_x are shown as dashed line.

Table 2.6 Summary of XRD results for the $Ti_3Si_{0.5}Al_{0.5}C_2$ composition HIPed for 8 h at 1400 ºC, and then annealed in Ar, at the same temperature, for an additional 48 h. The calculated values assume c = 18.456 Å and a = 3.074 Å.

(h k l)	$2\theta_{measured}$	$d_{measured}$	$d_{calculated}$	$(I/I_{max})_{measured}$
1 0 1	34	2.634	2.633	21.9
1 0 3	36.88	2.435	2.434	7.8
1 0 4	39.254	2.293	2.292	100
0 0 8	39.921	2.256	2.254	36.5
1 0 5	42.141	2.142	2.141	36.9
1 0 7	49.151	1.852	1.851	5.9
1 0 8	53.17	1.721	1.72	5.5
1 0 9	57.482	1.6	1.6	22.7
1 1 0	60.151	1.537	1.537	22.8
2 0 3	72.04	1.309	1.3	15.7
2 0 4	74.224	1.276	1.276	14.1
1 1 8	74.646	1.27	1.27	21.8
2 0 5	76.175	1.248	1.248	30
0 0 16	86.1	1.128	1.128	4.7

2.3.1.4 Effect of A-Site Substitutions on the Lattice Parameters

A closer look at the crystal structures of the MAX phases (previously discussed in Ch.1) reveals the fact that the distance between the M-A layers determines the c-axis. Hence a substitution on the A-site is expected to affect the c-axis more than a-axis. Figure 2.6 (a) shows the effect of A-site substitutions on the lattice parameters in the Ti_3SiC_2-Ti_3GeC_2 system-while Fig. 2.6 (b) shows the influence of the difference in the atomic radii of Si and Ge on the lattice parameters. Both lattice constants increase with an increase in the atomic percentage of the A group element, with the larger radius (Ge in this case). The effect on c is observed to be more profound than on a, as expected.

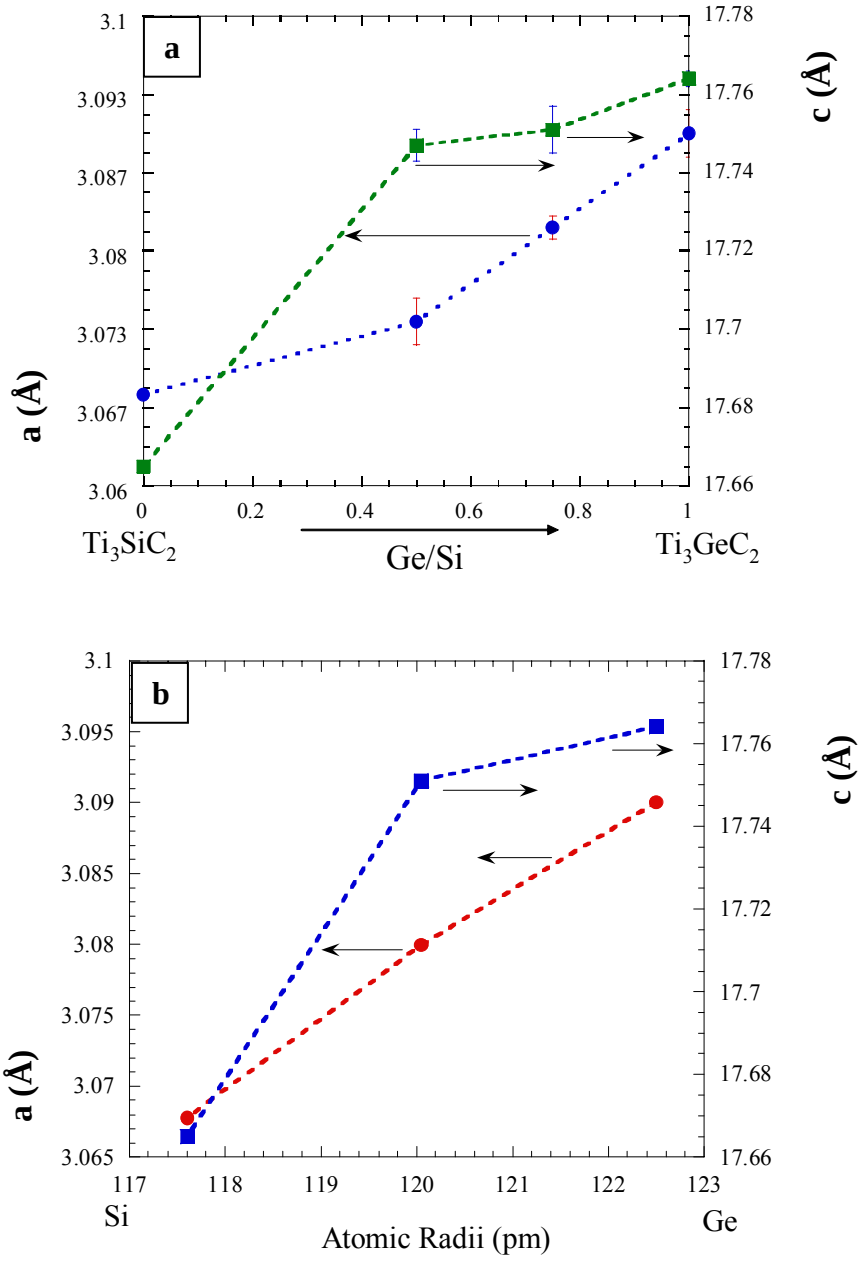

Figure 2.6: Effect of (a) A-site substitutions, and (b) atomic radii on the lattice parameter in the Ti_3SiC_2-Ti_3GeC_2 system.

Similar behavior is observed in the Ti_3SiC_2-Ti_3AlC_2 system (Fig. 2.7). In this case, the change in c is about 1 Å, which can be accounted for by the large difference between the atomic radii of Al (145 pm) and Si (117 pm). The values of lattice parameter for $Ti_3Si_{(1-x)}Al_xC_2$ system in the range of x = 0.1-0.25 were obtained by Zhou et al. [18].

It is to be noted that the atomic radii for the solid solution compositions in each of the 312 systems were taken as the average of the A-site elements of the corresponding end members.

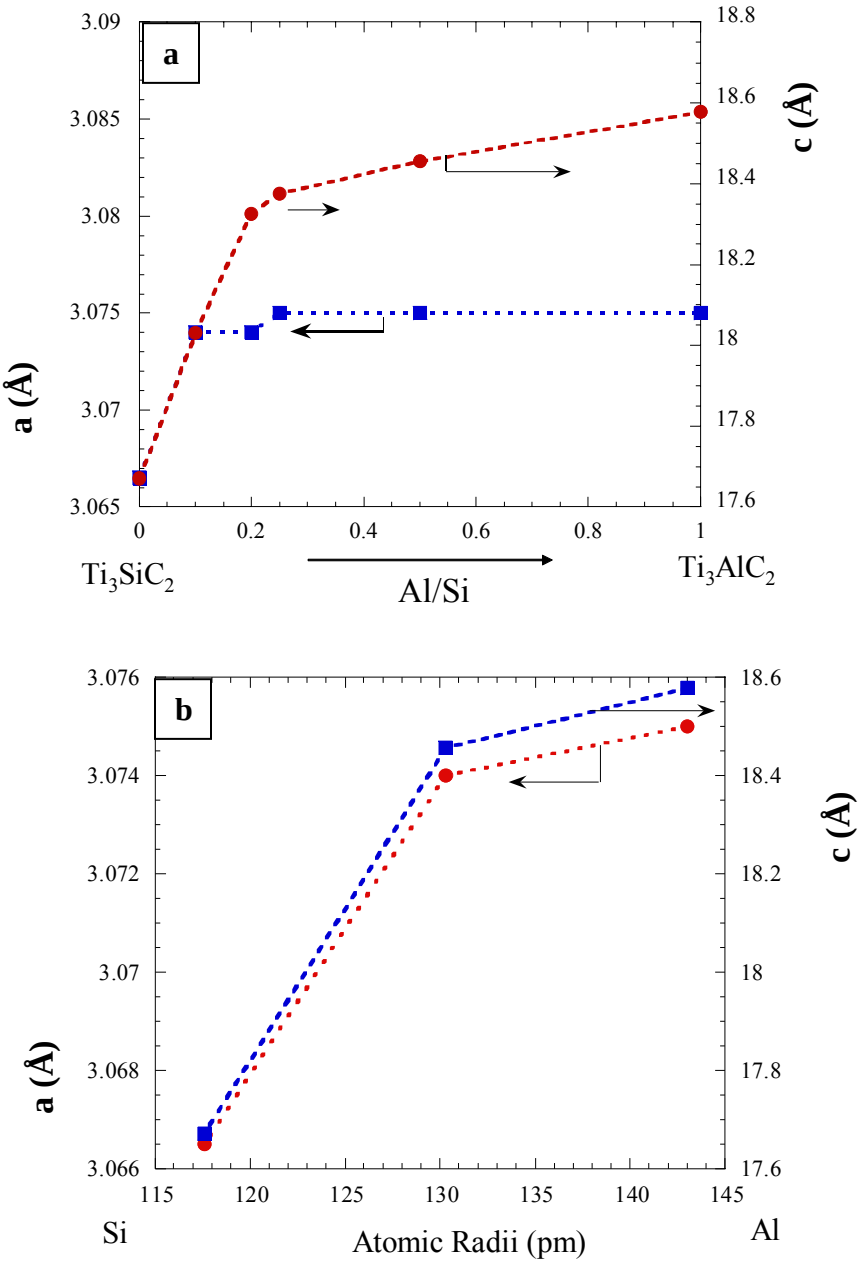

Figure 2.7: Effect of (a) A-site substitutions and, (b) atomic radii on the lattice parameters in the Ti_3SiC_2-Ti_3AlC_2 system. The values of the lattice parameter for the $Ti_3Si_{(1-x)}Al_xC_2$ system in the range of x = 0.1-0.25 are cited from the work of Zhou et al. [18].

2.3.1.5 X-Site Substituted Solid Solutions

2.3.1.5.1 $Ti_3Al(C_{0.5},N_{0.5})_2$

Medium grained, (MG), $Ti_3Al(C_{0.5},N_{0.5})_2$ samples were single phase, dense with ~ 3 vol. % of TiC and ~2 vol. % of Al_2O_3. Figure 2.8 (a) shows a typical backscattered micrograph of this sample. The dark regions are Al_2O_3. The molar percentages of Ti and Al in the matrix as determined by EDS were 74.95±0.1 and 25.0±0.5, respectively. The grains were plate-like, with an average diameter of 30 ± 5 μm and an aspect ratio of~ 2.0 (Fig. 2.9 a). At 4.49 Mg m^{-3}, the measured density was ~99% of theoretical (4.535 Mg m^{-3}).

2.3.1.5.2 $Ti_2Al(C_{0.5},N_{0.5})$

Figure 2.8 (b) shows a typical backscattered micrograph of $Ti_2Al(C_{0.5},N_{0.5})$. The sample was dense, single phase with < 2 vol. % of Al_2O_3. EDS of the matrix showed the molar percentages of Ti and Al to be 68.6±0.1 and 31 ± 1, respectively. At 4.19 Mgm^{-3}, the measured density was ~99.5 % of theoretical (4.21 Mg m^{-3}). The grains were equiaxed with an average size of 40±10 μm (Fig. 2.9 b).

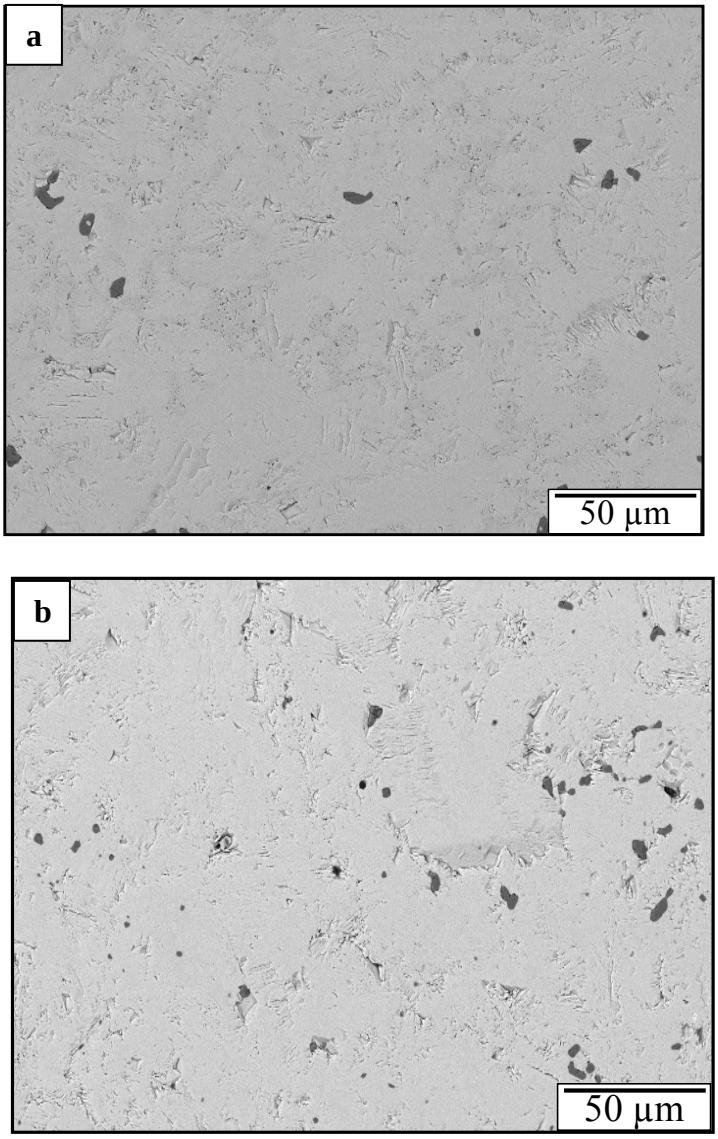

Figure 2.8: Typical backscattered SEM micrographs of polished samples of, (a) $Ti_3Al(C_{0.5},N_{0.5})_2$ and, (b) $Ti_2Al(C_{0.5},N_{0.5})$, HIPed at 1400 ºC for 10 h. The dark areas are Al_2O_3 inclusions.

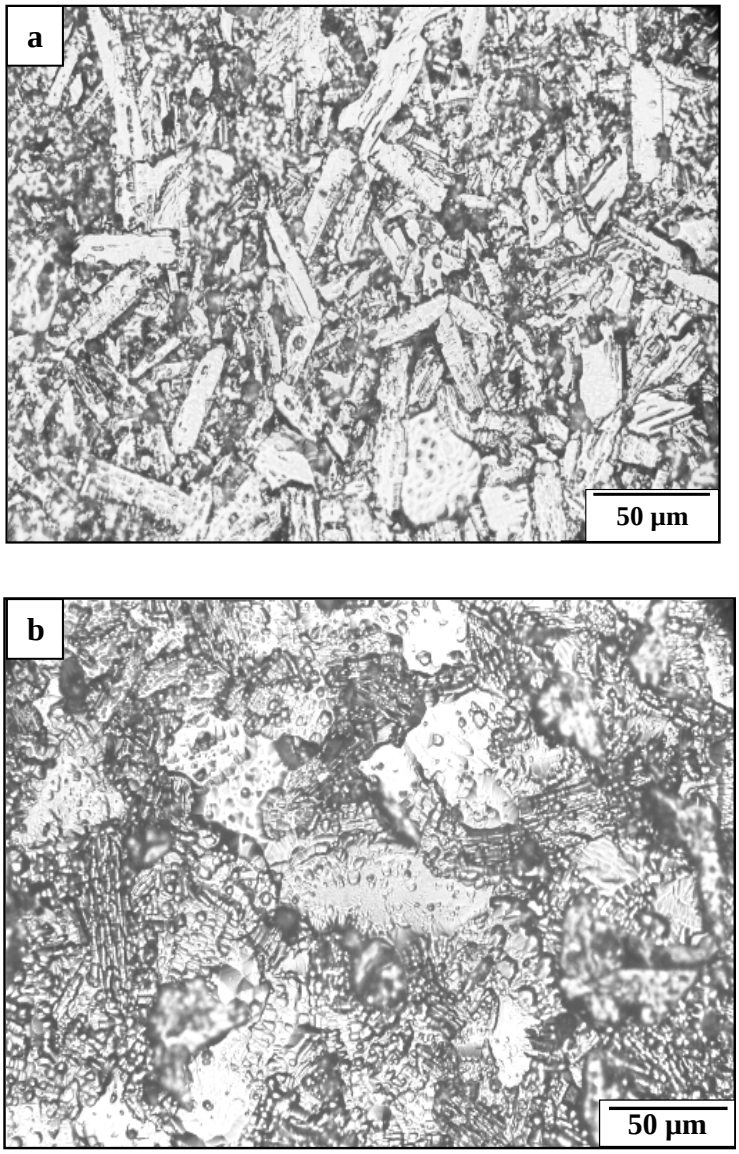

Figure 2.9: Etched optical micrographs of, (a) $Ti_3Al(C_{0.5},N_{0.5})_2$ and, (b) $Ti_2Al(C_{0.5},N_{0.5})$, HIPed at 1400 ºC for 10 h.

The XRD patterns of the above mentioned solid solution compositions is shown in figure 2.10, the corresponding lattice parameters are listed in Table 2.7. The lattice parameters of Ti_3AlC_2 [32, 33], Ti_3AlN_2 [34], Ti_2AlC and Ti_2AlN [32] are also included for the sake of comparison. It is to be noted here that even though Ti_3AlN_2 is not known to exist, the value of the lattice constants for this composition was taken as the average of Ti_2AlN and Ti_4AlN_3 and has been portrayed here to complete the comparison. Also given is the value of Ti_3AlN_2 [34] obtained theoretically. A detailed summary of the XRD results for $Ti_3Al(C_{0.5}, N_{0.5})_2$ are listed in Table 2.8.

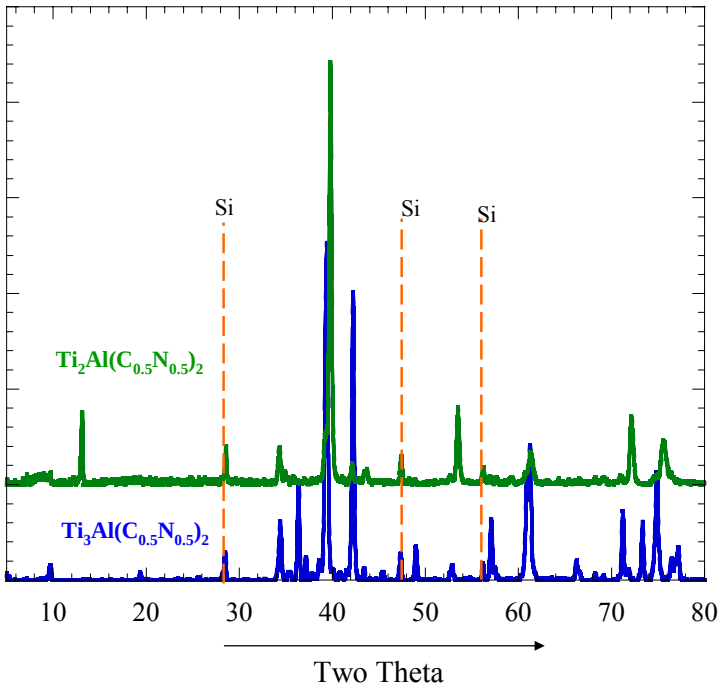

Figure 2.10: XRD pattern of (a) $Ti_3Al(C_{0.5},N_{0.5})_2$ and, (b) $Ti_2Al(C_{0.5},N_{0.5})$, HIPed at 1400 ºC for 10 h. Si is used as an internal standard.

Table 2.7 Summary of lattice parameters of X-site substituted solid solutions. Also included are the lattice parameters of Ti_3AlC_2 [32, 33], Ti_3AlN_2 [34], Ti_4AlN_3 [62], Ti_2AlC and Ti_2AlN [32].

	a (Å)	c (Å)	Comments + Ref.
Ti_2AlC	3.04	13.6	[32]
$Ti_2Al(C_{0.5},N_{0.5})$ [This Work]	3.023	13.61	[This Work]
Ti_2AlN	2.989	13.614	[32]
Ti_3AlC_2	3.075	18.578	[32]
Ti_3AlC_2	3.073	18.557	[33]
$Ti_3Al(C_{0.5},N_{0.5})_2$	3.04	18.3653	[This Work]
Ti_3AlN_2 (Average of 211 and 413)	2.9885	18.493	(Average of 211 and 413)
Ti_3AlN_2	3.09	18.1	[34]
Ti_4AlN_3	2.99	23.34	[62]

Table 2.8 Summary of XRD results for the $Ti_3Al(C_{0.5},N_{0.5})_2$ composition HIPed for 10 h at 1400 ºC. The calculated values assume c = 18.3653 Å and a = 3.04 Å

(hkl)	$2\theta_{measured}$	$d_{measured}$	$d_{calculated}$	$(I/I_{max})_{measured}$
101	34.381	2.606	2.606	14.4
102	35.374	2.534	2.53	7.5
103	36.36	2.468	2.42	22
104	39.3659	2.287	2.284	100
105	42.2148	2.139	2.139	60.4
107	48.976	1.858	1.858	8.4
108	52.847	1.731	1.73	3.4
109	57.07	1.612	1.6128	15.9
110	60.89	1.5202	1.5202	22.4
10 11	66.255	1.41	1.414	4.4
201	71.203	1.323	1.323	11.9
203	73.336	1.289	1.288	10.8
204	74.857	1.267	1.265	30.3
205	77.175	1.235	1.239	6.4
0016	84.3	1.147	1.147	3.6
209	88.1	1.108	1.106	5.0

2.3.1.6 Effect of X-Site Substitutions on the Lattice Parameters

Figure 2.11 shows the effect of X-site substitution on the lattice parameters in the Ti_3AlC_2-Ti_3AlN_2 and Ti_2AlC-Ti_2AlN systems. In each case the dependence of a on composition and atomic radii is much more evident than c. This behavior is due to the doping on the X site with elements of different atomic radius which influences the atomic spacings in the M_6X octahedra, which in turn affects a.

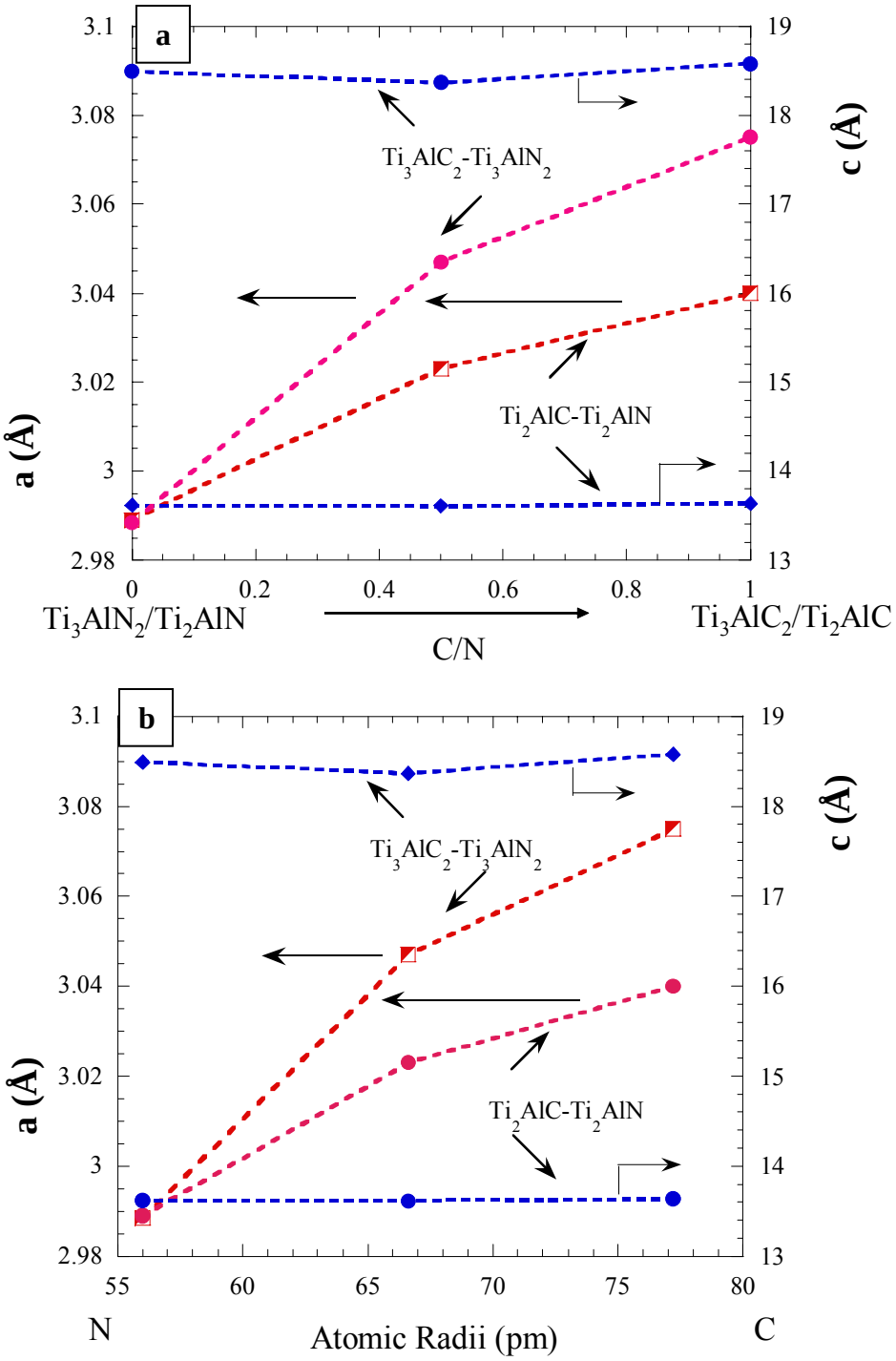

Figure 2.11: Effect of (a) X-site substitutions and (b) atomic radii on the lattice parameter in the Ti_3AlC_2/Ti_2AlC and Ti_3AlN_2/Ti_2AlN systems.

2.3.2 Processing Challenges

Several attempts were made to fabricate single phase, dense Ti_3GeC_2 samples by HIPing. The end result was porous samples, with unreacted TiC and Ge in the matrix. One possible explanation is the low melting point of Ge (923 ºC) which may have resulted in Ge loss from the system. The reducing atmosphere inside the vacuum hot press and prolonged soaking time at 900 ºC (3 h) may have prevented the Ge loss. However, the grain size of the as hot pressed sample was fine (FG), (Fig. 2.12). Further annealing under Ar atmosphere resulted in a CG sample (Fig. 2.2 a).

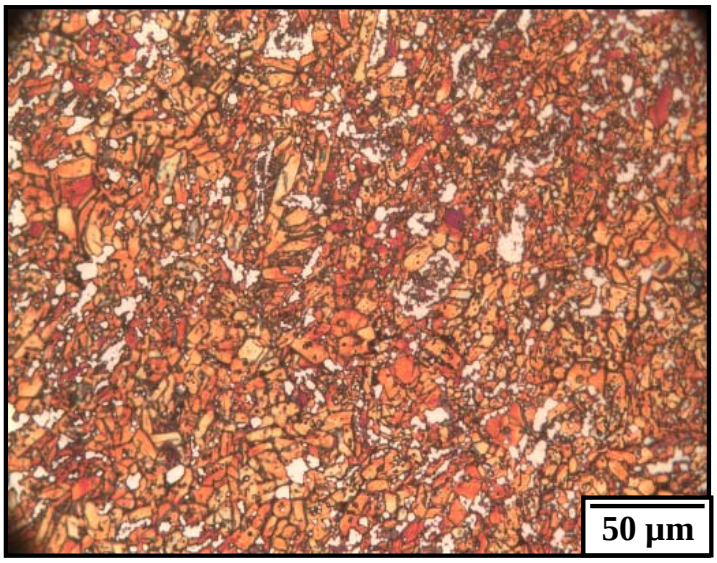

Figure 2.12: Optical micrograph of as hot pressed, etched sample of Ti_3GeC_2 (1600 ºC, 6h). Note the fine grain size~5±3 µm. Major impurity being TiC_x (~5 vol. %).

Synthesizing solid solutions of two end members with different atomic radii can be a daunting task. Difference in the atomic radii of the A (Si and Ge or Si and Al) or X group elements influences the stability of the solid solutions. The atomic radii of the three A group elements in the 312 system are of the order Al (145 pm)>Ge (123pm)>Si (117 pm). Needless to say that to stabilize the solid solution with the composition $Ti_3Si_{0.5}Al_{0.5}C_2$ was the biggest challenge. Several runs were made in the temperature range of 1400-1600 ºC. The optical micrograph of the samples heat treated in the temperature range of 1500-1600 ºC showed the presence of TiC as a major secondary phase in the matrix. Figure 2.13 shows a typical OM of $Ti_3Si_{0.5}Al_{0.5}C_2$ synthesized at 1600 ºC for 8h, P~172 MPa. The white regions are TiC_x. One plausible explanation behind this might be the phase separation occurring in the Ti_3SiC_2-Ti_3AlC_2 system at high temperatures. However, the sample heat treated at 1400 ºC followed by annealing under Ar for 48 h resulted in a cleaner matrix with FG size (Fig. 2.4).

The AlN powder - one of the raw materials used to synthesize $Ti_3Al(C_{0.5}N_{0.5})_2$ and $Ti_2Al(C_{0.5}N_{0.5})$- was coarser (-200 mesh size) compared to other raw materials used for the same purpose, viz: Ti (-325 mesh) and C (-300 mesh) powders. This factor influenced the milling time of the weighed powder batch considerably. Two separate batches of powders were ball milled for 30 mins and overnight, respectively, and then cold pressed to form the green body. A cross section of the cold pressed sample, ball milled for 30 mins showed the presence of white patches of AlN and HIPing of this sample resulted in a porous microstructure. Whereas, the cross section of the overnight ball milled, cold pressed sample had no such patches and HIPing of this sample resulted in a dense, single phase, medium grained microstructure.

In order to synthesize the Al based solid solutions the green bodies were pre-sintered at 625 ºC for 10 h in a vacuum hot press (near the melting point of Al) and the samples were weighed before and after the heat treatment to make sure there was no Al loss. This step was not only essential to pre- react the Al in a reducing atmosphere, but also was effective in reducing the Al_2O_3 content in the final microstructures.

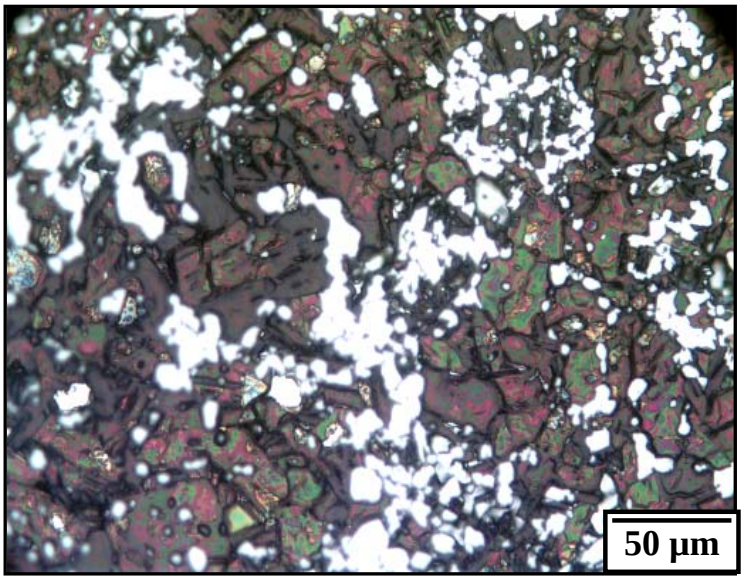

Figure 2.13: Optical micrograph of etched $Ti_3Si_{0.5}Al_{0.5}C_2$, synthesized at 1600 ºC for 8h; the pressure during the soaking period was, P~172 MPa. The white regions are TiC_x.

2.4 Conclusions

Bulk polycrystalline samples of $Ti_3Si_{0.5}Ge_{0.5}C_2$, $Ti_3Si_{0.75}Ge_{0.25}C_2$, $Ti_3Si_{0.5}Al_{0.5}C_2$ (A-site substituted solid solutions), $Ti_3Al(C_{0.5}N_{0.5})_2$ and $Ti_2Al(C_{0.5}N_{0.5})$ (X-site substituted solid solutions) were synthesized by reactive hot isostatic pressing (HIPing), the former four for the first time. A series of completed hot isostatic compaction runs were made at different temperatures in the range of 1400-1600 ºC. Based on x-ray diffraction and SEM-EDS results, it has been shown that fully dense, essentially single phase samples of $Ti_3Si_{0.5}Ge_{0.5}C_2$ and $Ti_3Si_{0.75}Ge_{0.25}C_2$ were produced by reactive HIPing in the temperature range of 1450-1600 ºC for 8h. Fine grained (FG) single phase samples of $Ti_3Si_{0.5}Al_{0.5}C_2$ were produced by HIPing at 1400 ºC for 10h, followed by annealing under inert atmosphere (Ar) for 24h. Medium grained (MG) single phase samples of $Ti_3Al(C_{0.5}N_{0.5})_2$ and $Ti_2Al(C_{0.5}N_{0.5})$ were formed by HIPing at 1400 ºC for 10h.

Bulk polycrystalline samples of Ti_3GeC_2 on the other hand were prepared by reactive hot pressing (HPing) at 1600 ºC for 4-6 h followed by annealing at same T in Ar for 48h to grow the grains.

The time-temperature processing envelope for fabricating, small (5-7 μm), large (above 100 μm) grain sized samples of Ti_3GeC_2 and A-site substituted solid solutions and medium grained samples (35-40 μm) of X-site substituted solid solutions has been delineated. The processing challenges encountered while synthesizing the ternary solid solutions have also been discussed.

Both lattice constants were observed to change with composition, however, in case of substitution on the A-site, the effect on c is observed to be more profound than on a and vice versa for the X-site substituted solid solutions.

3: Physical Properties

3.1 Introduction

Armed with high quality bulk samples, we may now proceed to investigate the intrinsic physical properties of these materials.

As a class, MAX phases possess a unique set of physical properties: Machinability, electrical and thermal conductivity, anomalously low hardness (Vickers hardness values of 2–4 GPa), thermal shock resistance, damage tolerance, stiffness (at 320 GPa the stiffness of Ti_3SiC_2 is almost 3 times that of Ti metal, with the same density of ~ 4.5 g/cm^3) [1, 14, 21] and relatively low coefficients of thermal expansion (8–10 × 10^{-6} ºC^{-1}) [1]. This set of properties derives partially from the metallic nature of the bonding, partially from the layered nature of the compounds and partially from the fact that dislocations multiply and are mobile even at room temperatures and, as important, are confined to the basal planes [31, 35, 36]. Because these materials possess only two independent slip systems, i.e. less than the five slip systems needed for ductility, but more than the typical ceramic, their response to stress, thermal shock, damage etc., is unique and in many cases, including this work, falls somewhere between the behavior of typical metals and ceramics.

This chapter is part of a larger effort aiming to understand the chemistry–structure–property relationships of the MAX phases. In order to do so, a database needs to be created and one of the more intriguing and important questions that this, and related, work try to answer is: What effects do substitutions on the A- or X-sites have on properties in general? Ultimately, this understanding is essential to tailor the properties of these technologically potentially important compounds for any given application.

Physical properties like compressibility, elasticity and thermal expansion coefficients of the MAX solid solutions and Ti_3GeC_2 are discussed in detail. Properties of Ti_3SiC_2 have been mentioned and compared to the experimental results wherever applicable.

3.2 High Pressure Study of MAX Solid Solutions and Ti_3GeC_2

The first paper dealing with the compressibility of the MAX phases was on Ti_3SiC_2 [37]. In case of Ti_3SiC_2 no phase transitions were observed up to a pressure of 61 GPa. At 206 GPa, the isothermal bulk modulus K_o, calculated by fitting the PV data with the Birch–Murnaghan equation, [38] is lower than that obtained for TiC, both experimentally (220-240 GPa) [39, 40] and theoretically (250 GPa) [41] but ~10%–15% larger than the values calculated from the elastic moduli [42] and Poisson's ratio (0.2) [43].

The pressure (P) dependencies of the relative shrinkage of the a and c lattice parameters were reported to be, respectively,

$$a/a_o = 1 - 9.15\times10^{-4}\,(P/P_o) \qquad (3.1)$$

$$c/c_o = 1 - 2.02\times10^{-3}(P/P_o) + 1.28\times10^{-5}(P/P_o)^2 \qquad (3.2)$$

where $P_0 = 1$ GPa.

However, recently Manoun et al. reported on the compressibility of Zr_2InC [44] and Ti_4AlN_3 [45]. Here again, K_o of these compounds, while high-- 216 GPa for Ti_4AlN_3 and 127 GPa for Zr_2InC - are lower than those of near stoichiometric TiN (300-318 GPa) [46,

47] or ZrC [39]. In all three compounds, the relative shrinkages with pressure are more severe along the c direction than that in the *a* direction.

In another study Wang et al. [48] reported on the bulk modulus of Ti_3GeC_2 under a non-hydrostatic state of stress up to 64 GPa. Evidence for a shear induced phase transformation was observed at ≈ 26.6 GPa. The bulk modulus was calculated to be 179±10 GPa.

This section reports on the compressibility and the lattice parameter dependence on pressure of Ti_3GeC_2 [49], the solid solution compositions, $Ti_3Ge_{0.5}Si_{0.5}C_2$ [50] and $Ti_3Al(C_{0.5}N_{0.5})_2$ [29] under nearly hydrostatic conditions. The results are compared to other recent studies, wherever applicable.

3.2.1 Experimental Details

A powdered sample of a given composition was pressurized using a gasketed diamond anvil cell with a 400 μm culet. The gasket, made of rhenium, Re, was 250 μm in initial thickness, indented to 40 μm, and had a 150 μm diameter hole. The sample, placed between two pieces of aluminum foil (15 μm thick), was packed in the hole. The high purity Al acts as a pressure marker and also a pressure medium by virtue of its low shear strength. Measurements were conducted at room temperature; pressure was determined from the equation of state of Al [51]. EDX diffraction spectra were collected with a fixed 2θ (=11°). The cell parameters were determined using least squares refinement on individually fitted peaks. The peaks were assigned to the hexagonal structure with the space group $P6_3/mmc$.

3.2.2 Results and Discussion

3.2.2.1 Ti_3GeC_2

A summary of the lattice parameters, their relative change, the unit cell volumes, V, and their relative changes with pressure are listed in Table 3.1.

Table 3.1 Unit cell parameters and volume of Ti_3GeC_2 at various pressures.

P (GPa)	a (Å) ± 0.002	c (Å) ± 0.02	V(Å^3) ± 0.1	a/a_o	c/c_o	V/V_o
0	3.084	17.80	146.6	1	1	1
2.53	3.074	17.70	144.8	0.9875	0.997	0.994
6.10	3.054	17.55	141.8	0.967	0.990	0.986
12.05	3.027	17.47	138.7	0.946	0.982	0.981
16.64	3.007	17.32	135.7	0.925	0.975	0.973
22.37	2.989	17.17	132.8	0.906	0.969	0.965
24.17	2.980	17.20	132.3	0.902	0.966	0.967
28.96	2.967	17.08	130.2	0.889	0.962	0.960
34.99	2.953	16.86	127.3	0.868	0.957	0.947
39.32	2.940	16.80	125.8	0.858	0.953	0.944
43.24	2.929	16.75	124.4	0.849	0.950	0.941
47.10	2.918	16.58	122.2	0.834	0.946	0.932
51.16	2.904	16.59	121.2	0.826	0.942	0.932

A least squares fit of the changes in the relative unit cell volume, V/V_o, with pressure yields (Fig. 3.1 a):

$$V/V_o = 1.0 - 0.0046\ P/P_o + 3x10^{-5}\ (P/P_o)^2 \quad R^2 > 0.998 \quad (3.3)$$

where $V_o = 146.6 \pm 0.1$ Å^3.

Fitting the same results to the Birch-Murnaghan equation [38]:

$$P = 3/2\ K_o\ [(V/V_o)^{-7/3} - (V/V_o)^{-5/3}]\ \{1 + 3/4(K_o' - 4)[(V/V_o)^{-2/3} - 1]\} \quad (3.4)$$

yields a K_o of 197 ± 2 GPa, with a derivative, K_o' of 3.4 ± 0.1. This K_o value is higher than the value obtained from ultrasound experiments on bulk Ti_3GeC_2 (186 GPa) and that predicted theoretically (191 GPa) based on density functional theory [52]. This value is lower than the corresponding values for Ti_3SiC_2 (206 GPa) [37] and TiC (220 GPa) [39]. The K_o value for Ti_3GeC_2 determined from Resonant Ultrasound Spectroscopy (RUS) measurement is reported to be even lower (174 GPa) [28].

And while the crystal structure is stable to pressures of ≈ 55 GPa, the compressibility is anisotropic. Least squares fits of the curves, yield (Fig 3.1 b):

$$a/a_o = 1 - 0.0016\ (P/P_o) + 9 \times 10^{-6}\ (P/P_o)^2 \quad R^2 > 0.998 \quad (3.5)$$

and

$$c/c_o = 1 - 0.0016\ P/P_o + 5 \times 10^{-6}\ (P/P_o)^2 \quad R^2 > 0.992 \quad (3.6)$$

In a recent study [53] Wang and Zhou performed first-principles total energy calculations; they demonstrated that a reversible polymorphic phase transition occurred in Ti_3SiC_2 when the shear strain energy was large enough to exceed the energy barrier. They described it as a sliding of Si atoms between 2b and 2d Wyckoff positions. These calculations were confirmed by Wang et al. [48], mentioned previously.

As observed in Ti_3SiC_2, the compressibility in Ti_3GeC_2 displayed anisotropy and the relative shrinkages with pressure is more severe along the c direction than that in the *a* direction.

3.2.2.2 $Ti_3Ge_{0.5}Si_{0.5}C_2$

A summary of the lattice parameters, their relative change, unit cell volumes, V, and their relative changes with pressure of $Ti_3Si_{0.5}Ge_{0.5}C_2$ are listed in Table 3.2

Table 3.2 Unit cell parameters and volume of $Ti_3Si_{0.5}Ge_{0.5}C_2$ at various pressures.

P (GPa)	a (Å) ± 0.001	c (Å) ± 0.01	V(Å^3) ± 0.1	a/a_o	c/c_o	V/V_o
0	3.079	17.77	145.9	1	1	1
4.65	3.062	17.56	142.6	0.994	0.988	0.977
6.00	3.054	17.56	141.8	0.992	0.988	0.972
8.94	3.038	17.45	139.4	0.986	0.982	0.955
13.16	3.020	17.33	136.9	0.981	0.976	0.939
18.79	2.996	17.13	133.1	0.973	0.964	0.912
23.61	2.983	17.00	131.0	0.969	0.957	0.898
29.64	2.960	16.85	127.8	0.961	0.949	0.876
40.20	2.933	16.68	124.2	0.952	0.939	0.851
43.45	2.922	16.49	122.0	0.949	0.928	0.836
47.42	2.910	16.43	120.5	0.945	0.925	0.826
50.74	2.900	16.44	119.7	0.942	0.925	0.821
53.53	2.897	16.29	118.4	0.941	0.917	0.812

A least squares fit of the changes in the relative unit cell volume, V/V_o, with pressure yields (Fig. 3.1 a):

$V/V_o = 1 - 0.0005\ P/P_o + 3x10^{-5}\ (P/P_o)^2 \qquad R^2 > 0.998 \qquad (3.7)$

and $V_o = 145.9 \pm 0.1$ Å^3.

Fitting the same results to the Birch-Murnaghan equation [37] yields a K_o value of 183±4 GPa and 3.4±0.2 for Ko'. This K_o is higher than the same value measured by ultrasound on bulk samples of $Ti_3Si_{0.5}Ge_{0.5}C_2$ [52]. This value is also lower than the corresponding values for Ti_3SiC_2 [37], Ti_3GeC_2 (this work) and TiC [39] which implies, $K_o\ (Ti_3SiC_2) > K_o\ (Ti_3GeC_2) > K_o\ (Ti_3Si_{0.5}Ge_{0.5}C_2)$.

Comparing the relative change in volume (V/V_0) as a function of pressure P for Ti_3GeC_2, $Ti_3Si_{0.5}Ge_{0.5}C_2$ and Ti_3SiC_2 [37], there is little doubt that the substitution of Si by Ge in Ti_3SiC_2 results in a general reduction of the bulk moduli.

The relative changes in lattice parameters of $Ti_3Si_{0.5}Ge_{0.5}C_2$ are plotted in Fig. 3.1 b as a function of pressure. Least squares fits of the curves, yield:

$$a/a_o = 1 - 0.0015(P/P_o) + 7 \times 10^{-6}\ (P/P_o)^2 \qquad (3.8)$$

and

$$c/c_o = 1 - 0.0021\ P/P_o + 10^{-5}\ (P/P_o)^2 \qquad (3.9)$$

As it was observed in Ti_3SiC_2 [37] and Ti_3GeC_2 (this work), the decrease of the *c*-axis length is faster than that of the *a*-axis length, while the crystal structure is stable up to pressures of ~ 53 GPa.

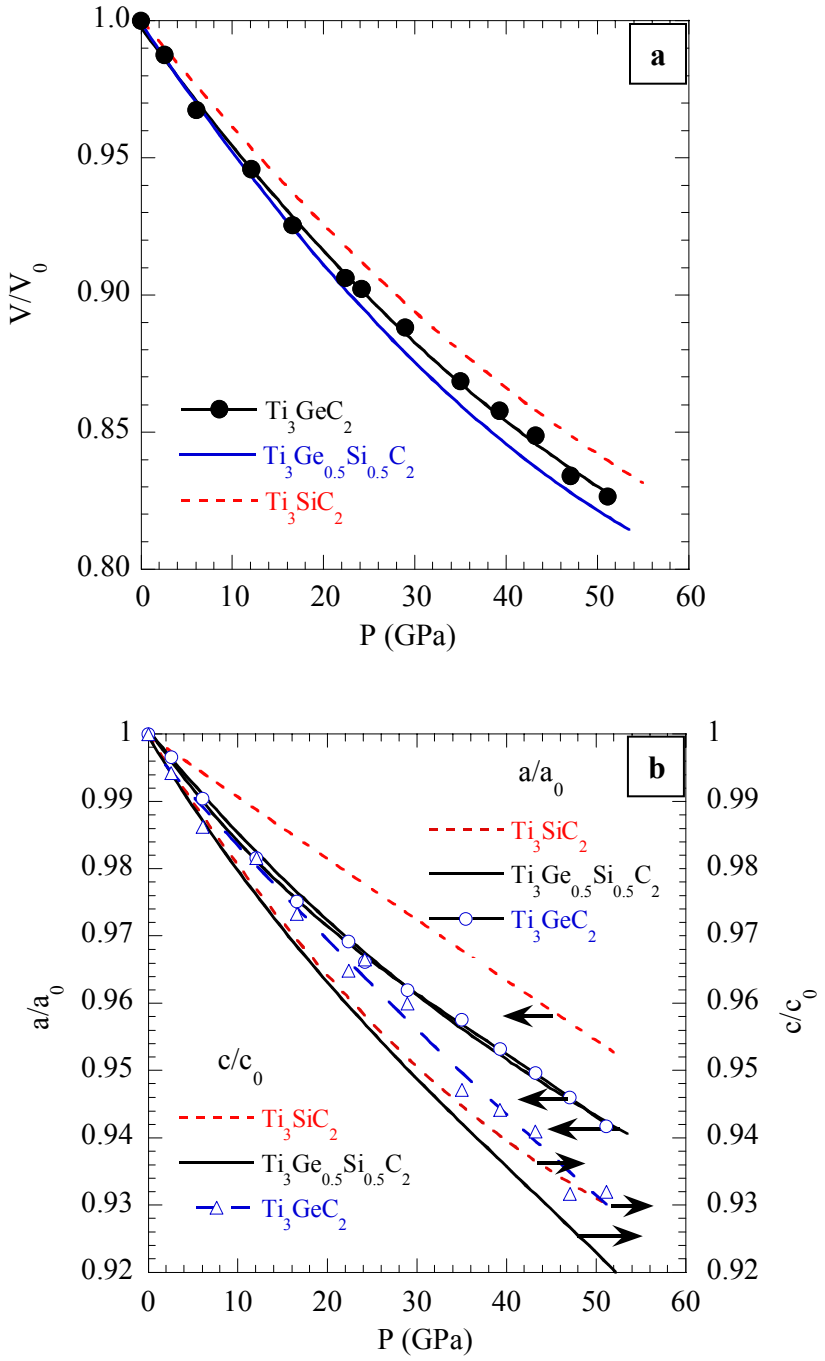

Figure 3.1: (a) Relative unit cell volume of Ti_3GeC_2 and $Ti_3Si_{0.5}Ge_{0.5}C_2$ as a function of pressure; (b) a/a_0 and c/c_0 of Ti_3GeC_2 and $Ti_3Si_{0.5}Ge_{0.5}C_2$ as a function of pressure. Also included in each case are the corresponding values for Ti_3SiC_2 [37].

Based on these results, it is fair to assume that thermal expansion anisotropy in Ti_3GeC_2 and $Ti_3Ge_{0.5}Si_{0.5}C_2$ would be similar to that in Ti_3SiC_2, with expansion along the c axis slightly larger than along the a axis [54, 55].

3.2.3.3 $Ti_3Al(C_{0.5}, N_{0.5})_2$

A summary of the relative changes in lattice parameters and unit cell volumes of $Ti_3Al(C_{0.5},N_{0.5})_2$ with pressure, P, are listed in Table 3.3.

Table 3.3 Relative unit cell parameters and volume of $Ti_3Al(C_{0.5}, N_{0.5})_2$ at various pressures.

P (GPa)	a/a_o	c/c_o	V/V_o
0	1	1	1
6.7	0.991	0.984	0.966
12.9	0.984	0.974	0.944
17.4	0.981	0.974	0.937
23.3	0.974	0.960	0.911
28.2	0.969	0.954	0.896
32.0	0.967	0.949	0.887
34.8	0.965	0.944	0.880
39.3	0.961	0.939	0.866
42.9	0.959	0.937	0.862
46.4	0.953	0.935	0.849
50.1	0.951	0.9317	0.842

A least squares fit of the changes in V/V_o, with P yields:

$$V/V_o = 1.0 - 3.06 \times 10^{-3}\ P/P_o - 2.73 \times 10^{-6}\ (P/P_o)^2 \qquad R > 0.99 \qquad (3.10)$$

where $V_o = 147.4 \pm 0.2$ Å^3.

Fitting the same results to the Birch Murnaghan equation [38] yields a K_o value of 219 ± 4 GPa, with a pressure derivative, K_o' of 3.7 ± 0.3 (if K'_o is fixed to 4, K_o = 207±2 GPa).

The value of K_o measured herein is one of the highest measured for any 312 MAX phase to date, it's also 15 to 17 % higher than that calculated for Ti_3AlC_2 [16, 56] which indicates that some type of solid solution stiffening occurred. However, current investigation on Ti_3AlC_2 has revealed that the K_o value (225 GPa) [29] is comparable to that of $Ti_3Al(C_{0.5},N_{0.5})_2$. It is worth mentioning here that some Sn was added to Ti_3AlC_2 used for this work. The nominal Ti:Al:Sn:C molar ratio being 3:1:0.2:2 (Appendix B) The Sn was added because it has been reported recently that its presence catalyses the formation of Ti_3AlC_2. The presence of this small amount of Sn did not significantly affect the results and the values obtained are believed to be representative of Ti_3AlC_2.

Figure 3.2 (a) shows the relative change in volume (V/V_0) as a function of pressure for these two compounds. Also plotted are the corresponding values of Ti_2AlC and Ti_2AlN [57].

Figure 3.2 (b) plots the relative changes in lattice parameters of $Ti_3Al(C_{0.5},N_{0.5})_2$ as a function of pressure. Also plotted are the corresponding values for Ti_3AlC_2. The crystal structure is stable to pressures of ≈ 51 GPa and the compressibility is anisotropic in each case. Like many other MAX phases, the relative shrinkage along the c-axis is larger than the a-axis.

Least squares fits of the curves shown in Fig. 3.2 (b), yield:

$$a/a_o = 1 - 6.92 \times 10^{-4} P/P_o - 4.23 \times 10^{-6} (P/P_o)^2 \quad (3.11)$$

and

$$c/c_o = 1 - 1.66 \times 10^{-3} P/P_o + 1.83 \times 10^{-6} (P/P_o)^2 \quad (3.12)$$

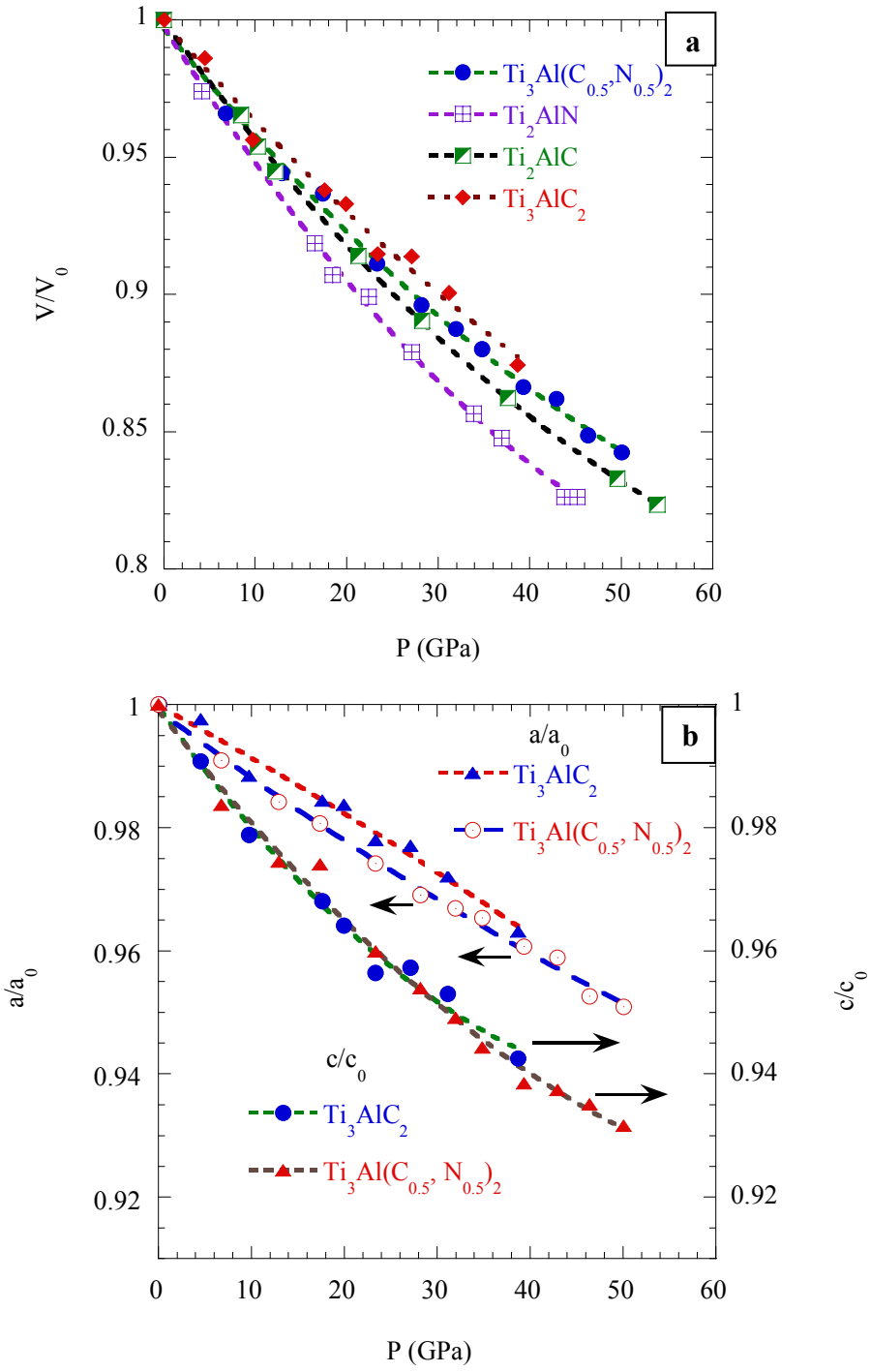

Figure 3.2: (a) Relative unit cell volume of Ti_3AlC_2 and $Ti_3Al(C_{0.5},N_{0.5})_2$ powders as a function of pressure; also included are corresponding values of Ti_2AlC and Ti_2AlN [57]; (b) a/a_0 and c/c_0 for Ti_3AlC_2 and $Ti_3Al(C_{0.5},N_{0.5})_2$ as a function of pressure.

Based on the results shown in Fig. 3.2 (a), there is little doubt that the addition of N to either Ti_2AlC or Ti_3AlC_2 decreases K_o. Furthermore, based on Fig. 3.2 (b), it is reasonable to conclude that this decrease results from a softening along the *a*- rather than along the *c*-axis. In other words, the replacement of C by N must somehow decrease the strengths of the Ti-X bonds more than the Ti-Al bonds. This is a somewhat surprising result because it is well established that replacing C by N in TiC results in an increase in K_o [41, 58]. Clearly, the Al atoms play an important modulating role here.

The results shown in Fig. 3.2 (a) also show that the 312 phases are stiffer than the 211 phases with the same A-group element, thus confirming the previous work of Barsoum et al. [1]. In the $Ti_{n+1}AlX_n$ compounds the Ti-Al bonds are somewhat more compressible than the Ti-X bonds (Figs. 3.2 a & b) and thus the 312's with their higher fraction of Ti-X bonds are indeed stiffer.

Previously, various authors [41, 58] have attempted to relate the elastic properties of solids to their electronic structure. Some suggested that there is a relationship between the elastic properties and the average valence electron concentration, VEC. Figure 3.3 plots the VEC *per Ti atom* for a number of MX and $Ti_{n+1}AlX$ compounds. The elastic properties and their correlation with VEC for the solid solution compositions explored in this work will be discussed in greater detail in the following subsection (3.3).

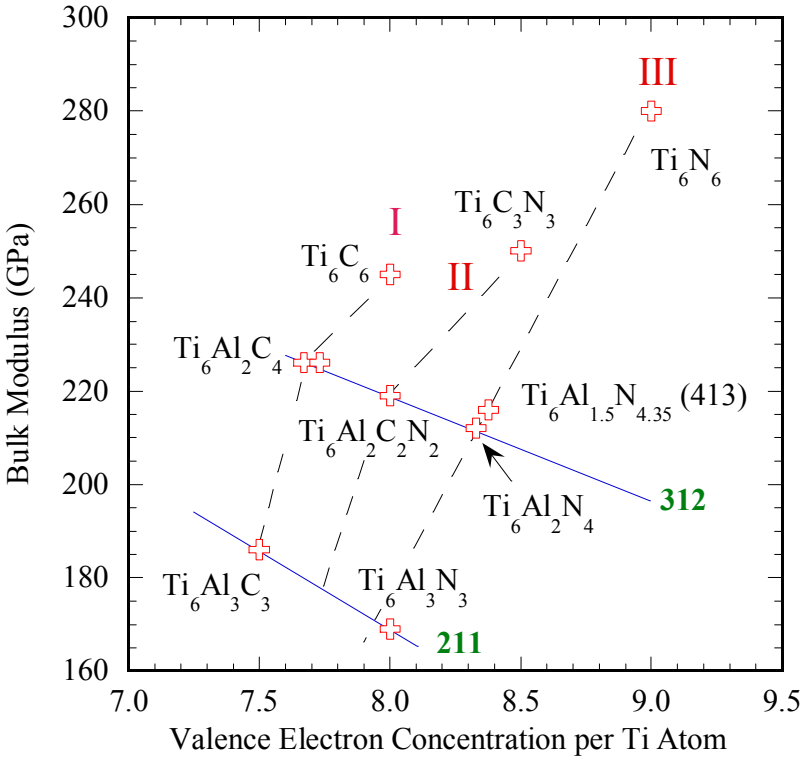

Figure 3.3: VEC per Ti atom vs. K_o for TiC-TiN, Ti_2AlC-Ti_2AlN (211) and Ti_3AlC_2- Ti_3AlCN (312) systems, respectively.

Referring to Fig. 3.3, the following points are salient:

a) A correlation exists between K_o and VEC. The R value for all the results shown in figure is 0.68.

b) Replacing C or N by Al (inclined dashed lines labeled I, II and III) results in a decrease in both VEC and K_o. The decrease in K_o, however, is much more severe for TiN than it is for TiC. The correlation along the dashed lines is quite high.

c) K_o of the MX binaries is higher than the 312 compounds, which, in turn, are higher than the 211 compounds. This is consistent with the fact that the Ti-Al bonds in the $Ti_{n+1}AlX_n$ compounds are more compressible than the Ti-X bonds.

d) For the MX compounds (top three points), replacing C with N results in an increase in K_o [58]. In contradistinction, replacing C with N in the ternaries results in a decrease in K_o, with the decrease being larger for the 211's than for the 312's (Fig. 3.3). Note that the actual composition of the 413 compound is $Ti_4AlN_{2.9}$, which is why the chemistry of that compound is the one given in Fig. 3.3 and not 413.

The simplest explanation for the last observation is that for the $Ti_{n+1}AlC_n$, compounds, excess electrons are pushed into antibonding orbitals. Another possibility is formation of vacancies on the N sublattice thereby affecting the chemistry of 211 systems.

3.3 Elastic Properties

The elastic constants are one of the fundamental parameters to be evaluated, for any solid, let alone newly synthesized ones. Thermodynamically, the elastic constants are defined by the shape of the interatomic bonding energy in the vicinity of the minimum. Therefore, any changes in crystal structure or the electronic character of solids are often revealed through changes in their elastic properties. The most important role of the elastic properties and their temperature dependence is that with their knowledge one could identify correlations between fundamental solid-state phenomena such as lattice

vibrations, theoretical strength, free energy, specific heat and thermal expansion coefficient. The elastic constants and associated physical parameters (i.e., the Debye temperature) allows a deeper understanding of the relationship between the mechanical properties and the electronic and phonon structure of materials in general. It is established that elastic properties also can be predicted from *ab initio* calculations.

The elastic properties of Ti_3SiC_2 were first measured by Pampuch *et al* [3, 42], who reported Young's, E_{RT} , and shear, μ_{RT}, moduli at room temperature for two different samples. For these samples, hot pressed at 1400 °C for two hours, E_{RT}, and μ_{RT} were 326±11 and 135±4 GPa, respectively. The corresponding values for samples that were sintered at 1600 °C for 2 hours were 286±2 and 120±1 GPa. Poisson's ratio, ν, was 0.193. The samples measured, however, were not single phase, but contained ≈ 10-20 vol. % TiC [42].

Barsoum and El-Raghy [1] in the preliminary work on single-phase pure Ti_3SiC_2, reported a room temperature Young's modulus of 320 ± 10 GPa. Recently, using an ultra sound echo-pulse technique, Finkel et al. reported on the elastic constants of Ti_3SiC_2 (E_{RT} ~ 322-339 GPa, μ_{RT} ~ 134-139 GPa) [43, 59], $Ti_3Al_{1.1}C_{1.8}$ (E_{RT} ~ 297.5 GPa, μ_{RT} ~ 124 GPa) and Ti_4AlN_3 (E_{RT} ~ 310 GPa, μ_{RT} ~ 127 GPa) [43] in the 20-300 K temperature range. Not surprisingly, given the similarities in structure and properties of these compounds, their moduli are all within 10% of each other. Consistent with these results is the fact that the thermal expansion coefficients of Ti_4AlN_3 [60], $Ti_3Al_{1.1}C_{1.8}$ [10] and Ti_3SiC_2 [54] are, respectively, 9.0×10^{-6}, 9.7×10^{-6}, and 9.2×10^{-6} K^{-1}. However all three ternaries are substantially stiffer than Ti (E_{RT} ~ 116 GPa, μ_{RT} ~ 43.6 GPa) [61] but less

stiff than $TiC_{0.97}$ (E_{RT} ~ 456-500 GPa, μ_{RT}~193 GPa) [39, 62]. The Debye temperature (θ_D) calculated for the three ternaries varied from 758 K ($Ti_3Al_{1.1}C_{1.8}$) to 780 K (Ti_3SiC_2) with Ti_4AlN_3 (762 K) in between [43].

To date only one study exists on the elastic properties of Ti_3SiC_2 determined from Resonant Ultrasound Spectroscopy (RUS) in the 300-1573 K [63]. The elastic moduli were observed to decrease linearly with temperature. RUS is a relatively novel technique, for determining the complete set of elastic constants of a crystal by measuring its free-body resonances [64-67]. In addition to the elastic constants, the RUS technique can also be applied to study the mechanical damping of any material under dynamic conditions as a function of temperature, grain size and deformation history.

This work reports on the room temperature elastic properties of Ti_3GeC_2, $Ti_3Si_{0.5}Al_{0.5}C_2$, $Ti_3Si_{0.5}Ge_{0.5}C_2$, and $Ti_3Al(C_{0.5}N_{0.5})_2$, $Ti_2Al(C_{0.5}N_{0.5})$ using ultrasound echo pulse technique and/or RUS [28, 52]. High temperature elastic properties of Ti_3GeC_2 and $Ti_3Si_{0.5}Al_{0.5}C_2$ in the 300-1573 K are also obtained using RUS. The results obtained herein are compared with those of Ti_3SiC_2 and Ti_2AlC, wherever applicable. The mechanical damping behavior of Ti_3GeC_2 and $Ti_3Si_{0.5}Al_{0.5}C_2$ obtained from RUS will be discussed in chapter 7.

3.3.1 Experimental Details

3.3.1.1 Ultrasound Echo-Pulse Technique

As has been established for a long time, one of the easiest techniques to measure elastic constants is one that uses a propagating sound wave. This approach is based on measurements of the time of flight, *t* (or round-trip transit time) of elastic waves in the material in order to obtain the sound velocity, V from V = 2L/*t*, where L is the specimen length and t is the time interval. When applied to isotropic materials, the elastic constants can be obtained from the longitudinal V_l and transverse (shear) *Vs* ultrasonic wave velocities. So far, the most accurate, precise and complete set of elastic constants has been determined by measuring the time of flight of a sound pulse.

The room-temperature elastic constants were determined with an ultrasonic echo-pulse technique using a RAM 10000 system from Ritec. The time of flight of a 10-MHz tone burst produced by a lithium niobate transducer was measured by heterodyne phase sensitive detection (PST). This setup measures the change in the time of flight by decomposing each individual echo into a quadrature and in-phase component and is capable of resolving relative changes in sound velocity with precision up to 10^{-5}. The PST also measures the absolute sound velocity in the material with an accuracy of about 0.5%.

For the ultrasonic measurements 8×8×8 mm^3 cubes of $Ti_3Si_{0.5}Ge_{0.5}C_2$ were used. For Ti_3GeC_2, the sample was cylindrical (10 mm in diameter and 16 mm long). In all cases Salol© was used as the ultrasonic transducer-bonding compound. Room temperature Young's E_{RT} and shear μ_{RT} moduli were calculated from independent measurements of the longitudinal V_l and shear *Vs* sound velocities, assuming an isotropic medium. Figure

3.4 shows the sample and the sample holder used in the ultrasonic velocity measurements setup.

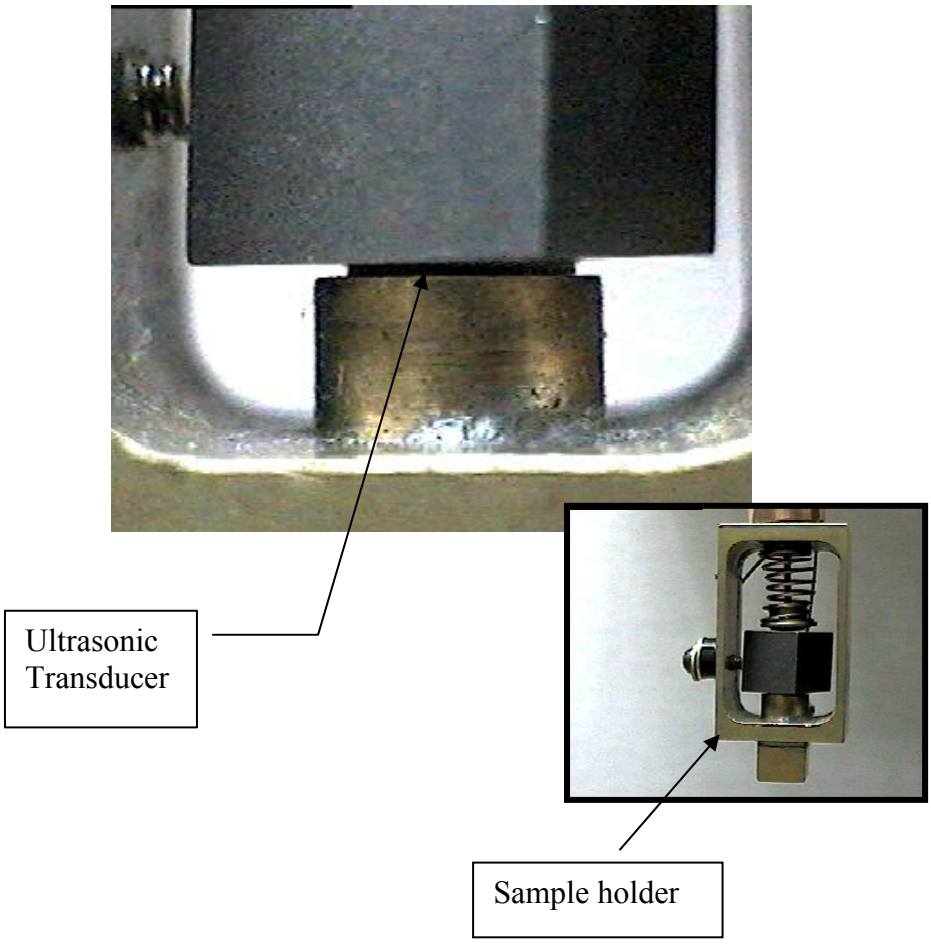

Figure 3.4: Photograph of the sample and sample holder used for the ultrasonic velocity measurements setup.

The elastic moduli were determined from *Vs* and V_L assuming the following equations [68]:

$$E = V_s^2 \, \rho \, \frac{(3V_L^2 - 4V_s^2)}{(V_L^2 - V_s^2)} \tag{3.13}$$

$$\mu = V_s^2 \rho \tag{3.14}$$

$$\nu = \frac{E}{2\mu} - 1 \tag{3.15}$$

where ν, is Poisson's ratio. Specimen density, ρ, was measured using Archimedes' principle.

The Debye temperature is calculated from the following expression [69]:

$$\theta_D = \left(\frac{h}{k}\right) \left(\frac{3 \, n \, \rho \, N_{Av}}{4 \, \pi \, m}\right)^{1/3} V_m \tag{3.16}$$

where:

h - Plank's constant

k - Boltzmann's constant

n - number of atoms per formula unit

N_{Av} – Avogadro's number

m – molecular weight

V_m - mean sound velocity defined by averaging the shear V_s and longitudinal V_L sound velocities, or

$$V_m = [\frac{1}{3}(\frac{1}{V_L^3} + \frac{2}{V_s^3})]^{-1/3} \quad (3.17)$$

3.3.1.2 Resonant Ultrasound Spectroscopy (RUS)

Figure 3.5 shows the experimental tripod set up used for RUS. The specimens are supported by three piezoelectric transducers; one generates an elastic wave of constant amplitude and varying frequency, and the other two detect the resulting signals. The complete set of elastic constants can be determined from the frequency of the resonant peaks in the RUS spectra for the known weight, geometry and dimensions of a freely suspended single crystal. For an isotropic elastic solid, like the polycrystalline samples examined herein, the number of independent elastic constants reduces to two, namely E and μ. The RUS spectra cannot be deconvoluted directly to deduce the elastic constants [64-67]. Instead, an approximate spectrum is calculated from the known sample dimensions, density, and a set of "guessed" elastic constants. A multidimensional algorithm (Quasar International 1, Albuquerque, NM) that minimizes the root-mean-square (RMS) error between the measured and calculated resonant peaks enables the determination of the elastic constants from a single frequency scan. In this work the first 40 resonance peaks were fitted for all specimens assuming elastic isotropy; i.e. only two independent elastic constants: E and μ. The measurements were performed in the 0-450 KHz frequency range.

At elevated temperatures, the samples were supported by sapphire elongation rods with semi-spherical tips that were located in a furnace. The other ends of the rods were attached to the transducers that were kept out of the furnace at room temperature. The

temperature was monitored by two thermocouples, one right above, and one right below, the sample. At each temperature, before a measurement was taken, the sample was held for 15 min. to reduce any temperature gradients. The temperature difference between the two thermocouples was ≤ 1 K. To avoid oxidation, the high temperature tests were carried out in an Ar environment. The oxygen concentration at high temperatures was monitored by an oxygen analyzer and was less than 100 ppm at all times.

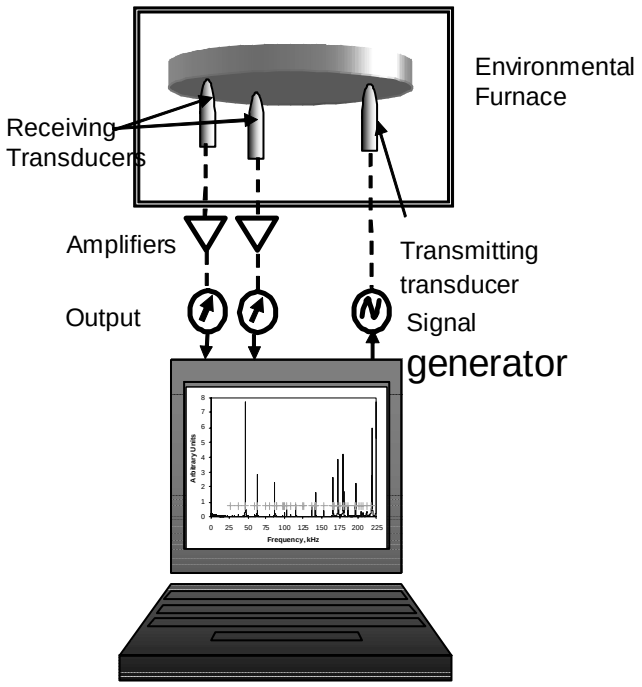

Figure 3.5: Experimental tripod set up used for Resonant Ultrasound Spectroscopy (RUS).

3.3.2 Results and Discussion

3.3.2.1 Ti_3GeC_2 and A-Site Substituted Solid Solutions

3.3.2.1.1 Room Temperature Elastic Properties

Table 3.4 summarizes all the results obtained in this work (both from RUS and the Ultrasound echo-pulse technique), including, measured densities, ρ, Poisson's ratio, ν, and rate of change of moduli with temperature $d(E/E_{RT})dT$ and $d(\mu/\mu_{RT})dT$ [28, 52]. Also included are results for some of the MAX phases explored eslewhere [42], as well as near stoichiometric TiC [70, 71]. The moduli of $Ti_3Si_{0.5}Ge_{0.5}C_2$ (E_{RT} ~ 310 GPa, μ_{RT}~130 GPa) obtained from the Ultrasound echo pulse technique were found to be ~ 10% lower than those of the end members, while those of $Ti_3Si_{0.5}Al_{0.5}C_2$ (E_{RT} ~ 322 GPa, μ_{RT}~136.8 GPa) obtained from RUS were observed to be in between those of Ti_3SiC_2 and Ti_3AlC_2. All sound velocities measured herein are lower than those for near stoichiometric TiC. For the isostructural 312 phases, V_l and V_s, obtained from RUS decrease in the following order: Ti_3SiC_2>$Ti_3Si_{0.5}Al_{0.5}C_2$ >Ti_3AlC_2 >Ti_3GeC_2 (Table 3.4). Similarly when using the ultrasound echo pulse technique a similar pattern emerges: Ti_3SiC_2>$Ti_3Si_{0.5}Ge_{0.5}C_2$> Ti_3GeC_2. Given that the values for the solid solutions are in between those of the end members, it is fair to conclude that substitutions on the A-sites do not greatly affect the elastic properties.

The Debye temperatures calculated herein from sound velocities are all above 700 K. Gratifyingly, the order of the Debye temperatures for the 312 phases – from high to low - is identical to that of the sound velocities. This is not too surprising since the densities of the examined samples are comparable.

Table 3.4 Summary of Ultrasound echo pulse technique and RUS results obtained in this work [28, 52]. Also included are values obtained previously and the corresponding values for near stoichiometric TiC [70, 71].

Sample	Ti_3SiC_2		$Ti_3Si_{0.5}Al_{0.5}C_2$	Ti_3AlC_2	$TiC_{0.98}$
	RUS [28]	Ultrasound [43]	RUS [28]	Ultrasound [43]	Ultrasound [70, 71]
ρ (g/cm^3)	4.5	4.5	4.35	4.2	4.98
E (GPa)	343	339	322	297.5	436
G (GPa)	143.8	142	136.8	124	184
B (GPa)	185.6	187	166	165	233
ν	0.192	0.200	0.176	0.200	0.187
$d(E/E_{RT})dT$, (K^{-1})	-1.38×10^{-4}	-0.75×10^{-4}	-1.29×10^{-4}	-0.84×10^{-4}	-0.95×10^{-4}
$d(\mu/\mu_{RT})dT$, (K^{-1})	-1.57×10^{-4}	-1.4×10^{-4}	-1.44×10^{-4}	-1.20×10^{-4}	-1.05×10^{-4}
V_l (ms^{-1})	9185	9142	9015	8880	9429
V_s (ms^{-1})	5670	5613	5650	5440	5856
θ_D (K)	813	784	795	758	929

Table 3.4 (*continued*)

Sample	Ti_3SiC_2		$Ti_3Si_{0.5}Ge_{0.5}C_2$	Ti_3GeC_2	
	RUS [28]	Ultrasound [43]	Ultrasound [52]	RUS [28]	Ultrasound [52]
ρ (g/cm^3)	4.5	4.5	5.01	5.29	5.35
E (GPa)	343	339	310	321	340
G (GPa)	143.8	142	130	135	142
B (GPa)	185.6	187	169	184.8	186
ν	0.192	0.200	0.2	0.196	0.19
$d(E/E_{RT})dT$, (K^{-1})	-1.38×10^{-4}	-0.75×10^{-4}	-----	-1.38×10^{-4}	
$d(\mu/\mu_{RT})dT$, (K^{-1})	-1.57×10^{-4}	-1.4×10^{-4}	-----	-1.35×10^{-4}	
V_l (ms^{-1})	9185	9142	8262	8424	8230
V_s (ms^{-1})	5670	5613	5096	5182	5063
θ_D (K)	813	784	728	728	725

It has been shown in the previous section that a correlation exists between the average VEC per Ti atom and K_o in these ternary compounds (Fig. 3.3). In a similar approach, VEC *per Ti atom*, Vickers Hardness (VHN) and μ are plotted here as a function of composition in the Ti_3SiC_2-Ti_3GeC_2/Ti_3AlC_2 systems (Fig. 3.6 a, b).

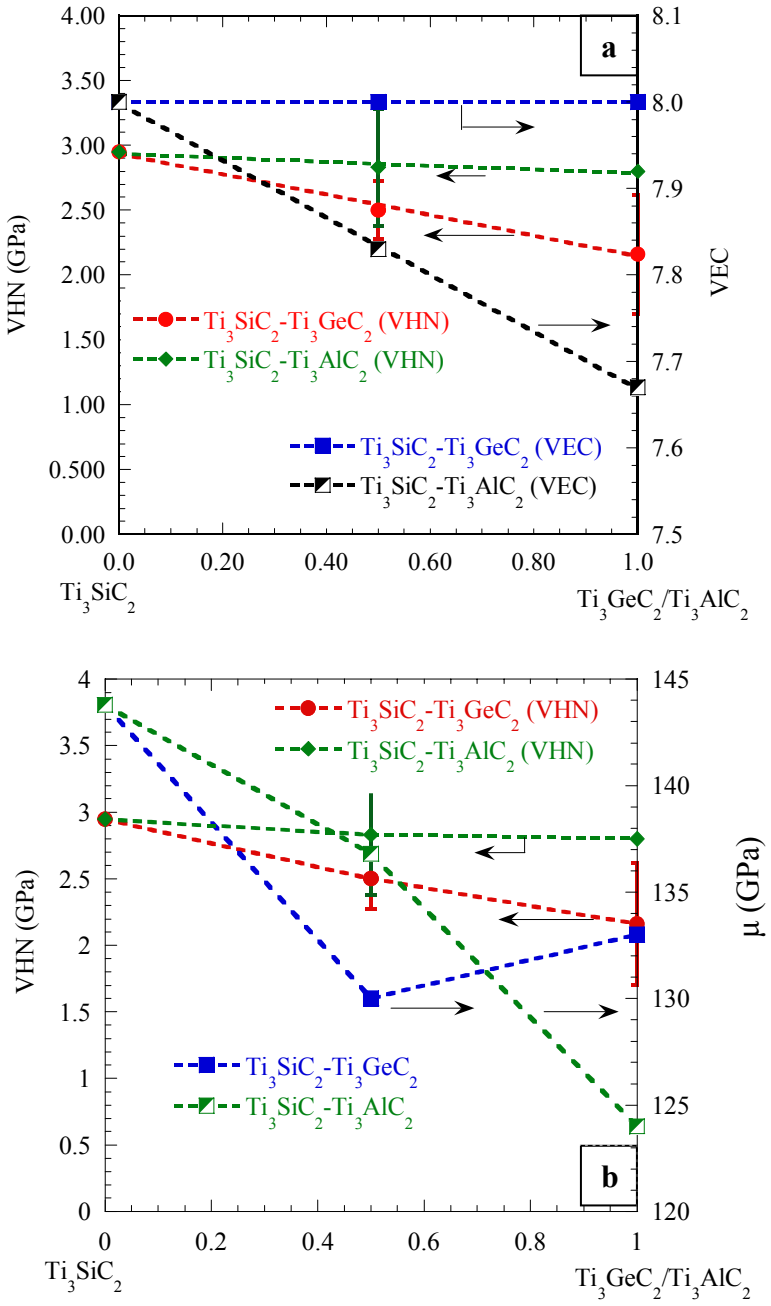

Figure 3.6: Vickers hardness (VHN) values and, (a) VEC, and, (b) shear moduli (μ) vs. composition in Ti_3SiC_2-Ti_3GeC_2/ Ti_3AlC_2 systems.

Referring to Fig. 3.6 the following points are salient:

(a) In the Ti_3SiC_2-Ti_3GeC_2 system, while the VEC is not affected by replacing Si by Ge, the hardness decreases monotonically without showing any maxima. This feature combined with the fact that μ goes through a minimum right at the 50-50 composition (Fig. 3.6 b), indicates that substitution of Si by Ge leads to some sort of softening in the system.

(b) In the Ti_3SiC_2-Ti_3AlC_2 system, both VEC and μ decrease monotonically, with little or no affect on the hardness as Si is gradually replaced by Al. This again indicates that substitution on the A-site leads to softening.

3.3.2.1.2 High Temperature Elastic Properties

Both, E and μ change linearly with temperature for Ti_3GeC_2 and $Ti_3Si_{0.5}Al_{0.5}C_2$ (Fig. 3.7). Also plotted are the corresponding values of Ti_3SiC_2 and Ti_2AlC for the sake of comparison [28]. The values of $d(\mu/\mu_{RT})/dT$ measured here varied from 1.35×10^{-4} K^{-1} for Ti_3GeC_2, to 1.44×10^{-4} K^{-1} for Ti_2AlC. These values are also in reasonable agreement with previous measurements [43]; an agreement that is noteworthy considering the very different temperature ranges over which the measurements were made (150–250 K in Ref. 43), the differences in techniques, as well as sample batches. Similarly, the values of $d(E/E_{RT})/dT$ range from a low of 1.29×10^{-4} K^{-1} for $Ti_3Si_{0.5}Al_{0.5}C_2$, to a high of 1.44×10^{-4} K^{-1} for Ti_2AlC. In this case the agreement with previous work [43] is less good. However, the good agreement between the values of $d(E/E_{RT})/dT$ and $d(\mu/\mu_{RT})/dT$ for all compositions measured herein probably indicates that these new values are more accurate. This is especially true for temperatures greater than ambient. It is also worth

nothing that the temperature dependencies of all examined $Ti_{n+1}AC_n$ phases are higher than those of TiC (Table 3.4). This is not too surprising given that in general the Ti-A bonds are slightly weaker than the Ti-C bonds [1].

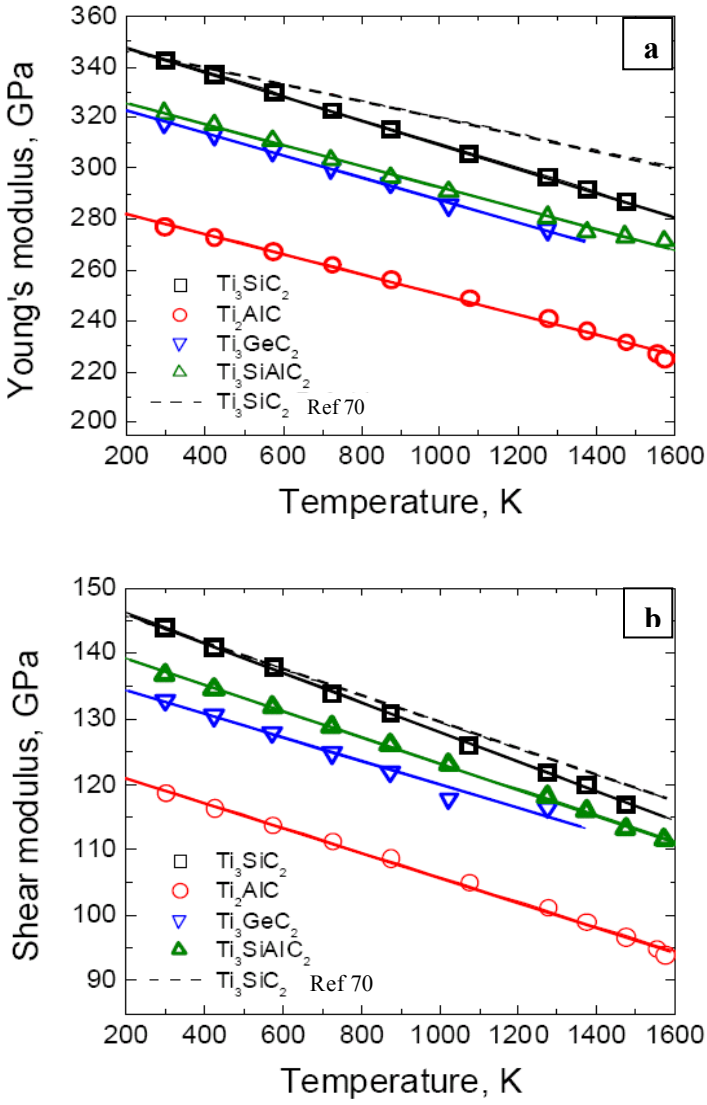

Figure 3.7: (a) Young's and (b) shear moduli of Ti_3GeC_2 and $Ti_3Si_{0.5}Al_{0.5}C_2$ as a function of temperature. Also plotted are corresponding values of Ti_3SiC_2 and Ti_2AlC [28] for the sake of comparison.

3.3.2.2 X-Site Substituted Solid Solutions

Table 3.5 summarizes the elastic properties of $Ti_3Al(C_{0.5},N_{0.5})_2$ and $Ti_2Al(C_{0.5},N_{0.5})$ measured by RUS. Also cited are the corresponding values for Ti_3AlC_2 [43], Ti_2AlC [28] and Ti_2AlN [72] for the sake of comparison. The moduli of $Ti_2Al(C_{0.5},N_{0.5})$ obtained from analyzing the room temperature RUS spectra - E_{RT} ~ 290 GPa, μ_{RT} ~ 122.6 GPa - were found to be higher than both end members. The same holds true for the 312 system. Both the Young's (E_{RT} ~ 330 GPa) and shear moduli (μ_{RT} ~ 137 GPa) of $Ti_3Al(C_{0.5},N_{0.5})_2$ were also considerably higher than those of Ti_3AlC_2 (E_{RT} ~ 297 GPa, μ_{RT}~124 GPa).

The V_l obtained from RUS or the Ultrasound echo pulse technique decrease in the following order: $Ti_3Al(C_{0.5},N_{0.5})_2$>$Ti_3AlC_2$>$Ti_2AlN$>$Ti_2Al(C_{0.5}, N_{0.5})$>$Ti_2AlC$; while V_s values obtained decrease in the following order: $Ti_3Al(C_{0.5},N_{0.5})_2$ > Ti_3AlC_2 > Ti_2AlC > $Ti_2Al(C_{0.5},N_{0.5})$ > Ti_2AlN.

The Debye temperatures (θ_D) calculated herein from sound velocities in this case are also above 700 K and the order of the Debye temperatures– from high to low - is identical to that of the shear velocities. It is worth noting here that θ_D for $Ti_3Al(C_{0.5},N_{0.5})_2$ is almost 800 K.

Table 3.5 Summary of RUS results for the X-site substituted solid solutions obtained in this work. Also included are values of the corresponding end members.

Sample	Ti_2AlC	$Ti_2Al(C_{0.5},N_{0.5})$	Ti_2AlN	Ti_3AlC_2	$Ti_3Al(C_{0.5},N_{0.5})_2$
	RUS [28]	RUS [This Work]	Ultrasound [72]	Ultrasound [43]	RUS [This Work]
ρ (g/cm^3)	4.0	4.19	4.3	4.2	4.5
E (GPa)	277.6	290	277	297.5	330
G (GPa)	118.8	123	112	124	137
B (GPa)	139.6	152	176.3	165	189
ν	0.169	0.182	0.238	0.200	0.209
$d(E/E_{RT})/dT$, (K^{-1})	-1.44×10^{-4}	----	----	-0.84×10^{-4}	----
$d(\mu/\mu_{RT})/dT$, (K^{-1})	-1.59×10^{-4}	----	----	-1.20×10^{-4}	----
V_l (ms^{-1})	8590	8670	8700	8880	9092
V_s (ms^{-1})	5423	5407	5100	5440	5514
θ_D (K)	741	738	730	758	795

It is worth mentioning here that the Bulk Modulus, B-$Ti_3Al(C_{0.5},N_{0.5})_2$> B-$Ti_3AlC_2$ [43], while K_o-$Ti_3Al(C_{0.5},N_{0.5})_2$ < K_o-Ti_3AlC_2. This is due to the fact that B from RUS or Ultrasound, unlike high pressure measurements, is calculated from μ and E. The higher values of B obtained from RUS, are in good agreement with the higher values of μ and microhardness values for the solid solution composition.

Figure 3.8 plots the VEC *per Ti atom*, Vickers Hardness (VHN) and μ as a function of composition for the Ti_3AlC_2-Ti_3AlN_2 (312) and Ti_2AlC-Ti_2AlN (211) systems. It is observed that replacing N by C atoms causes a monotonic decrease in the average VEC, while both VHN and μ go through maxima at the 50-50 composition in both the systems. Since Ti_3AlN_2 is not known to exist, the plot in case of 312 is completed using the corresponding values of Ti_4AlN_3 [43, 61]. It is evident from Fig. 3.8 that the solid solution compositions are harder and stiffer than the end members.

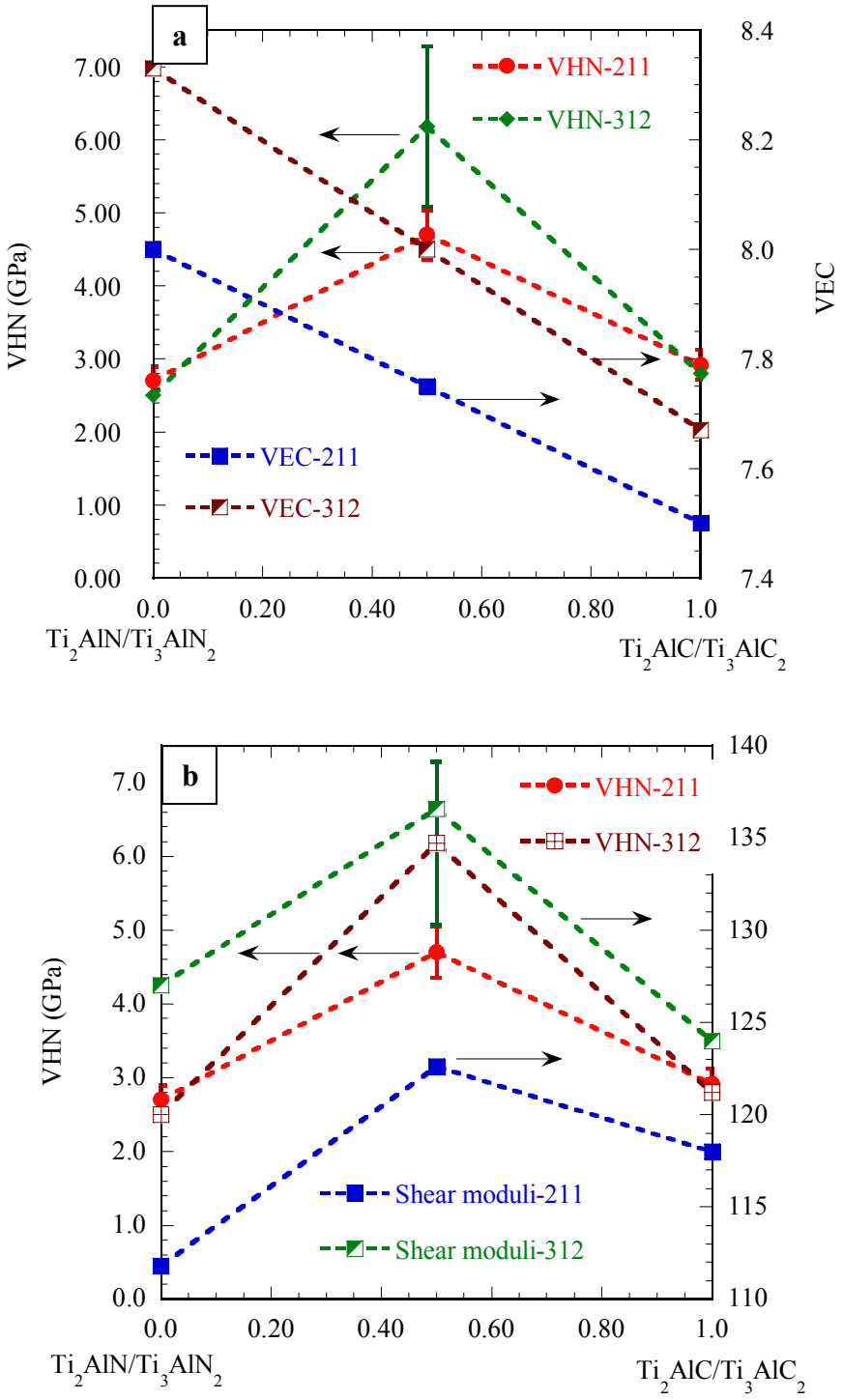

Figure 3.8: Vickers hardness values and, (a) VEC, and, (b) shear moduli (μ) vs. composition in Ti_2AlN/Ti_3AlN_2- Ti_2AlC/ Ti_3AlC_2 systems.

3.4 Coefficient of Thermal Expansion

The bulk dilatometric thermal expansion coefficients, TEC's, of the ternary MAX phases ranges from 7.5 to 10.5×10^{-6} K^{-1}[1]. For a given A element the TEC's of the ternaries scale with those of the corresponding MX binaries. Given the structural similarities, such a correlation, however is not surprising. Furthermore, since the TEC's of the ternaries are higher than their corresponding binaries, this implies the M-A bonds are, on average, weaker than the MC bonds. Considerable work exists on the influence of anisotropy on the TEC's of these ternaries. Barsoum et al. [54] for the first time determined from high temperature neutron diffraction that the thermal expansion anisotropy of Ti_3SiC_2 is moderate: 8.6×10^{-6} $^oK^{-1}$ along the *a*- direction and 9.7×10^{-6} $^oK^{-1}$ along the *c* direction which is in excellent agreement with the more recent values reported by Manoun et al. [55] who used high temperature X-ray diffraction.

The bulk TEC's of Ti_2AlC and Ti_2AlN were found to be comparable with the nitride being more isotropic [22, 73]. Interestingly, the bulk TEC value of $Ti_2Al(C_{0.5},N_{0.5})$ has been reported to be significantly higher than the end members indicating a solid solution softening in the system at high temperature [22]. In the Ti-Al-N system, the TEC of Ti_2AlN, along the a- and c-directions was observed to be lower than those of Ti_4AlN_3 [73] or the corresponding binary TiN [74]. The very fact that the replacement of N by Al in TiN enhances the bonding by lowering the TEC value, even though the number of valence electrons is reduced by two implies that some of the electrons in stoichiometric TiN are residing in anti-bonding orbitals [75]. This work however, focuses on the effect of substitution on the A- or X-site in the MAX ternaries on bulk dilatometric thermal expansion.

3.4.1 Experimental Details

Several bar shaped specimens with dimensions 2×2×25 mm^3 were electric discharge machined for the bulk thermal expansion coefficient measurements. The TEC was measured from 298 to 1273 K under Ar in an Anter Corporation Unitherm dilatometer. The measurements were carried out on heating and cooling at a rate of 3°C/min.

3.4.2 Results and Discussion

3.4.2.1 Substitution on the A-Sites

Figure 3.9 (a) plots the relative change in length (Δl/l) as a function of temperature (T) for Ti_3SiC_2-Ti_3GeC_2 system. The TEC of Ti_3GeC_2 (7.5×10^{-6} K^{-1}) is one of the lowest measured for a MAX phase to date.

The TEC values of both the solid solution compositions, $Ti_3Si_{0.5}Ge_{0.5}C_2$ and $Ti_3Si_{0.5}Al_{0.5}C_2$ (Fig. 3.9 b) are observed to be slightly higher than the end members, indicating a mild solid solution softening. Previously in this chapter it has already been shown that substitution of Si by Ge in Ti_3SiC_2 results in general reduction in the bulk (section 3.2) and shear moduli (section 3.3), indicating that substitution on the A-sites render the solid solution less stiff than the end members. The TEC results lead to the same conclusion.

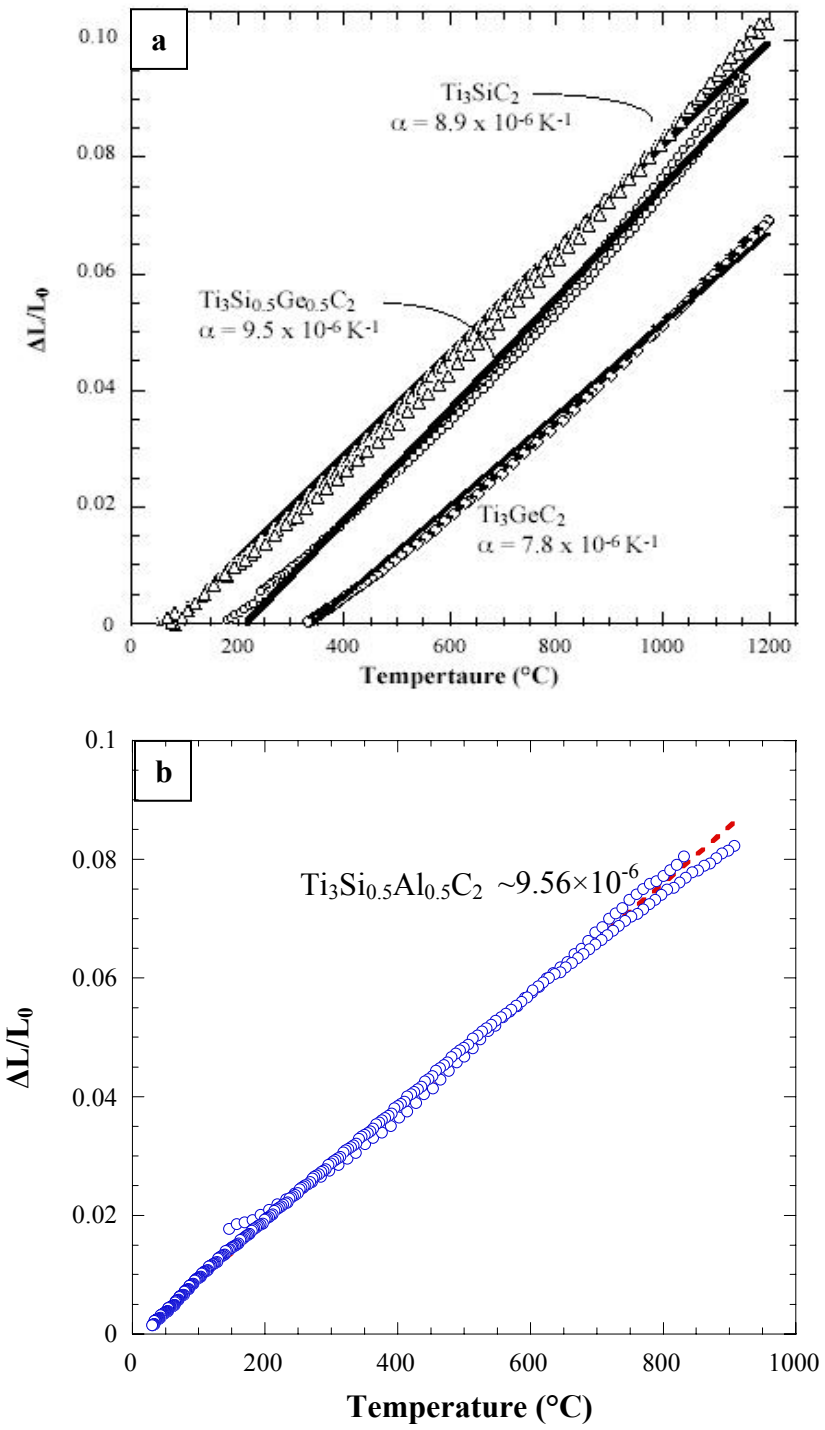

Figure 3.9: Relative change in length (Δl/l) as a function of temperature in (a) Ti_3SiC_2-Ti_3GeC_2 system (b) for $Ti_3Si_{0.5}Al_{0.5}C_2$.

Given the fact that both K_o and μ for Ti_3GeC_2 is lower than that of Ti_3SiC_2, one would anticipate higher TEC value for Ti_3GeC_2. However, the very fact, that the TEC value results the opposite is difficult to clarify at this point. A detailed study on the lattice expansions of Ti_3GeC_2 along a- and c-directions using high temperature neutron/X-ray diffraction might give a better understanding of the nature of the bond strength in this system.

Table 3.6 Summarizes the TEC values obtained in this work. Also included are corresponding values of Ti_3SiC_2 [1] and Ti_3AlC_2 [11] for the sake of comparison.

Table 3.6 Summary of TEC values in 312 system.

Compound	TEC ($\times 10^{-6}$)	Ref.
Ti_3GeC_2	7.8±0.2	[This Work]
$Ti_3Si_{0.5}Ge_{0.5}C_2$	9.5±0.1	[This Work]
Ti_3SiC_2	8.9-9.1	[1]
$Ti_3Si_{0.5}Al_{0.5}C_2$	9.56±0.2	[This Work]
Ti_3AlC_2	9.0±0.1	[11]

3.4.2.2 Substitution on the X-Sites

Figure 3.10 plots the relative change in length (Δl/l) as a function of temperature (T) for the two solid solution compositions explored here in.

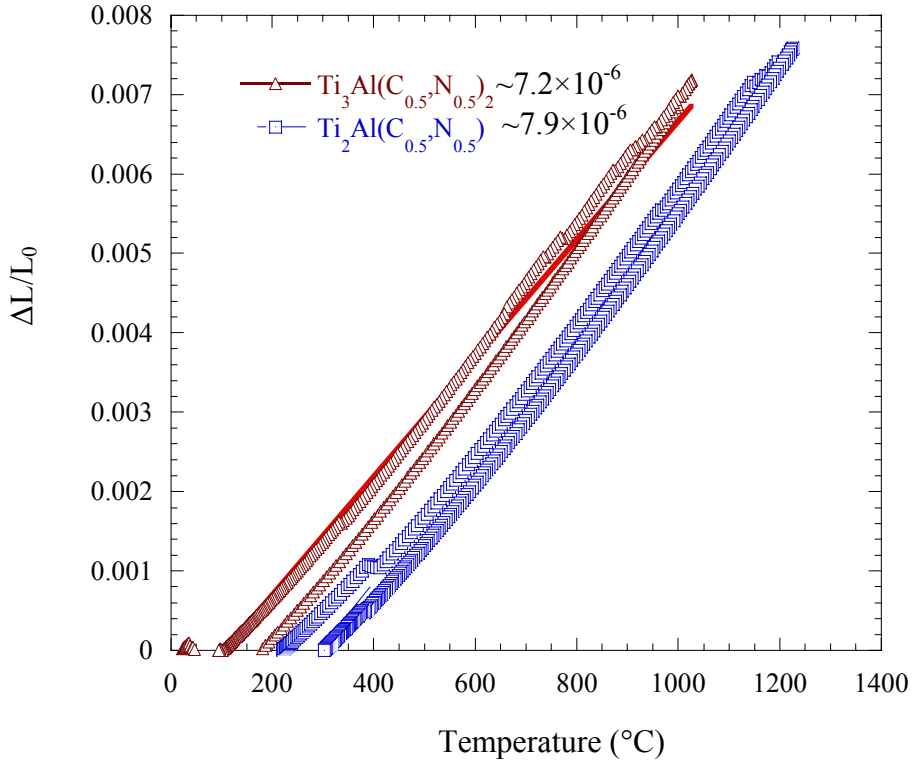

Figure 3.10: Relative change in length (Δl/l) as a function of temperature for $Ti_3Al(C_{0.5},N_{0.5})_2$ and $Ti_2Al(C_{0.5},N_{0.5})$.

Considering the fact that both the solid solution compositions are stiffer than the end members (section 3.2 and 3.3), it is expected that the corresponding bond strengths should be higher than the end members, thereby lowering the thermal expansion coefficients. The TEC values of the solid solution compositions obtained in this work are indeed lower than that of the end members [1]. However, the TEC value of $Ti_2Al(C_{0.5},N_{0.5})$ reported here is significantly lower than that reported in the previous work [22]. Given, the higher value of Young's and shear moduli, one would expect the

TEC value of $Ti_2Al(C_{0.5},N_{0.5})$ to be lower. Hence, the value reported in this work has to be more accurate. One possible reason for higher value of TEC in the previous work could be the presence of impurities/undesired phase(s) in the sample. Most likely, the source of such impurities was the starting powder Ti [*].

Table 3.7 summarizes the TEC values for the X-site substituted solid solutions. Also included are corresponding values of Ti_2AlC, Ti_2AlN, Ti_4AlN_3 [1] and Ti_3AlC_2 [11] for the sake of comparison.

Table 3.7 Summary of TEC values for X-site substituted solid solutions.

Compound	TEC ($\times 10^{-6}$)	Ref.	K_o	Ref.
Ti_2AlN	8.2	[1]	169	[59]
$Ti_2Al(C_{0.5},N_{0.5})$	7.9	[This Work]	-	-
Ti_2AlC	8.8	[1]	186	[59]
$Ti_3Al(C_{0.5},N_{0.5})_2$	7.2	[This Work]	219	[29]
Ti_3AlC_2	9.0	[11]	225	[29]
Ti_4AlN_3	9.7	[1]	216	[1]

* Private Communication-Barsoum M.W

From Table 3.7, it is apparent that partially replacing C by N atoms in both 312 and 211 system lowers the bulk TEC, thereby enhancing the bond strength in the system. The effect is certainly more pronounced in the 312 system than in 211. Given, the difference in shear moduli between Ti_3AlC_2 (125 GPa) and $Ti_3Al(C_{0.5},N_{0.5})_2$ (135 GPa), this observation, however, is not surprising. However, the compressibility results discussed in section 3.2 showed that the addition of N to either Ti_2AlC or Ti_3AlC_2 decreases the bulk moduli. The reason behind this discrepancy is due to the fact that calculation of the bulk modulus from the high pressure study does not take into account the shear modulus (unlike RUS or Ultrasound echo pulse technique). The low TEC value of the solid solution compositions are direct reflections of stiffer bonds which is well accounted for the high μ values for both the 211 and 312 solid solutions.

3.5 Conclusions

This section completes the study on the physical properties of the A or X-site substituted MAX solid solutions.

High pressure study of A-site substituted solid solutions shows that replacing Si by Ge atoms in Ti_3SiC_2 results in a general reduction in bulk moduli, thereby making the system more compressible. Similar to most MAX phases reported to date, the relative changes were more severe along the c- than that in the a-directions. This behavior, combined with the low value of μ for both the solid solution compositions ($Ti_3Si_{0.5}Ge_{0.5}C_2$ and $Ti_3Si_{0.5}Al_{0.5}C_2$) leaves little doubt that, substitution on the A site in

the 312 system leads to softening. This conclusion is consistent with the higher TEC values of the solid solution compositions relative to those of the end members.

A plot of VHN, VEC per Ti atom and μ as a function of composition in the Ti_3SiC_2-Ti_3GeC_2 system goes through a minima for VHN and μ at the solid solution composition, while no dependence of VEC on composition was observed. The values of the sound velocities and the Debye temperatures calculated for the solid solution $Ti_3Si_{0.5}Al_{0.5}C_2$ were also observed to fall in between those of end members.

Substitution on the X-site reveals the fact that replacing C by N gradually results in a reduction in the bulk moduli for both Al-based 312 and 211 systems, with the solid solution composition falling in between those of the end members. A plot of bulk modulus vs. VEC per Ti atom indicates the existence of a correlation (R~0.64). This observation is contradictory to the result obtained for MX binaries before, where replacing C by N atoms resulted in significant increase in bulk modulus. The simplest explanation for this observation is that for the $Ti_{n+1}AlC_n$, compounds, excess electrons are pushed into antibonding orbitals.

A plot of shear moduli μ, Vickers microhardness and VEC per Ti atom as a function of composition in the Al-based 312 and 211 systems goes through a clear maximum for VHN and μ at the 50-50 composition, while VEC decreases monotonically. From this behavior, it is fair to conclude that substitution in the X-site leads to a general stiffening.

High values of μ, combined with higher hardness for the solid solution compositions clearly indicates that substitution on the X-site results in solid solution hardening. This is in excellent agreement with previous work results [22]. Low values of TEC for the X-site substituted solid solutions suggests for the high bond strengths and in

turn supports the conclusions obtained from the elastic properties. The sound velocities and corresponding Debye temperature were observed to be highest for the composition $Ti_3Al(C_{0.5},N_{0.5})_2$ in the 312 and 211 Al-based systems, which is in accordance with the results of shear moduli and thermal expansion coefficients.

4: Low Temperature Electronic and Transport Properties

4.1 Introduction

To date the most studied of MAX phases materials is Ti_3SiC_2. It is a good thermal and electrical conductor. The room-temperature electrical conductivity is roughly twice that of pure Ti [1, 8], and more than 4 times that of near stoichiometric TiC [3, 8, 76]. Yoo *et al*. have shown that the thermoelectric power of Ti_3SiC_2 is negligible at least over the 300-850 K temperature range [8]. This fact led Barsoum *et al.* to the conclusion that Ti_3SiC_2 is a compensated conductor [76], in which the concentration of electrons, n, was equal to the concentration of holes, p. In addition, to account for the fact that the Hall coefficient fluctuated around zero, the mobilities of the holes and electrons were also assumed to be equal. However, recently Finkel et al. [77] have shown that the Hall coefficient while low, is not zero. Part of the problem in the previous work can be traced to the fact the experiment was performed in relatively low (0.8 T) magnetic fields causing the Hall voltage to be around the noise level of the measurements.

Finkel et al. characterized the electronic transport in Ti_3SiC_2 by performing electrical conductivity, Hall constant and magnetization measurements over the 4 to 300K temperature range and with magnetic fields up to 5T and proposed on the electronic conduction mechanism in Ti_3SiC_2 in light of the two-band model. The Hall coefficient was found to be almost independent of *H* and *T*. These, along with the fact that the MR is a quadratic function of *H*, imply that, as assumed earlier, [8] Ti_3SiC_2 is a compensated conductor with n~p.

Work on the low temperature electronic properties of two other members of MAX family; Ti_3AlC_2 and Ti_4AlN_3 suggests that at 0.39 μΩm, the room temperature resistivity of Ti_3AlC_2 [8, 11] is higher than that of Ti_3SiC_2 (0.22 μΩm) but roughly an order of magnitude smaller than that of Ti_4AlN_3 [8, 60]. More recent work [12] reported a lower room temperature resistivity of 0.285 μΩm, with a residual resistivity of ≈ 0.075 μΩm for Ti_3AlC_2. The resistance of Ti_4AlN_3 is high partly because of its high residual resistivity, which likely reflects the fact that its actual chemistry is 4:1:2.9 rather than 4:1:3 [25, 60].

Recently Finkel et al. reported on the electronic and magneto-transport properties of Ti_3AlC_2 and Ti_4AlN_3 [78]. The Hall effect, electrical conductivity, thermoelectric power, magnetic susceptibility and magnetoresistance were measured as a function of temperature between 4 and 300K and at magnetic fields up to 9 T. For Ti_3AlC_2, the Hall voltage was observed to vary linearly with magnetic field at all temperatures. At the lowest temperatures, the Hall coefficient was small but positive; above 100 K it was negative and dropped more or less linearly with temperature. The magnetoresistance of Ti_3AlC_2 was dominated by a positive quadratic field dependence. In contrast, the Seebeck coefficient remained positive up to 800 K, with a maximum at 700 K. The results were analyzed within a two-band model approach. The temperature dependence of ρ for Ti_3AlC_2 showed a typical metal-like resistivity; the residual resistivity, ρ_0, of 0.18 μΩm was found to be roughly six times higher than that of Ti_3SiC_2 ~0.033 μΩm [76] indicating the presence of a relatively larger defect concentration in Ti_3AlC_2 compared to the work of Zhou et al, where ρ_0 for Ti_3AlC_2 was reported to be ~ 0.01 μΩm [12].

The resistivity, magnetoresistance and Hall coefficient of Ti_4AlN_3, on the other hand, were successfully described within a single-band model, with holes as the dominant charge carriers. This was supported by measurements of the Seebeck coefficient which is positive and peaks at ≈ 300 K. The ρ vs. T curves for Ti_4AlN_3 were essentially parallel to those for Ti_3AlC_2 and Ti_3SiC_2, but were shifted vertically because of the significantly larger residual resistance ($\rho_0 = 2.35$ μΩm).

In an effort to understand the chemistry and/or physical property relationships in the MAX ternaries, Hettinger et al. [79] recently reported on the 5 to 300 K electrical resistivities, Hall and Seebeck voltages, magnetoresistances, and thermal and elastic properties of the Al containing phases: Ti_2AlC, V_2AlC, Cr_2AlC, and Nb_2AlC. The resistivities for all materials investigated drop linearly with decreasing temperatures, showing metal-like behavior. Of the materials measured, residual resistance ratio [RRR=ρ(300 K)/ρ(5K)] of V_2AlC was observed to be largest; of about 6.5, indicating a low defect density in this case. With the exception of Cr_2AlC, the Hall coefficients were found to be negative for all the other compositions explored. In general, the Seebeck coefficients were observed to be low with a tendency to fluctuate around zero. The low values of Hall and Seebeck coefficients indicate that the electronic conductivities in all these solids are also compensated with n~p.

The thermal conductivity of V_2AlC was reported to be highest, while that of Nb_2AlC, was the lowest. Given the fact, that the total thermal conductivity has both electronic and phonon contributions and the latter is sensitive to sample purity, the phonon conductivity was observed to be highest for V_2AlC. This is in good agreement with the low defect density and high RRR values obtained for V_2AlC.

This work, for the first time, investigates the effects of A-site [52] and X-site substitutions on the electronic properties in these ternaries. To study the effect of A-site substitutions, the following compositions were explored: $Ti_3Si_{0.5}Ge_{0.5}C_2$, $Ti_3Si_{0.75}Ge_{0.25}C_2$, $Ti_3Si_{0.5}Al_{0.5}C_2$. To observe the effect of X-site substitutions in the 312 and 211 system, the electronic properties of $Ti_3Al(C_{0.5}N_{0.5})_2$ and $Ti_2Al(C_{0.5}N_{0.5})$ were investigated.

4.2 Experimental Details

Several bar shaped specimen with dimensions $1\times1\times12$ mm^3 and $1.5\times2\times12$ mm^3 were cut for the transport measurements. The electrical resistivity ρ, Hall voltage, V_H, and magnetoresistance, MR = [ρ(B)-ρ(0)]/ ρ(0), were measured for temperatures T ranging between 5 and 300 K and for magnetic fields B, up to 9 T using Quantum Design's Physical Properties Measurement System (PPMS). A specially designed sample holder—with spring-loaded gold-coated contacts—was used to mount the samples for electrical transport measurements. The voltage measurement sensitivity was roughly 5 nV, and no contact heating was observed for currents up to 300 mA. Measurements were performed by a four-probe method to eliminate measurement of the contact resistance for these low resistivity materials. This configuration allowed a simultaneous measurement of the transverse and longitudinal magnetic-field-dependent voltages. The magnetoresistive component of the measured voltage and extraction of the Hall signal were achieved by magnetic field reversal and subtraction of the measured voltages to separate those components even and odd in the magnetic

field. Thermal voltages were eliminated from the measured values by use of a low frequency ac current technique.

The Seebeck voltages were also measured using the PPMS configured with the thermal transport option (TTO) from 5 to 300 K in zero magnetic field. The TTO allows sequential measurements of the thermal conductivity, Seebeck voltage, and electrical resistivity at each temperature. This measurement was made by attaching four leads to the sample with conducting silver epoxy. A temperature gradient was established by applying heat at one end of the specimen, while holding the other end at a constant temperature by maintaining good thermal contact with a low-temperature reservoir. Calibrated Cernox thermometers are attached to the sample between 4 and 7 mm apart. The temperature difference is monitored and the voltage measured at the same positions along the sample.

4.3 Results and Discussion

In the presence of two isotropic bands with different types of carriers (possessing different effective masses or signs), in a weak field limit, the magnetoresistance ρ(H) and Hall effect can be expressed respectively as [80]:

$$\rho(H) = \frac{\rho_1\rho_2(\rho_1+\rho_2) + (\rho_1 R_2^{\,2} + \rho_2 R_1^{\,2})B^2}{(\rho_1+\rho_2)^2 + (R_1+R_2)^2 B^2} \tag{4.1}$$

$$R_H = \frac{R_1\rho_2^{\,2} + R_2\rho_1^{\,2} + R_1R_2(R_1+R_2)B^2}{(\rho_1+\rho_2)^2 + (R_1+R_2)^2 B^2} \tag{4.2}$$

here R_i and ρ_i are the Hall constant and resistivity of the specific band, respectively. In the presence of a second group of degenerate charge carriers, the MR can be approximated and expressed in terms of mobilities, μ_I, of each band by:

$$\Delta\rho/\rho \approx \sigma_1\sigma_2(\mu_1 - \mu_2)^2 B^2/(\sigma_1 + \sigma_2)^2 \qquad (4.3)$$

where the σ_i's are the conductivities of each band. In the special case that the concentration of electrons, n, is equal to that of the holes, p, and given that the mobilities of the electrons, μ_n, is negative, while that of the holes, μ_p, is positive, Eq. 4.3 simplifies to:

$$\Delta\rho/\rho \approx |\mu_n\mu_p| B^2 \qquad (4.4)$$

wherein the MR is proportional to B^2. Thus the magnetoresistance coefficient α ($|\mu_n\mu_p|$) is an indirect measure of the mobility of the charge carriers.

Furthermore, in the low field limit, Eq. 10 can be expressed as:

$$R_H = (1/e)\,(\mu_p^2 p - \mu_n^2 n) / (p\,\mu_p + n\,\mu_n)^2 \qquad (4.5)$$

For n = p, it simplifies further to:

$$R_H = (1/ne)\,\{(1 - b^2)/ (1+ b)^2\} \qquad (4.6)$$

where $b = \mu_n/\mu_p$ – the ratio of mobilities. In this case, R_H is not a function of the magnetic field B.

4.3.1 Substitutions on the A-Sites

4.3.1.1 Resistivity, Hall Coefficient and Magnetoresistance Coefficient

Figure 4.1 presents the measured resistivities as a function of temperature. The resistivities for all compositions explored herein drop linearly with decreasing temperature. This metal like behavior, characteristic of all MAX phases explored to date, [77, 78, 79] and results from the large density of states at the Fermi level $N(E_F)$ of these solids [81, 82].

The residual resistance ratio (RRR), a measure of defect density for metal like materials, decreased in the following order: Ti_3SiC_2 (9.7)> Ti_3GeC_2 (5.6) > $Ti_3Si_{0.5}Ge_{0.5}C_2$ (3.3) > $Ti_3Si_{0.5}Al_{0.5}C_2$ (2.56). The resistivity of $Ti_3Si_{0.75}Ge_{0.25}C_2$ was almost indistinguishable from that of $Ti_3Si_{0.5}Ge_{0.5}C_2$. The higher residual resistivities in the solid solution compositions clearly suggest that solid solution scattering is operative in this system with the defect concentrations being highest in case of $Ti_3Si_{0.5}Al_{0.5}C_2$ (lowest RRR). Given the difference in atomic radii between Si (115 pm) and Al (145 pm), this observation, however, is, not too surprising.

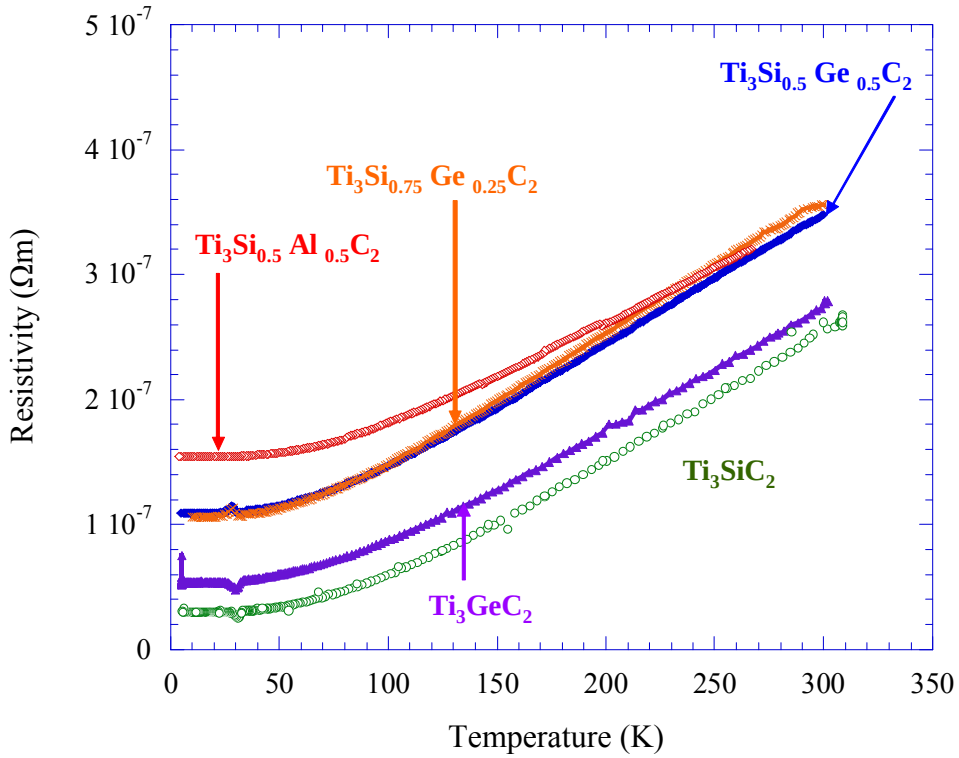

Figure 4.1: Resistivity as a function of temperature for A -site substituted solid solutions. Also included are corresponding values of the end members, Ti_3GeC_2 [this work] and Ti_3SiC_2 [77].

The temperature dependencies of R_H for the various compounds are plotted in Fig. 4.2. The R_H values are negative and small at the lowest temperatures and become more negative with increasing temperature. This observation is in good agreement with previous work on Ti_3SiC_2 [77], where also a relatively weak temperature dependence of R_H was reported.

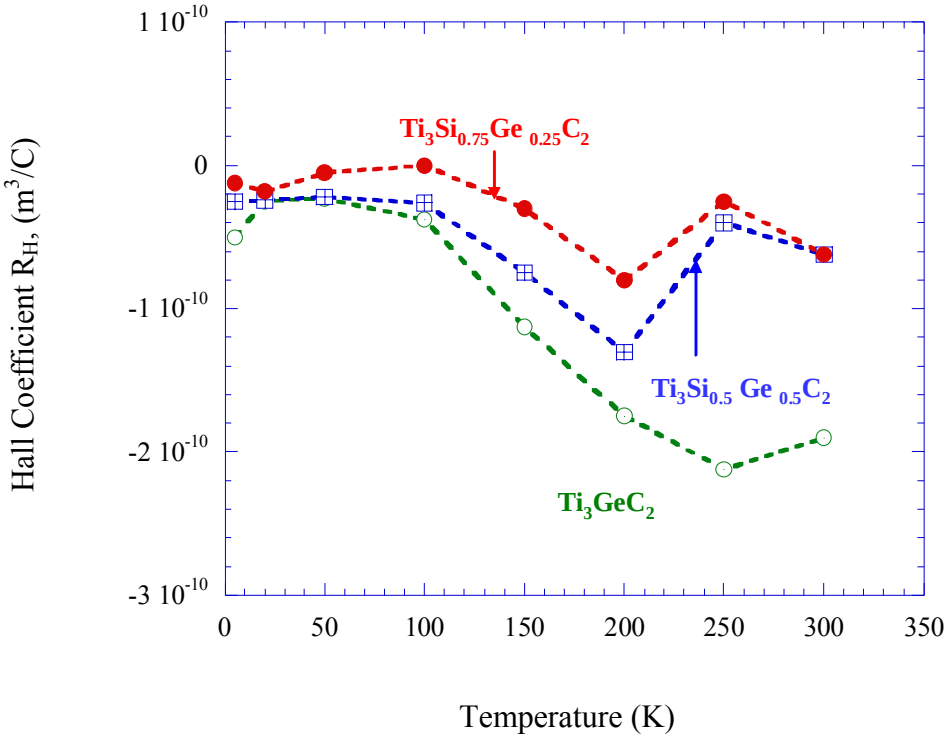

Figure 4.2: Temperature dependence of the Hall coefficient for A-site substituted solid solutions. Also included are the corresponding values of Ti_3GeC_2 [52].

As found for Ti_3SiC_2 and Ti_3AlC_2, [77, 78] the magnetoresistance (MR) of all phases could be well fitted by the expression $MR= [\rho(B)-\rho(0)]/ \rho(0) = \alpha B^2$, where α is a quadratic coefficient and B is the magnetic field. The temperature dependence of α for $Ti_3Si_{0.5}Ge_{0.5}C_2$ and Ti_3GeC_2 is plotted in Fig. 4.3.

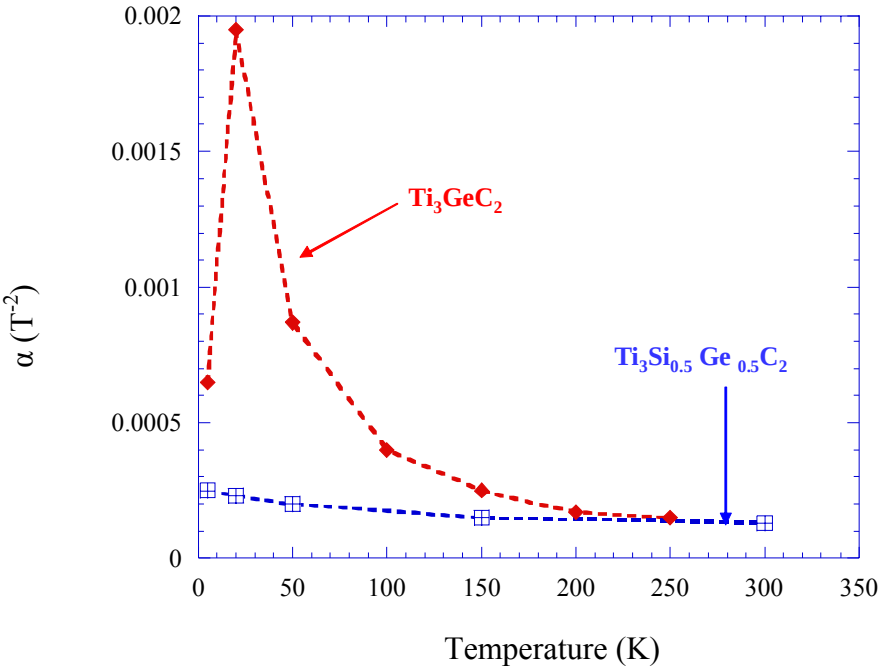

Figure 4.3: Temperature dependence of the magnetoresistance coefficient α for $Ti_3Si_{0.5}Ge_{0.5}C_2$ and Ti_3GeC_2 [52].

α of the solid solution composition, as expected, was observed to be lower than that of Ti_3GeC_2. At lower temperatures (up to 100 K) the effect is more pronounced, while near room temperature the α values are almost identical. This is due to the fact that α in a way is related to the mobilties of the charge carriers. At lower temperature both electron and hole mobilities are high, which accounts for the high value of α in the case of Ti_3GeC_2, while near room temperature α decreases significantly due to electron and hole scattering. However, the lower values of α for $Ti_3Si_{0.5}Ge_{0.5}C_2$

throughout are due to relatively high defect densities (lower RRR value) compared to that of the end members, reflecting a solid solution scattering effect.

4.3.1.2 Seebeck Coefficient

In the 5–300 K temperature range, the Seebeck coefficients of all compositions are weak functions of temperature and quite low; they fluctuate between ±2 μV/K [Fig. 4.4] with the exception of Ti_3AlC_2 (~5 μV/K) [72] , also shown for comparison purpose the Seebeck coefficient values for single crystal Ti [83].

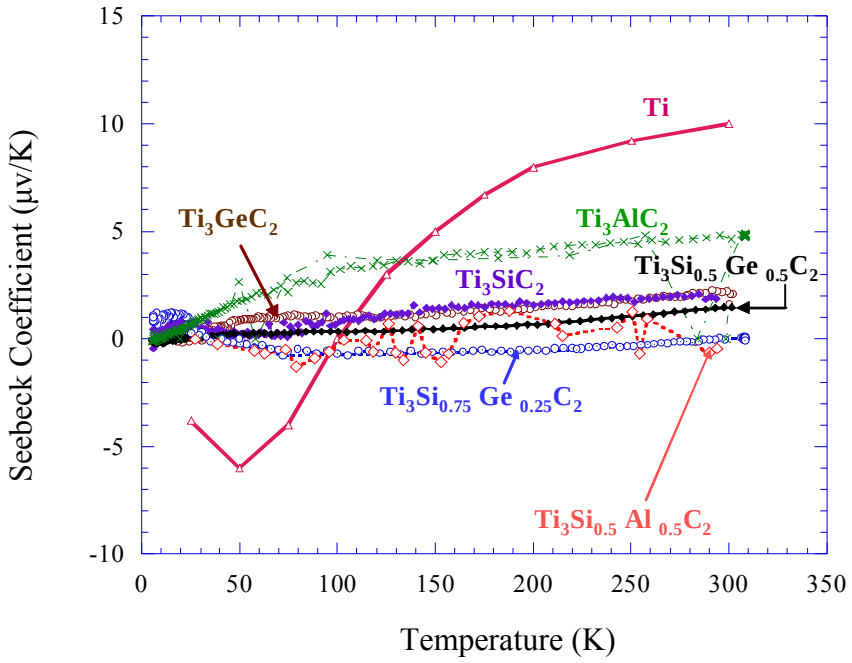

Figure 4.4: The Seebeck coefficient as a function of temperature for the A site substituted solid solutions [52]. Also included are the corresponding values of Ti_3GeC_2 [52], Ti_3SiC_2 [77], Ti_3AlC_2 [72] and single crystal Ti [83].

The weak temperature dependence of R_H, relatively small Seebeck coefficients and positive quadratic non-saturating magnetoresistance indicates that all the solid solution compositions explored are compensated conductors, like Ti_3SiC_2 (n~p) and a two band model is necessary to calculate the carrier concentrations and their respective mobilties.

4.3.1.3 Mobility Calculations

It has been mentioned in section 4.3.1.2 that a two band model is necessary to calculate the carrier concentrations and their respective mobilties. In the low-field limit of the two band model Eq. 4.3 and 4.5 apply. Also:

$$\sigma = 1/\rho = e(n\mu_n + p\mu_p) \qquad (4.7)$$

Based on the fact that the thermopower is negligible and the Hall coefficient is low and has a weak dependence of temperature it seems reasonable to assume n~p. From this, the value deduced for charge carrier concentrations for the solid solution compositions were about 2.25×10^{27} m^3. The electron and hole mobilties deduced assuming n~p are plotted in Fig. 4.5 (a, b). Not surprisingly the mobilities in the end members are higher than those for the solid solutions. This effect is indeed consistent with the fact that the α's for the solid solutions are also lower than those for either end members (Fig. 4.3). Also note that $R_H<0$ because $\mu_n>\mu_p$. The increasingly negative R_H, with increasing T, is probably due to the fact that the holes scatter more easily at high T than the electrons do. Table 4.1 summarizes the transport parameters for A-site substituted solid solutions. Also included are the corresponding values of Ti_3SiC_2 [8, 77], Ti_3GeC_2 [52], TiC_x [8] and Ti [8].

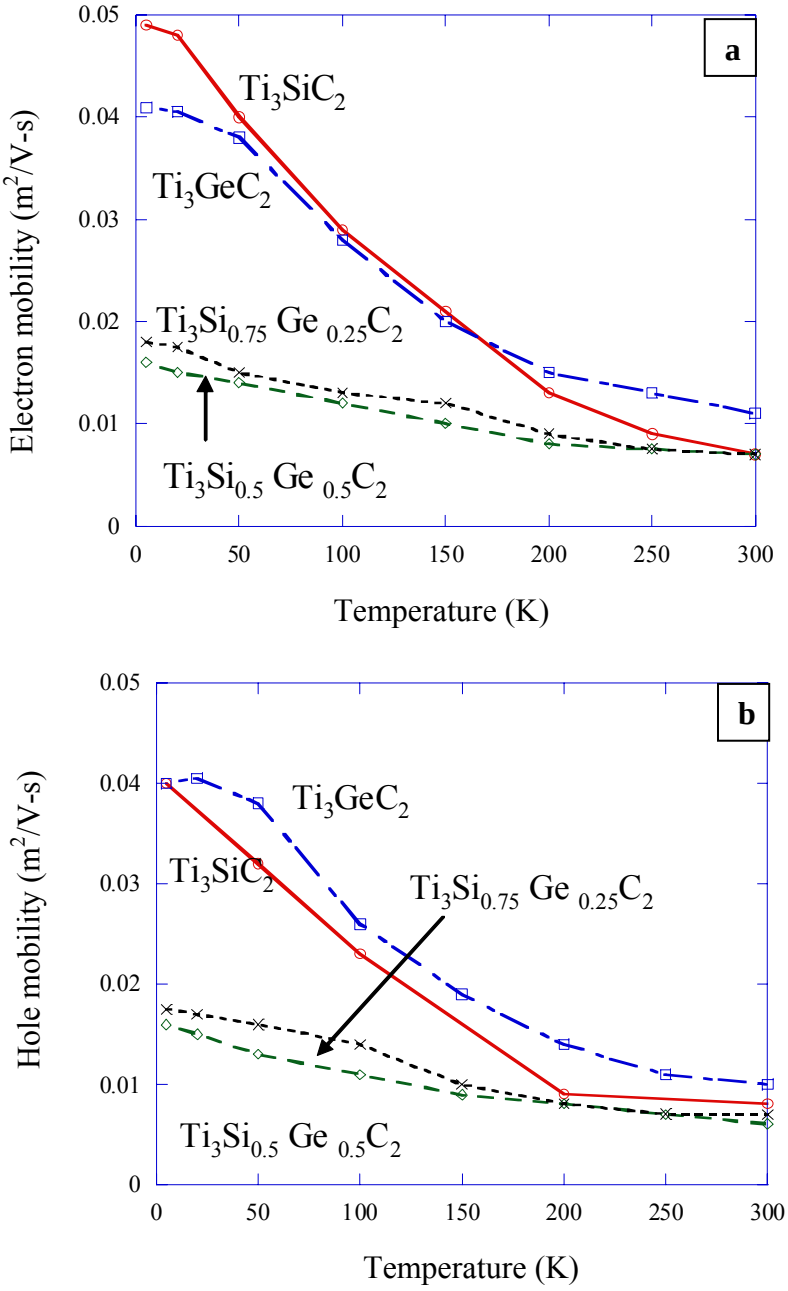

Figure 4.5: Temperature dependencies of the mobilities of, (a) electrons, and, (b) holes in the Ti_3SiC_2-Ti_3GeC_2 system.

Table 4.1 Summary of electrical transport parameters as calculated from room temperature resistivity, R_H and α for the A- site substituted solid solutions. Also included are corresponding values of the end members, Ti and TiC_x for comparison purposes.

Sample	R_H ($\times 10^{11}$) m^3/C	α (T^{-2}) (m^4/V^2s^2)	μ_n (m^2/V-s)	μ_p (m^2/V-s)	n ($10^{27}/m^3$)	p ($10^{27}/m^3$)
Ti_3SiC_2 [8]	-30	0.0003	0.007	0.006	2.4	2.4
$Ti_3Si_{0.5}Ge_{0.5}C_2$ [52]	-6.4	0.00013	0.007	.006	2.3	2.3
$Ti_3Si_{0.75}Ge_{0.25}C_2$ [52]	-6.2	-	0.007	.007	2.25	2.25
Ti_3GeC_2 [52]	-19.0	0.00015	0.011	.01	1.5-2.8	1.5-2.8
TiC_x [8]	-150 to -261	-	0.0012	-	0.24-0.4	-
Ti [8]	-4.5	0.0045	0.004	-	1.5	-

4.3.1.4 Thermal Conductivity

The room-temperature thermal conductivity κ of all phases is about 40 W/m- K range (Fig. 4.6) with the exception of $Ti_3Si_{0.5}Al_{0.5}C_2$ (~25 W/m-K).

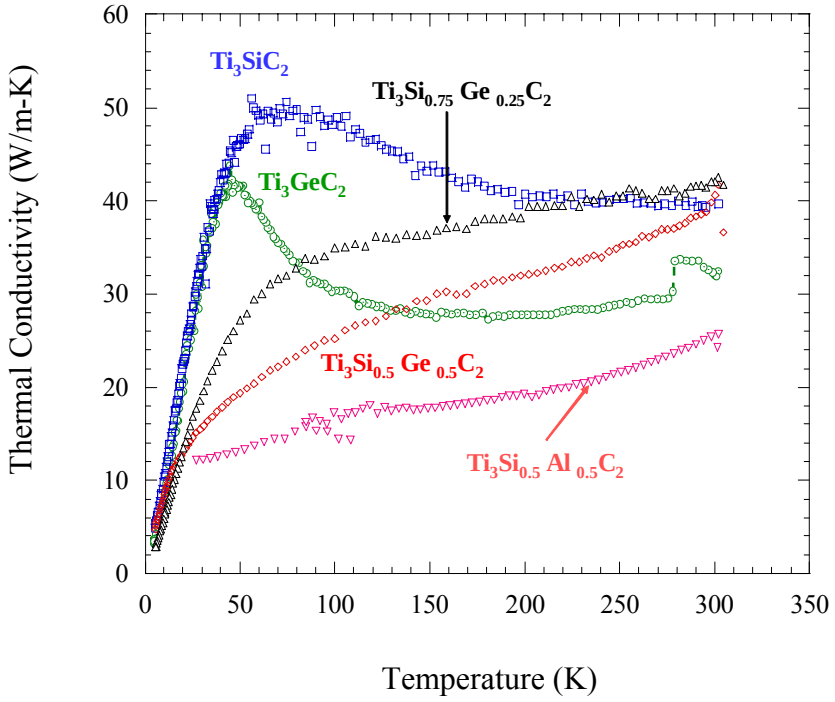

Figure 4.6: The thermal conductivity as a function of temperature for A-site substituted solid solutions. Also included are the corresponding values of the end members [52].

Considering the fact that the RRR for $Ti_3Si_{0.5}Al_{0.5}C_2$ is the lowest, a lower value of κ for this composition compared to all other compounds is not surprising. The end members show clear maxima in κ in the temperature range of 40 to 75 K. These

maxima are absent for the solid solution compositions. To appreciate this behavior of the end members it is imperative to be aware of the fact that total thermal conductivity has electronic and phonon contributions, κ_{el} and κ_{ph}, respectively. Since phonons are easily scattered by defects, they cannot contribute as strongly to the entropy transport in the 40-75 K temperature range in the case of solid solution compositions; where the effective defect density is higher than that of the end members. Hence no maxima in κ are observed for any solid solution compositions. To have a better understanding of this observation, the phonon conductivity ($\kappa_{ph} = \kappa - L_0/T\rho$, L_0=Lorenz number=2.45×10^{-8} V^2/K^2) for the solid solution composition $Ti_3Si_{0.5}Al_{0.5}C_2$ (with lowest RRR) is compared to that of the end members Ti_3SiC_2 and Ti_3AlC_2 [72] in Fig. 4.7. As expected the phonon conductivity of both the end members were observed to be much higher than that of $Ti_3Si_{0.5}Al_{0.5}C_2$ for the entire temperature range 5-300 K, which clearly indicates that the defect density of $Ti_3Si_{0.5}Al_{0.5}C_2$ is much higher than that of the end members. This is again in excellent agreement with the lowest RRR obtained for this particular composition.

It is also to be noted that to a lesser extent, the stiffness can also influence phonon conductivity, but only in compounds where κ_{ph} is large, and κ_{el} is small or very clean materials, which provide a long phonon mean path. To have a better insight in this case, the room temperature phonon conductivities and corresponding shear moduli for the Ti_3SiC_2-Ti_3AlC_2 system were plotted as a function of composition (Fig. 4.8). From Fig. 4.8 it is evident that even though the phonon conductivity goes through a minimum at the solid solution composition, the stiffness decreases monotonically, as Si atoms are being replaced by Al atoms, indicating that

lower phonon conductivity for the solid solution composition is due to it's higher defect density compared to that of the end members rather than being an influence of stiffness.

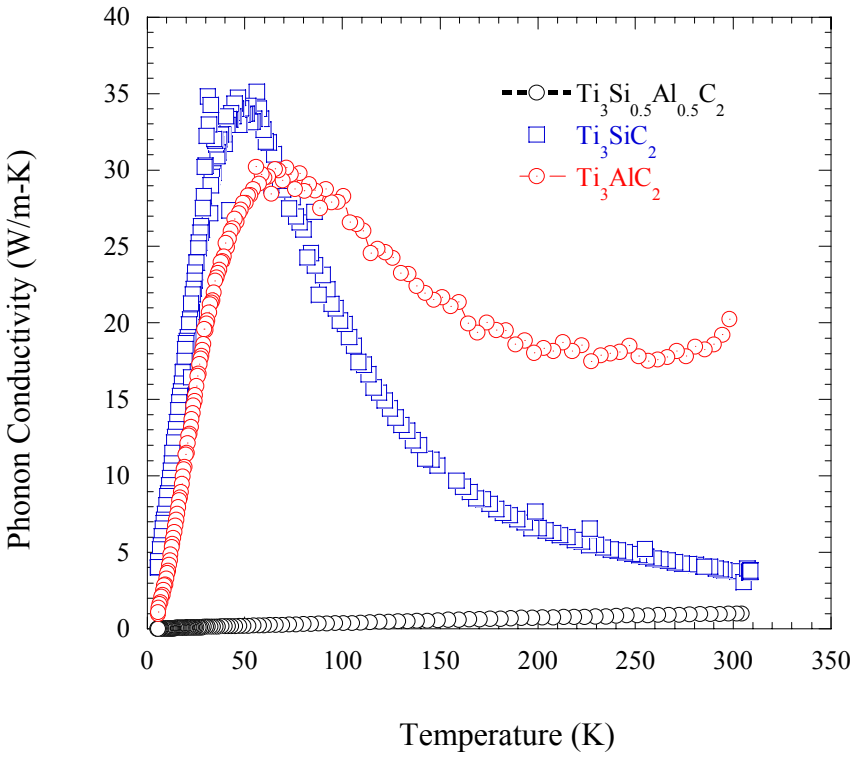

Figure 4.7: Phonon conductivity of $Ti_3Si_{0.5}Al_{0.5}C_2$ as a function of temperature. Also depicted are corresponding values of Ti_3SiC_2 [52] and Ti_3AlC_2 [72].

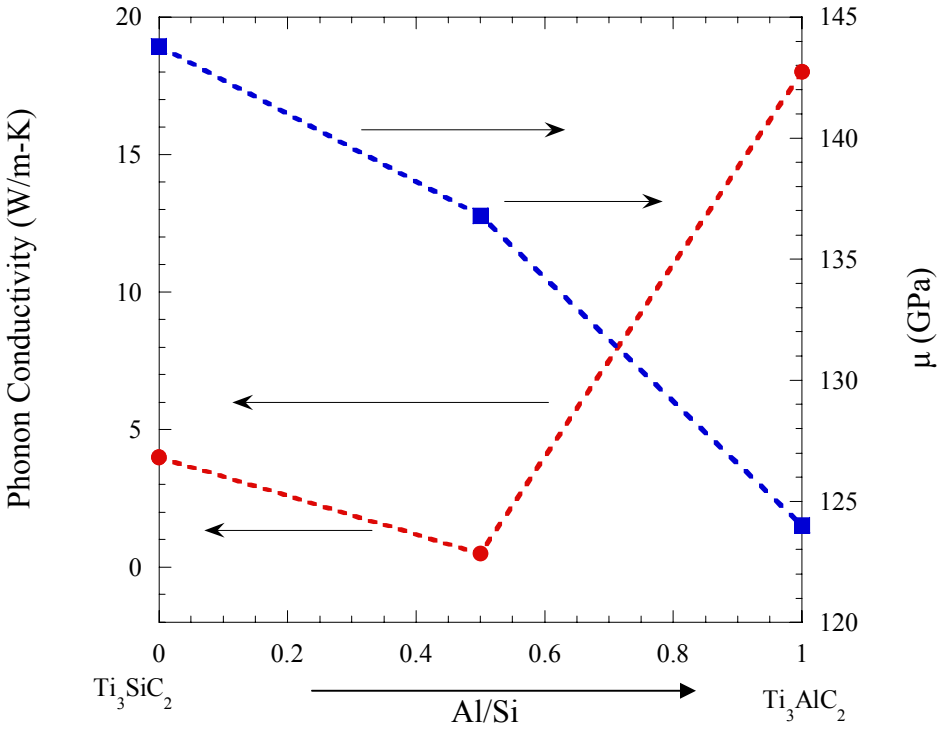

Figure 4.8: Room temperature phonon conductivity and shear moduli in Ti_3SiC_2-Ti_3AlC_2 system as a function of composition. The phonon conductivity goes through a minimum at the solid solution composition while the shear modulus decreases monotonically as Si atoms are gradually replaced by Al atoms.

4.3.2 Substitutions on the X-sites

4.3.2.1 Resistivity, Hall Coefficient and Magnetoresistance Coefficient

Figure 4.9 plots the resistivity as a function of temperature for the Ti_3AlC_2-Ti_3AlN_2 (312) and Ti_2AlC-Ti_2AlN (211) systems. The resistivity values for Ti_3AlC_2 plotted here are from the work of Zhou et al [12]. Here also, metal-like behavior is observed,

similar to all other MAX phases reported to date. Figure 4.9 (a) also plots the resistivity of $Ti_3Si_{0.5}Al_{0.5}C_2$ to compare the effect of substitution in the A-sites to that in the X-sites. The residual resistivity ratio (defined in section 4.1) decreases in the following order:

Ti_3AlC_2 (3.6) [12]> $Ti_3Si_{0.5}Al_{0.5}C_2$ (2.6) > $Ti_3Al(C_{0.5},N_{0.5})_2$ (1.45). From Fig. 4.9 (a) it is evident that $Ti_3Al(C_{0.5},N_{0.5})_2$ has the highest residual resistivity. This fact indicates that substitution in the X-sites also enhances the solid solution scattering. Figure 4.9 (b) plots the resistivity as a function of temperature for the 211 system. As anticipated, X-site substitutions in the 211 system also increases the residual resistivity and defect density of the solid solution $Ti_2Al(C_{0.5},N_{0.5})$ compared to that of the end members. The RRR decreases as follows: Ti_2AlN (10.25) [72]> Ti_2AlC (3.12) [79]> $Ti_2Al(C_{0.5},N_{0.5})$ (2.53). The lower residual resistivity for Ti_2AlN is related to the purity of that particular sample.

The temperature dependencies of R_H for $Ti_3Al(C_{0.5},N_{0.5})_2$ and $Ti_2Al(C_{0.5},N_{0.5})$ are plotted in Fig. 4.10. Also plotted are corresponding values of Ti_3AlC_2 [78] and Ti_2AlC [79]. Unlike the end members, the Hall coefficients for both the solid solution compositions are positive and have little or no dependence on temperature. From Fig. 4.10 it appears that replacing the C atoms by N atoms renders the holes (p) the dominant charge carrier for both solid solutions. It has been observed before [78] that nitride based samples (Ti_4AlN_3) have a relatively large positive value of R_H and the transport properties can therefore be calculated using a single band model. This observation is in good agreement with previous work [78].

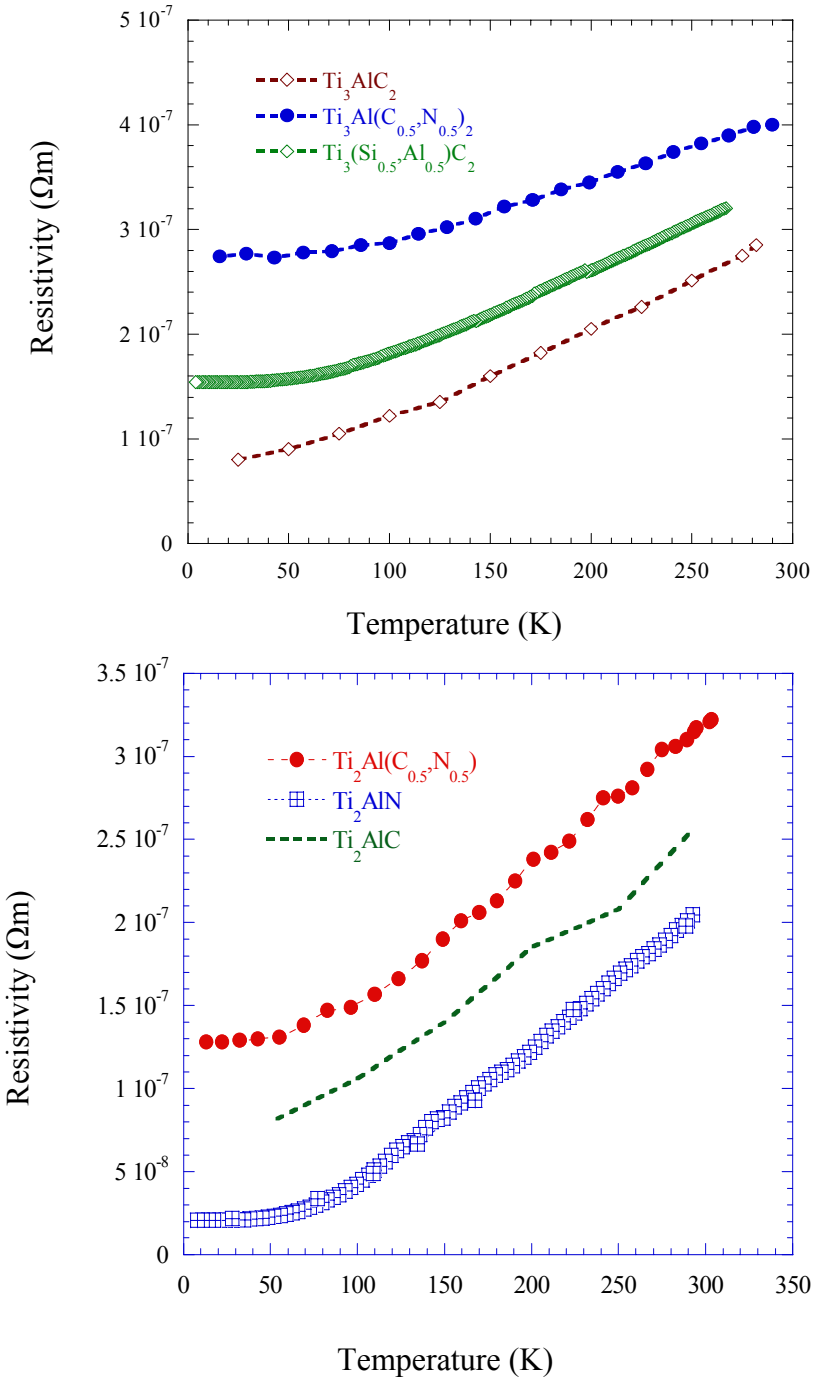

Figure 4.9: Resistivity as a function of temperature for, (a) Ti_3AlC_2 [12]-Ti_3AlN_2 (312), and, (b) Ti_2AlC [79]-Ti_2AlN (211) system.

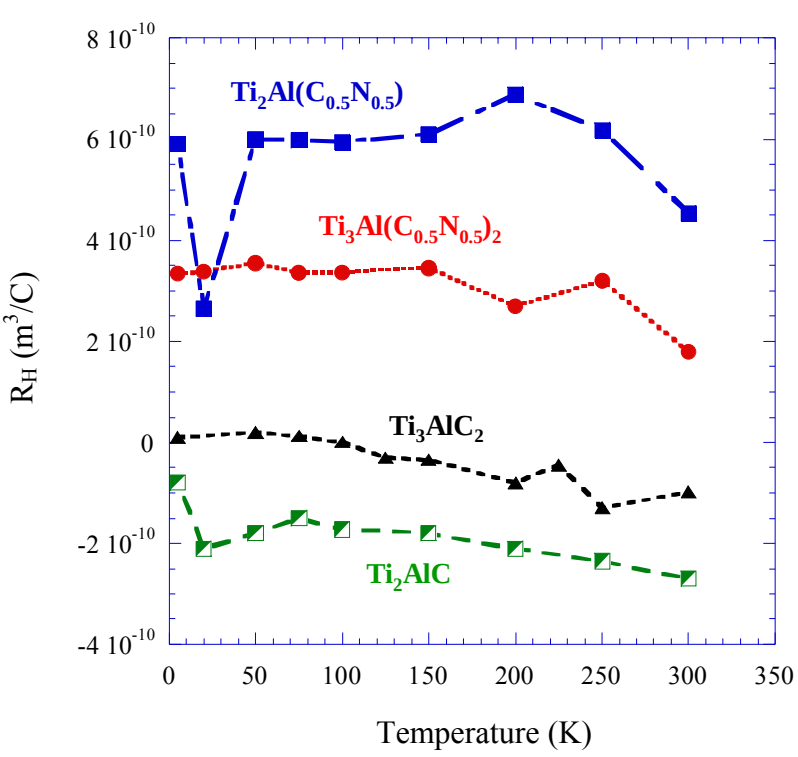

Figure 4.10: Temperature dependence of Hall coefficient for X- site substituted solid solutions. Also plotted are corresponding values of Ti_3AlC_2 [78] and Ti_2AlC [79].

The temperature dependence of α for $Ti_3Al(C_{0.5},N_{0.5})_2$ and $Ti_2Al(C_{0.5},N_{0.5})$ is plotted in Fig. 4.11 and is compared to that of the end members [78, 79]. As expected, α of $Ti_3Al(C_{0.5},N_{0.5})_2$ is lower than that of Ti_3AlC_2, which is accounted for by the high defect density and low RRR value for the solid solution composition. Surprisingly, α of $Ti_2Al(C_{0.5},N_{0.5})$ is quite comparable to that of Ti_2AlC. The main reason behind this is sample quality of Ti_2AlC. It has been already shown that the RRR value of Ti_2AlC is lower than that of Ti_2AlN, which indicates that the defect density in Ti_2AlC is high, which in turn lowers the mobility and hence α.

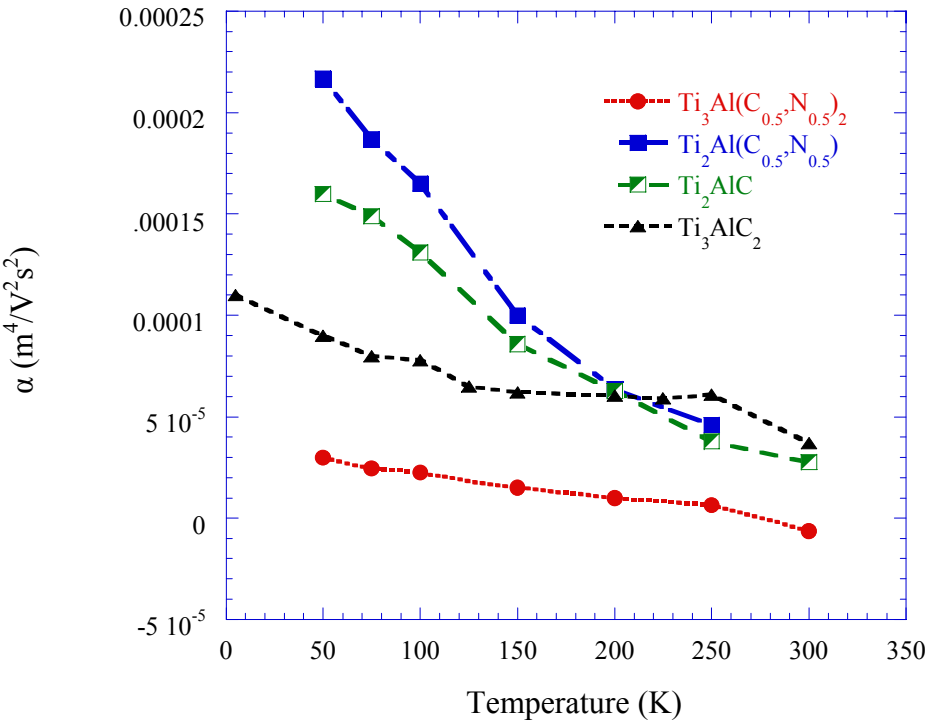

Figure 4.11: Temperature dependence of α for the X- site substituted solid solutions. Also plotted are corresponding values of Ti_3AlC_2 [78] and Ti_2AlC [79].

4.3.2.2 Seebeck Coefficient

Figure 4.12 plots the Seebeck coefficient for both the 312 and 211 systems. In each case, the gradual replacement of C by N atoms results in a significant increase in Seebeck coefficient to the positive side. This indicates that the presence of N atoms in the system increases the hole carrier concentration. The Seebeck coefficient was observed to be highest for $Ti_3Al(C_{0.5},N_{0.5})_2$ - room temperature value ~ 10μV/K and lowest for Ti_2AlC-room temperature value near zero. This result encourages one to

plot the R_H and the Seebeck coefficient for the 312 and 211 systems as a function of normalized concentration of N-$x_N/(x_N+x_C)$, where x_i is the molar concentrations of N or C on the X atom lattice. In other words, $x_N+x_C = 1$.

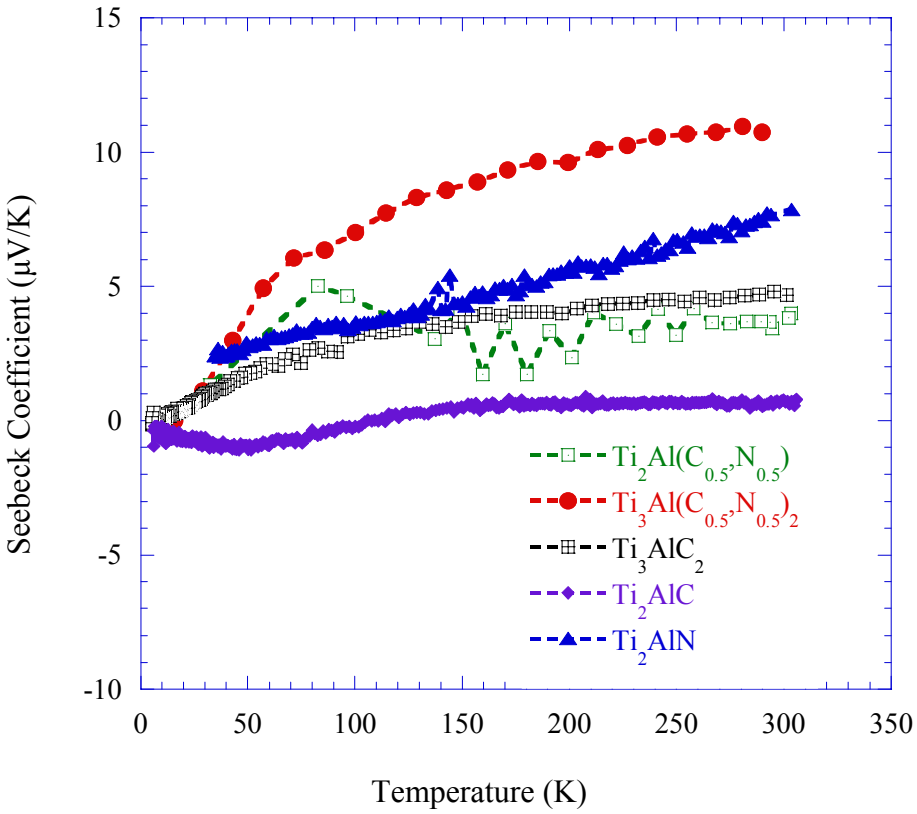

Figure 4.12: Seebeck coefficient for the X- site substituted solids solutions. Corresponding values of Ti_2AlC [79], Ti_2AlN [72] and Ti_3AlC_2 [78] are also incorporated for comparison.

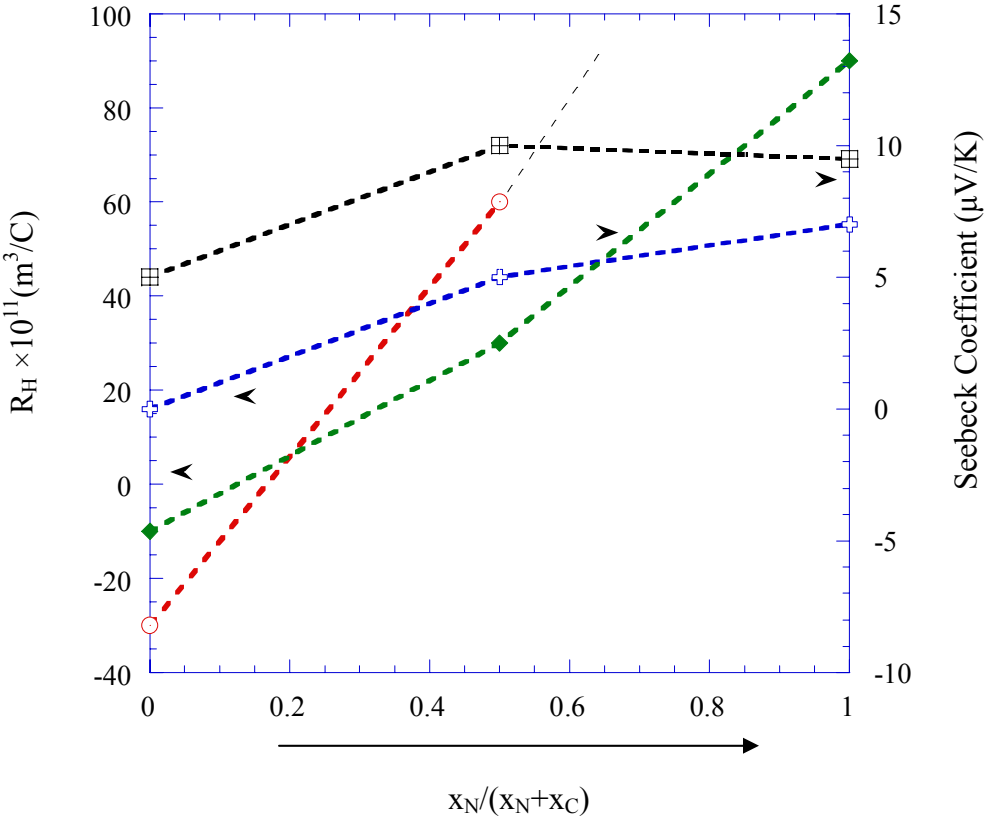

Figure 4.13: Room temperature values of Hall (R_H) and Seebeck coefficient for 312 and 211 systems as a function of normalized concentration of N.

Since Ti_3AlN_2 is not known to exist, values of Ti_4AlN_3 [78] are incorporated in the 312 system for the sake of comparison in Fig. 4.13.

It is apparent from fig. 4.13 that as the concentration of N increases in each system, R_H tends to increase. Same is true for Seebeck coefficient, but beyond the solid solution composition the curve apparently saturates. This behavior, combined with the positive Seebeck and Hall coefficients for the solid solution compositions and the weak temperature dependence of the Hall coefficient provides indirect evidence that

holes are the majority carriers in this case and a single band model is sufficient to calculate the charge carrier concentration and corresponding mobility values.

4.3.2.3 Mobility Calculations

It has been mentioned in section 4.3.2.2 that the behavior of both the X-site substituted solid solutions can be well described by a single band model in which dominant carriers are holes with a concentration $p = 1/e(R_H) \sim 19.5 \times 10^{27}$ m^{-3} for $Ti_3Al(C_{0.5},N_{0.5})_2$ and 9×10^{27} m^{-3} for $Ti_2Al(C_{0.5},N_{0.5})$; the corresponding mobilities being $\mu_p \sim 0.0004$ and 0.0014 $m^2/V\text{-}s$, respectively. The mobilities of the electronic carriers in the solid solutions, as expected, are lower than that of the end members (Fig. 4.14) which is in good agreement with the fact that the α's for the solid solutions are also lower than those of either end members (Fig. 4.11).

Table 4.2 summarizes the transport parameters for X-site substituted solid solutions. Also included are the corresponding values for Ti_3AlC_2, Ti_4AlN_3 [78], Ti_2AlC [79], TiC_x [8] and Ti [8].

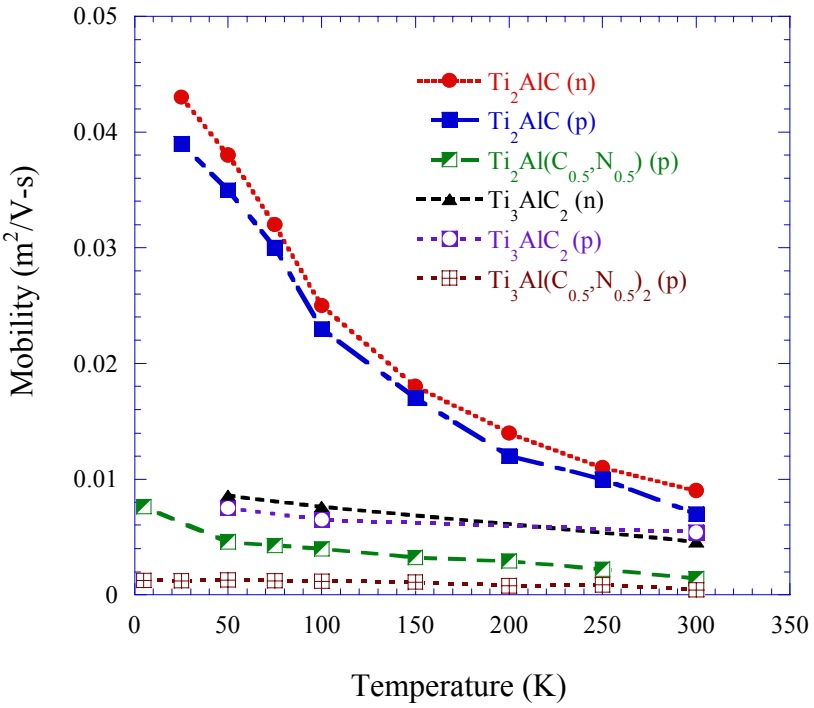

Figure 4.14: Temperature dependence of hole (denoted as p) mobilities for the X-site substituted solid solutions. Electron (denoted as n) and hole mobilties of Ti_3AlC_2 [78] and Ti_2AlC [79] are also shown for the sake of comparison.

Table 4.2 Summary of electrical transport parameters as calculated from the room temperature resistivity, R_H and α results for the X-site substituted solid solutions. Also included are corresponding values of the end members, Ti_4AlN_3, Ti and TiC_x for comparison purposes.

Sample	R_H ($\times 10^{11}$) m^3/C	α (T^{-2}) (m^4/V^2s^2)	μ_n (m^2/V-s)	μ_p (m^2/V-s)	n ($10^{27}/m^3$)	p ($10^{27}/m^3$)
Ti_3AlC_2 [78]	-1.2	4×10^{-5}	0.0046	0.0054	1.6	4.0
$Ti_3Al(C_{0.5},N_{0.5})_2$ [This Work]	32	4×10^{-6}	-	.00045	-	19.5
Ti_2AlC [79]	-20	4.5×10^{-5}	.009	.007	1.0	1.0
$Ti_2Al(C_{0.5},N_{0.5})$ [This Work]	60	2.4×10^{-5}	-	.00141	-	9.0
Ti_4AlN_3 [78]	90	3×10^{-7}	-	.00034	-	7.0
TiC_x [8]	-150 to -261	-	.0012	-	0.24-0.4	-
Ti [8]	-4.5	.0045	.004	-	1.5	-

4.3.2.4 Thermal Conductivity

Figure 4.15 plots the thermal conductivities of the X- site substituted solid solutions and their corresponding end members [72, 79]. Unlike substitution on the A-sites, the X-site substitutions increase the thermal conductivities in both the 312 and 211 systems. The effect is more pronounced at room temperature, where the thermal conductivity of $Ti_3Al(C_{0.5},N_{0.5})_2$ and $Ti_2Al(C_{0.5},N_{0.5})$ (~50 W/m-K in each case) exceed the end members (~40 W/m-K). The absence of any maxima in κ in the temperature range of 40-75 K for the end members (with the exception of Ti_2AlN) is due to relatively higher defect density which is in good agreement with the low RRR for both Ti_3AlC_2 and Ti_2AlC.

In a similar approach as discussed in section 4.3.1.3, κ_{ph} for both the 312 and 211systems is plotted in Fig. 4.16. The phonon conductivity of both solid solution

compositions were observed to be higher than those of the end members, which is in contrast to what was obtained for the A-site substituted solid solutions. Given that the defect densities of the solid solutions are higher than those of the end members, the higher values of κ_{ph} are quite surprising and seem to suggest that for the solid solutions stiffness is playing an important role.

A plot of phonon conductivity and corresponding shear moduli as a function of composition for both 312 and 211 systems (Fig. 4.17) goes through a maximum at the solid solution composition in each case, thereby corroborating the hypothesis that the stiffness is influencing phonon conductivity. Previously it has been shown in section 3.3.3.2 that a plot of Vickers hardness (VHN) and corresponding shear moduli vs. composition also goes through a maximum in 312 and 211 systems. Higher values of VHN, shear moduli and phonon conductivities for the solid solution compositions compared to that of the end members indicated that substitution on the X-site lead to solid solution hardening, which is in good agreement with previous work [22].

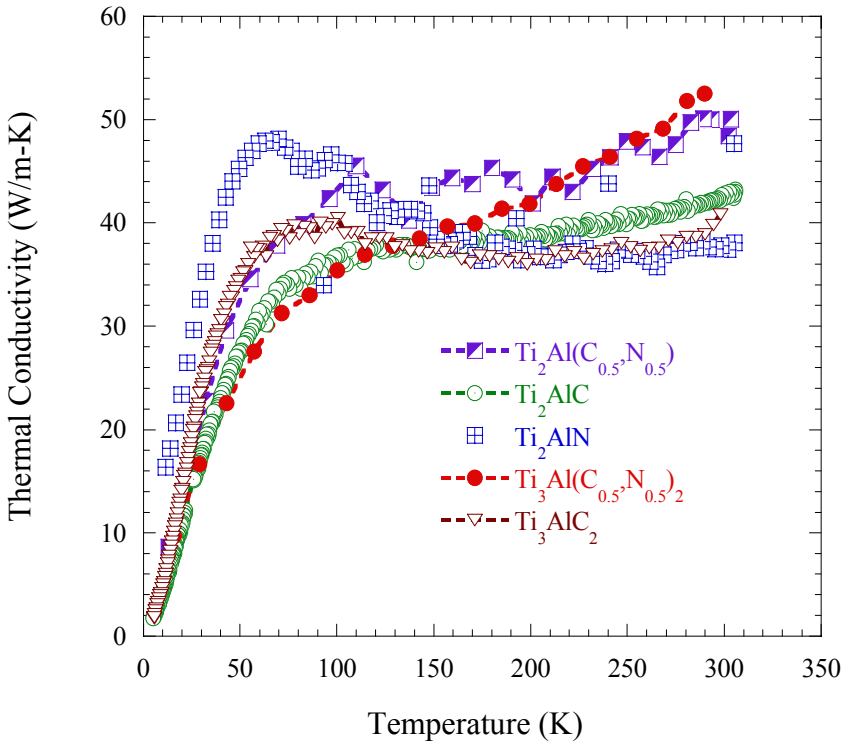

Figure 4.15: Temperature dependence of thermal conductivities of X- site substituted solid solutions compared to those of Ti_3AlC_2 [72], Ti_2AlC [79] and Ti_2AlN [72].

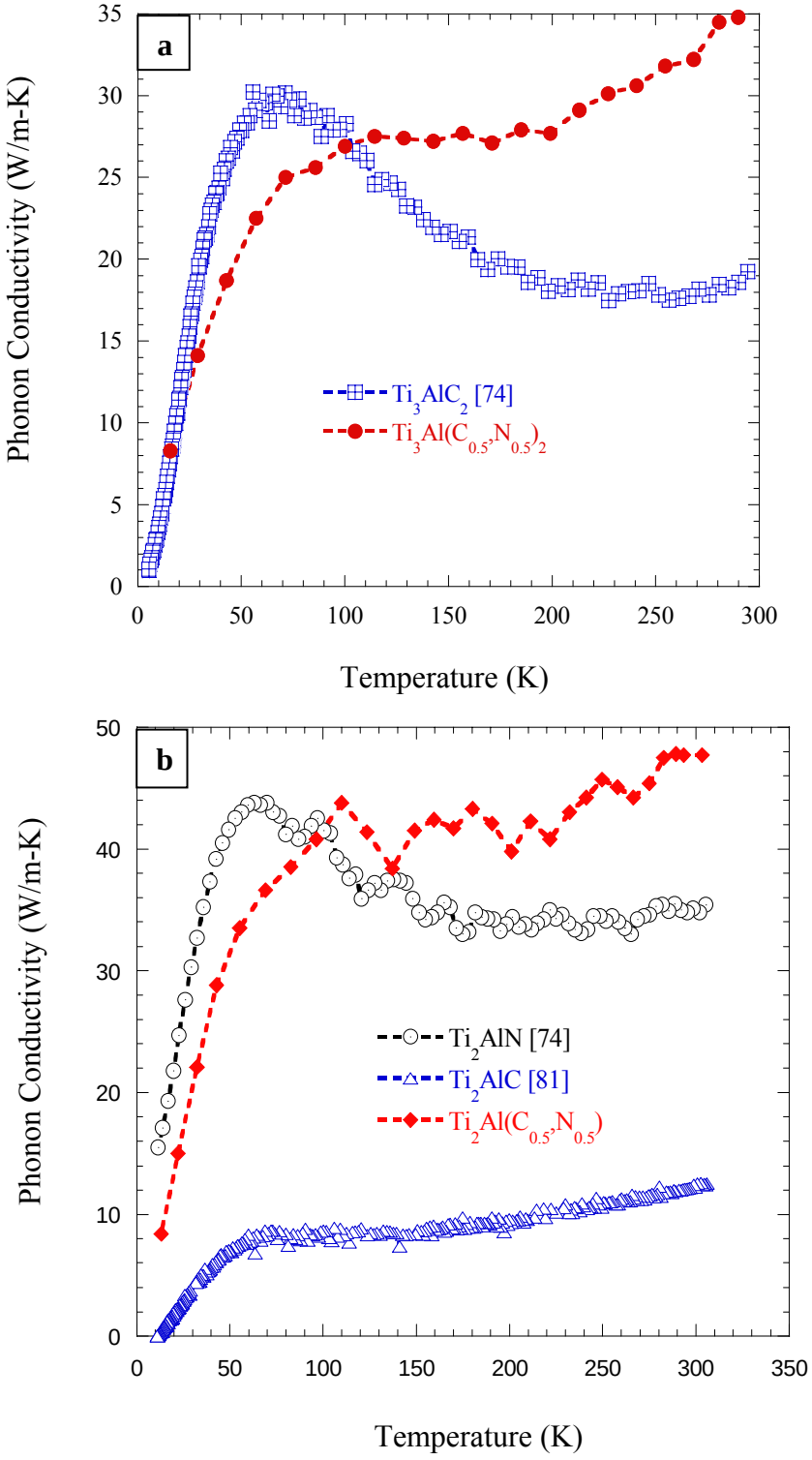

Figure 4.16: Phonon conductivity as a function of temperature for, (a) Ti_3AlC_2 and $Ti_3Al(C_{0.5},N_{0.5})_2$ (312) and, (b) the Ti_2AlC-Ti_2AlN (211) system.

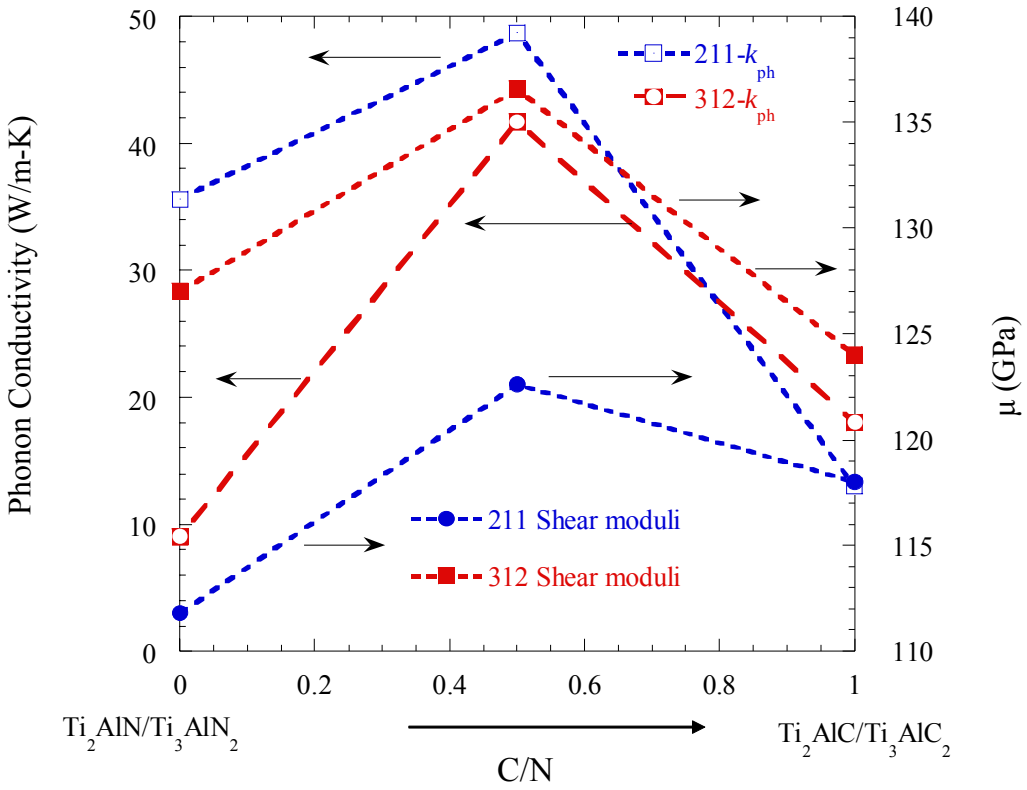

Figure 4.17: Phonon conductivities and shear moduli as a function of composition for the Ti_3AlC_2 and $Ti_3Al(C_{0.5},N_{0.5})_2$ (312) and Ti_2AlC-Ti_2AlN (211) systems.

It is worth mentioning here, that since Ti_3AlN_2 does not exist, values of Ti_4AlN_3 [60, 73] are incorporated in the 312 system for the sake of comparison in Fig. 4.17.

4.4 Conclusions

This section completes the study of the electronic and transport properties of A- or X-site substituted solid solutions. A plot of resistivity as a function of temperature for all the solid solution compositions explored shows metal-like behavior with higher residual resistivities and this lower RRR values than the corresponding end members. This observation indicates that solid solution scattering is operative in both A- and X-site substituted solid solutions.

The Seebeck coefficients for all the compositions explored by substitution on the A site ($Ti_3Si_{0.5}Ge_{0.5}C_2$ and $Ti_3Si_{0.75}Ge_{0.25}C_2$) were negligible in the temperature range of 5-300 K. This observation, combined with the low negative values and weak temperature dependence of R_H, positive quadratic non-saturating magnetoresistance suggest that like the end members $Ti_3Si_{0.5}Ge_{0.5}C_2$ and $Ti_3Si_{0.75}Ge_{0.25}C_2$ are also compensated conductors (n~p) and hence the transport parameters were analyzed in the light of a two band model. The charge carrier density for $Ti_3Si_{0.5}Ge_{0.5}C_2$ were found to be $n \sim p = 2.25 \times 10^{27}$ m^{-3} and the corresponding mobilities were found to be lower than those of the end members.

In contrast substitutions on the X- sites significantly increased the Seebeck and Hall coefficients and yielded positive values in each case. A plot of Seebeck and Hall coefficients as a function of normalized concentration of N reveals that replacing C atoms by N in the system increases the hole carrier concentration which become the dominant charge carriers. The positive values of the Hall and Seebeck coefficients suggests that a single band model can be used for calculating the transport parameters for the X-site substituted solid solutions. The charge carrier density, holes in this case,

were calculated to be 19.5×10^{27} m^{-3} for $Ti_3Al(C_{0.5},N_{0.5})_2$ and 9×10^{27} m^{-3} for $Ti_2Al(C_{0.5},N_{0.5})$; the corresponding mobilities being μ_p~0.0004 and 0.0014 m^2/V-s, respectively, which were lower than that of the corresponding end members.

Reduction of thermal conductivity for A- site substituted solid solutions is in good agreement with the resistivity results and can be related to the solid solution scattering effect. However, the thermal and corresponding phonon conductivities of the X-site substituted solid solutions were observed to be higher than those of their corresponding end members. This implies that substitutions on the X-sites cause less phonon scattering than that on the A-site which is due to the fact that X-site substituted solid solutions are stiffer than the corresponding end members. A plot of phonon conductivity and shear moduli for the 312 and 211 systems goes through a maximum at the solid solution compositions indicating that stiffness indeed plays a role in increasing phonon conductivity for $Ti_3Al(C_{0.5},N_{0.5})_2$ and $Ti_2Al(C_{0.5},N_{0.5})$. However, in order to generalize this statement more solid solution compositions with varying nitrogen contents needs to be explored. This comment, notwithstanding, it is hereby acknowledged that more work is needed to understand fully the influence of stiffness on phonon conductivity in 312 and 211 systems.

5: Room and Elevated Temperature Mechanical Properties

5.1 Introduction

This work is focused on the microhardness, room and elevated temperature behavior of A- or X-site substituted solid solutions under compression. Thermal shock resistance and damage tolerance for the A-site substituted solid solutions is also reported and compared to that of the corresponding end members.

5.2 Experimental Details

Cubes of 3mm ×3mm×3mm were electric discharged machined for the compression tests. Elevated temperature compressive testing was carried out only on FG samples. A servo hydraulic MTS machine (MTS Minneapolis, MN) was used for this test. The only information that is extracted from the compressive load–displacement curves are the maximum stresses. All tests were conducted in air. The nominal strain rate for all experiments was 0.0167 s−1.

To determine the thermal shock resistance and damage tolerance the specimens were electric discharge machined in accordance with ASTM C1161 Type A [84] specifications (1.5mm×2mm×25 mm). Susceptibility to thermal shock was evaluated by quenching the specimens from successively higher temperatures in water. Typically, three samples were inserted in a box furnace at the testing temperature, held at that temperature for ~10 min. to equilibrate thermally with the furnace and immediately quenched in an ambient temperature water bath. The quenched samples were then tested according to ASTM-C1161 [84].

Damage tolerance was measured by first Vickers indenting the tensile surface of 4-point bend specimens, using loads of 100, 200, and 300 N. At least three samples were tested after each indentation, again according to ASTM-C1161.

The microhardness was measured (LECO-M400, LECO Corp, St. Joseph, MI) at 1, 5, and 10 N. The hardness was calculated by averaging at least 10 measurements at each load.

5.3 Results and Discussion

5.3.1 Ti_3GeC_2 and A-Site Substituted Solid Solutions

5.3.1.1 Vickers Microhardness

Similar to all other MAX phases [4,11,22, 85], the Vickers microhardness values initially decrease with increasing applied load, but then asymptote at higher loads (Fig. 5.1). The asymptotic value for $Ti_3Si_{0.5}Ge_{0.5}C_2$ and $Ti_3Si_{0.75}Ge_{0.25}C_2$ (≈2.5±0.2GPa) are statistically indistinguishable, while that of $Ti_3Si_{0.5}Al_{0.5}C_2$ is ~2.9±0.5 GPa. More important, since at comparable grain sizes, the hardness values of all the solid solution compositions explored fall in between Ti_3SiC_2 (~3 ± 0.25 GPa) and Ti_3GeC_2 (~2.2 ± 0.5GPa) we conclude that no solid solution hardening effect is operative in this system.

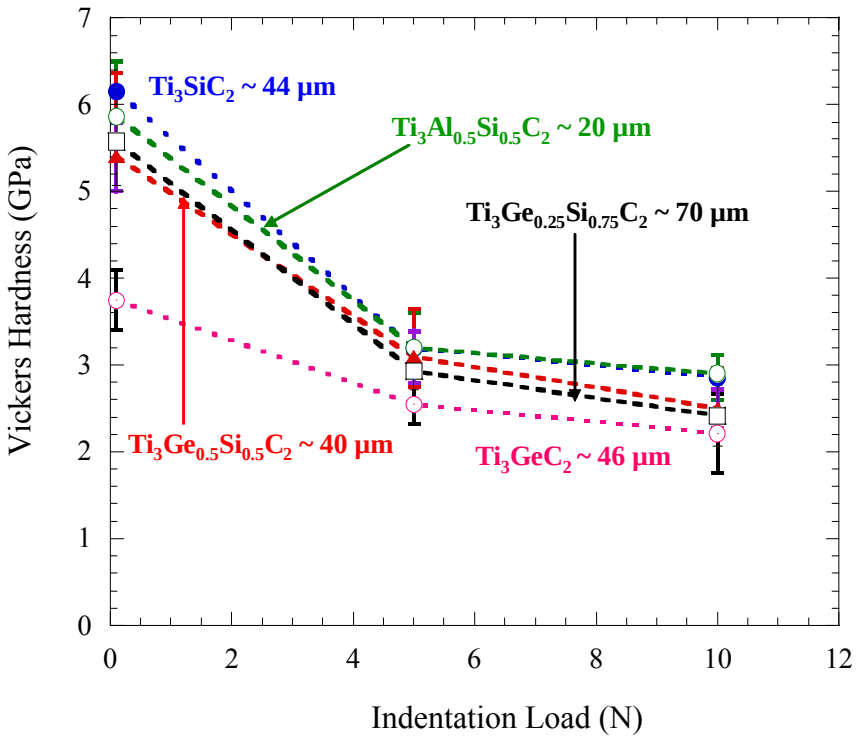

Figure 5.1: Vickers hardness versus indentation load for CG Ti_3GeC_2, $Ti_3Si_{0.5}Ge_{0.5}C_2$, $Ti_3Si_{0.75}Ge_{0.25}C_2$ and $Ti_3Si_{0.5}Al_{0.5}C_2$. Also included are data for Ti_3SiC_2 obtained in this work.

Figure 5.2 a–c show typical SEM micrographs of Vickers indentation marks formed under a load of 10N in Ti_3GeC_2, $Ti_3Si_{0.5}Ge_{0.5}C_2$ and Ti_3SiC_2, respectively. For reasons that are not clear the value of Vickers hardness obtained for Ti_3GeC_2 (~2.2 ± 0.5GPa) is significantly lower compared to earlier work [14, 15]. The lower value, however, has to be considered more accurate, since it probably reflects a purer matrix. In previous work [15], the loss of Ge led to the presence of ≈5 vol. % TiC in the final matrix. The soaking at 900 ºC during processing used here probably reduced this loss

and enhanced the purity. The 6 h soak at 1600 ºC followed by the 48 h anneal in Ar may also have played a role. It is worth noting that this hardness value is one of the lowest reported for a MAX phase to date [27].

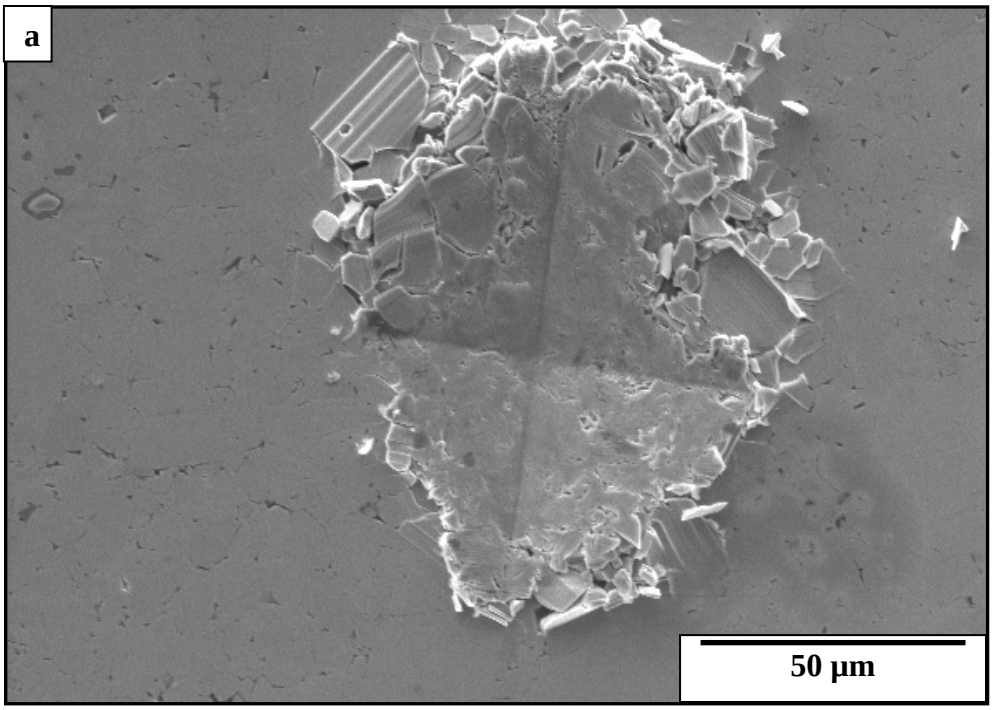

Figure 5.2: Secondary SEM micrographs of Vickers indentation using a 10 N load on (a) Ti_3GeC_2; (b) $Ti_3Si_{0.5}Ge_{0.5}C_2$; and (c) Ti_3SiC_2 [27].

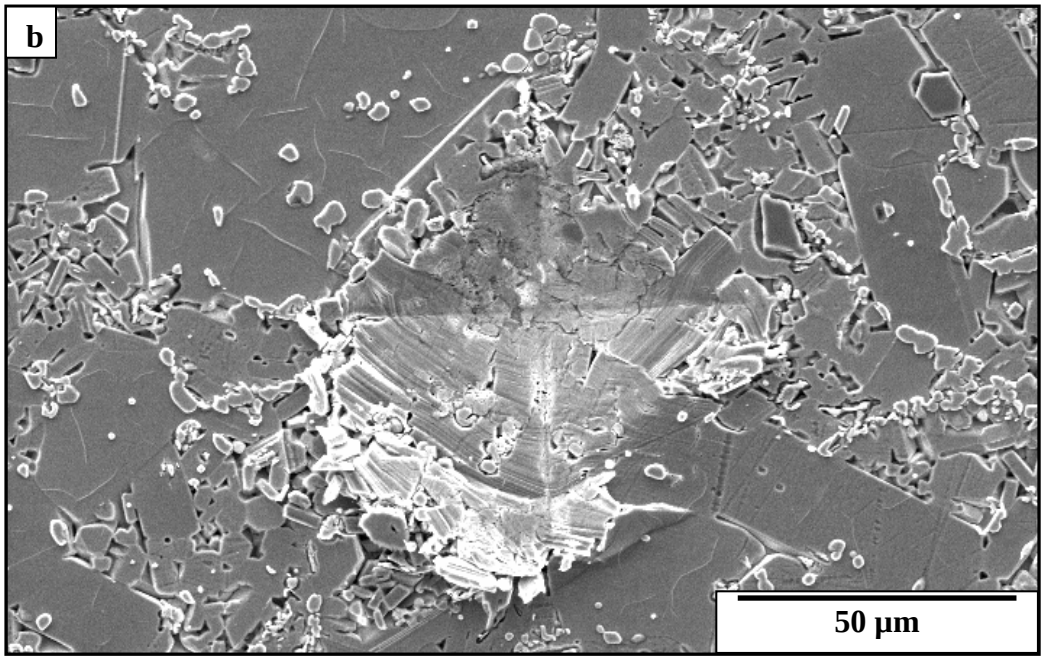

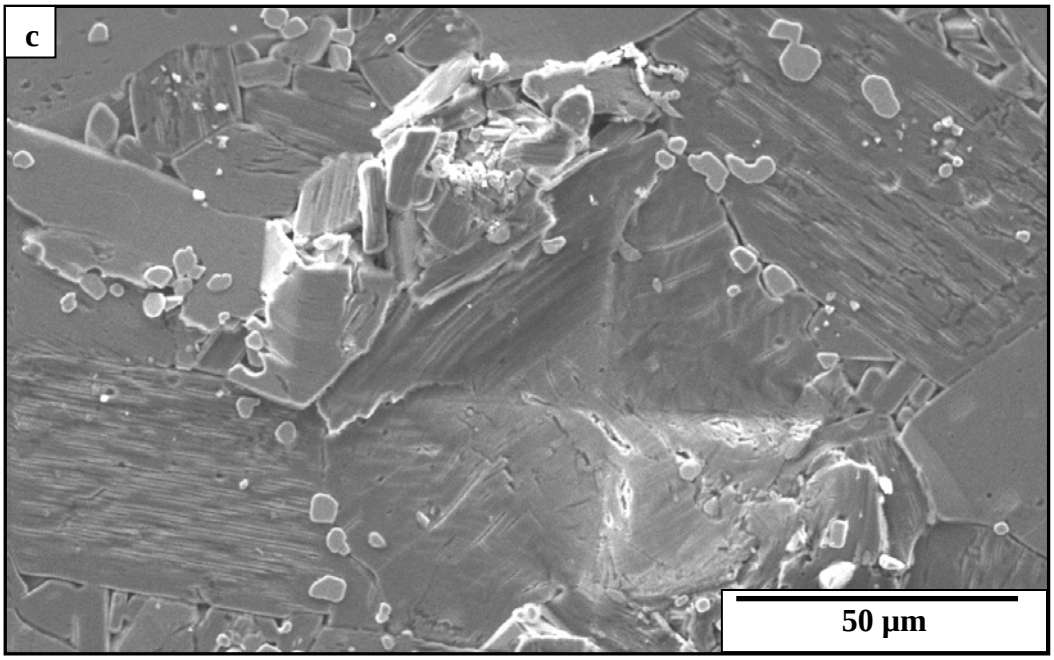

Figure 5.2 (*continued*)

Like all other MAX phases [4, 7, 22, 85, 86], no dominant cracks are observed to emanate from the corners of the Vickers indentations, even at the highest load tested (300 N). The area around the indentation piles up (Fig. 5.2) instead of sinking in, and local energy absorbing mechanisms previously described [86]—like grain buckling, kinks and delaminations (Fig. 5.2)—are all readily observed.

5.3.1.2 Damage Tolerance and Thermal Shock

The damage tolerance and thermal shock behavior of $Ti_3Si_{0.5}Ge_{0.5}C_2$ and Ti_3GeC_2 are shown in Figs. 5.3 and 5.4, respectively.

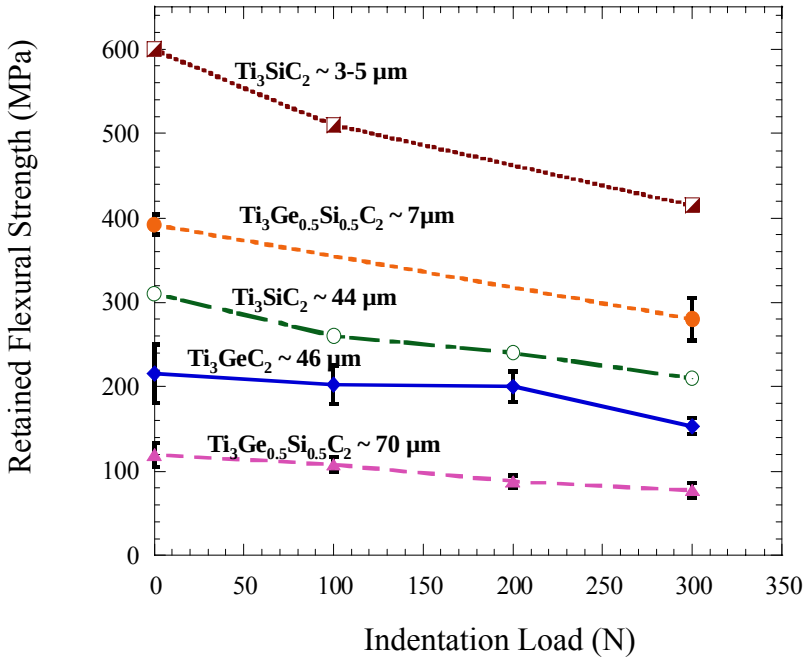

Figure 5.3: Effect of indentation load on post-indentation four point flexural strength of CG Ti_3GeC_2 samples and FG and CG $Ti_3Si_{0.5}Ge_{0.5}C_2$ samples. Each point is the average of at least three separate tests. Also included are results for Ti_3SiC_2 [7].

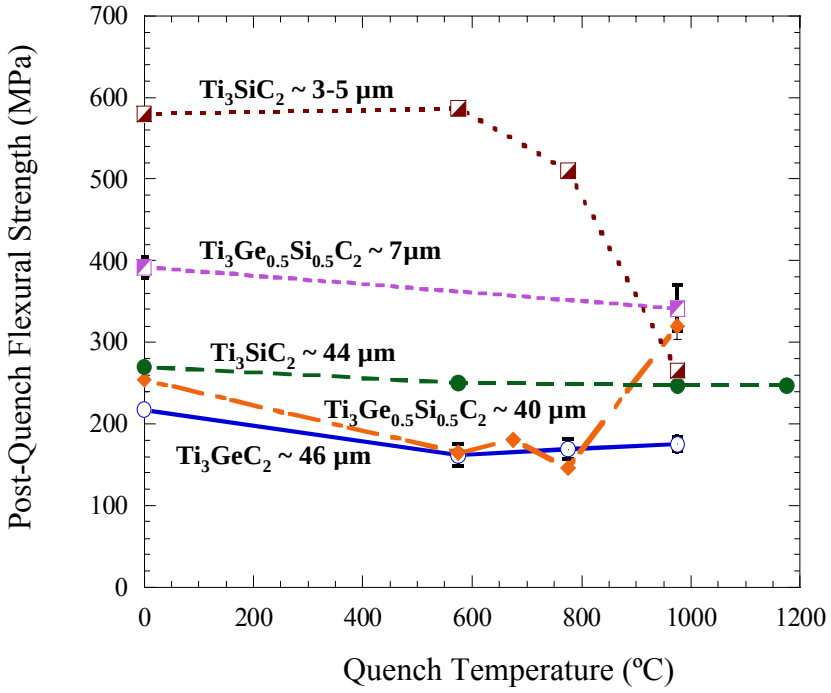

Figure 5.4: Post-quench four- point flexural strength versus quench temperature of CG Ti_3GeC_2 samples and FG and CG $Ti_3Si_{0.5}Ge_{0.5}C_2$ samples. The quench was into ambient temperature water. Each point is the average of at least three separate tests. Also included are results for Ti_3SiC_2 [7].

From Fig. 5.3 and 5.4 it is obvious that:

(i) At comparable grain sizes (~3–5 µm for Ti_3SiC_2 versus 7±3 µm for $Ti_3Si_{0.5}Ge_{0.5}C_2$) the flexural strengths of Ti_3SiC_2 (~600MPa) are higher than the solid solution $Ti_3Si_{0.5}Ge_{0.5}C_2$ (~ 400±12MPa). This is consistent with the fact that no solid solution strengthening is occurring in this system.

(ii) Compared to more brittle ceramics—the strengths of which are quite sensitive to indentation loads—the phases tested here are significantly more damage tolerant (Fig. 5.3). However, consistent with the ceramic literature, the larger-grained, and consequently weaker samples, are more damage tolerant than their fine-grained counterparts (Fig. 5.3).

(iii) The response of $Ti_3Si_{0.5}Ge_{0.5}C_2$ and Ti_3GeC_2 to thermal shock (Fig. 5.4) is characteristic of, and unique to, the MAX phases in that it is neither that of typical ceramics nor metals, but intermediate between them. With the exception of the CG $Ti_3Si_{0.5}Ge_{0.5}C_2$ samples, quenching results in a gradual decrease in post-quench strengths up to about 600 ºC, beyond which it asymptotes. Surprisingly the post-quench flexural strengths of the CG $Ti_3Si_{0.5}Ge_{0.5}C_2$ samples were ≈25% *higher* than the as-processed samples. And while this quench-hardening tendency has been observed before for Ti_3AlC_2 [11], Ti_3SiC_2 [7], and Ti_4AlN_3 [60], in none of these compounds did the post-quench flexural strength *exceed* the original strength. As far as we are aware, such quench hardening has never been observed in any other ceramic material to date. The exact reason for this state of affairs is unclear, but is most probably due to the formation of kink bands induced by the thermal stresses. In that respect, it is not unlike how deformations at high temperatures result in hardening and stiffening of CG Ti_3SiC_2 samples at room temperatures [87].

To verify this result, some samples were quenched twice from 1000 ºC. The multiple quenched samples were indeed found to be stronger than the single quenched samples by ~ 9%.

(iv) The flexural strengths of the as-fabricated FG solid solution samples (392 ± 12 MPa) are about 35% higher than their CG counterparts (252 ± 15MPa). The origin of this strengthening can be two-fold: a scaling of the flaw size with grain size, or a Hall-Petch effect. In both cases the strength would be expected to scale as $1/\sqrt{d_m}$, where d_m is the average grain size. Given, the extraordinary damage tolerance of these solids, especially the CG solid solution samples, it is unlikely that the former is operative. In other words, since the size of the indentations introduced in the samples to explore their damage tolerance (Fig. 5.3) is much larger than d_m, it is unlikely that the presence of intrinsic flaws, whose size is of the order of the largest grains, could be responsible for the differences in strengths observed. We conclude the strengthening must be of the Hall-Petch type, which is not too surprising given the central role dislocation pileups play in the deformation of the MAX phases [35]. The same conclusion was reached when analyzing the flexural strengths of $(Ti, Nb)_2AlC$ solid solution samples [85].

5.3.1.3 Room and Elevated Temperature Compression Behavior

The temperature dependence on the compressive stress–displacement curves for the FG $Ti_3Si_{0.5}Ge_{0.5}C_2$ and $Ti_3Si_{0.5}Al_{0.5}C_2$ samples are shown in Fig. 5.5 (a, b). Also included in Fig. 5.5 (a) are previous results for FG Ti_3GeC_2 samples [15].

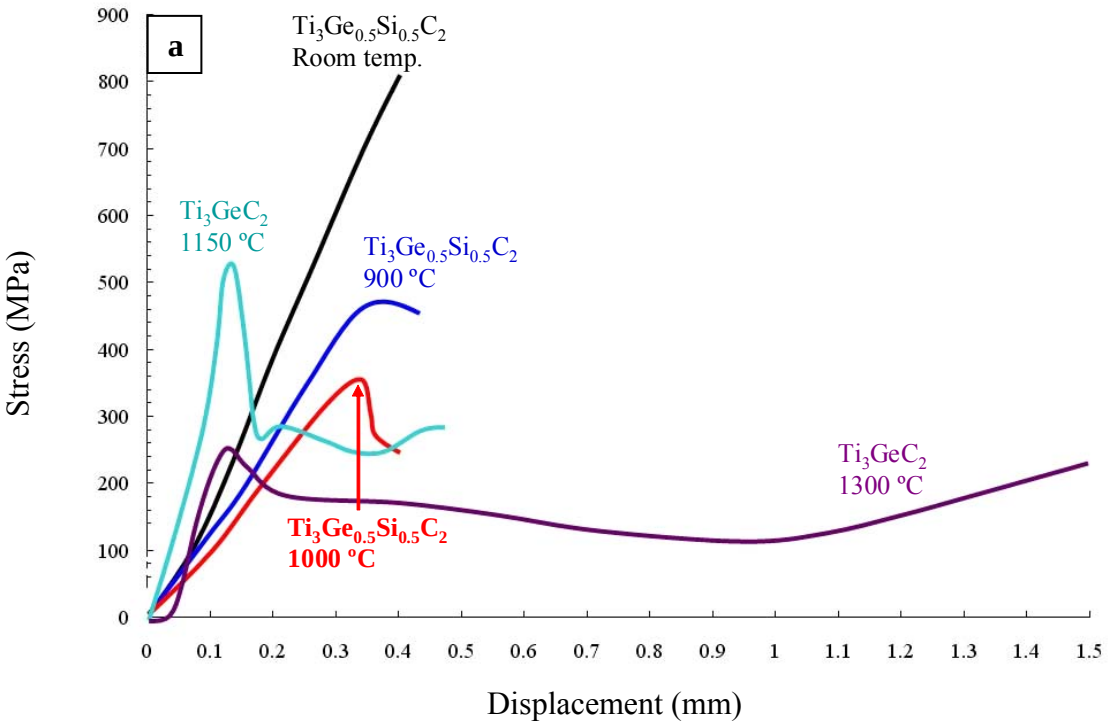

Figure 5.5: Temperature dependence of compressive stress-displacement curves for (a) FG $Ti_3Si_{0.5}Ge_{0.5}C_2$ and (b) $Ti_3Si_{0.5}Al_{0.5}C_2$. Also reproduced are results of FG Ti_3GeC_2 tested previously [15].

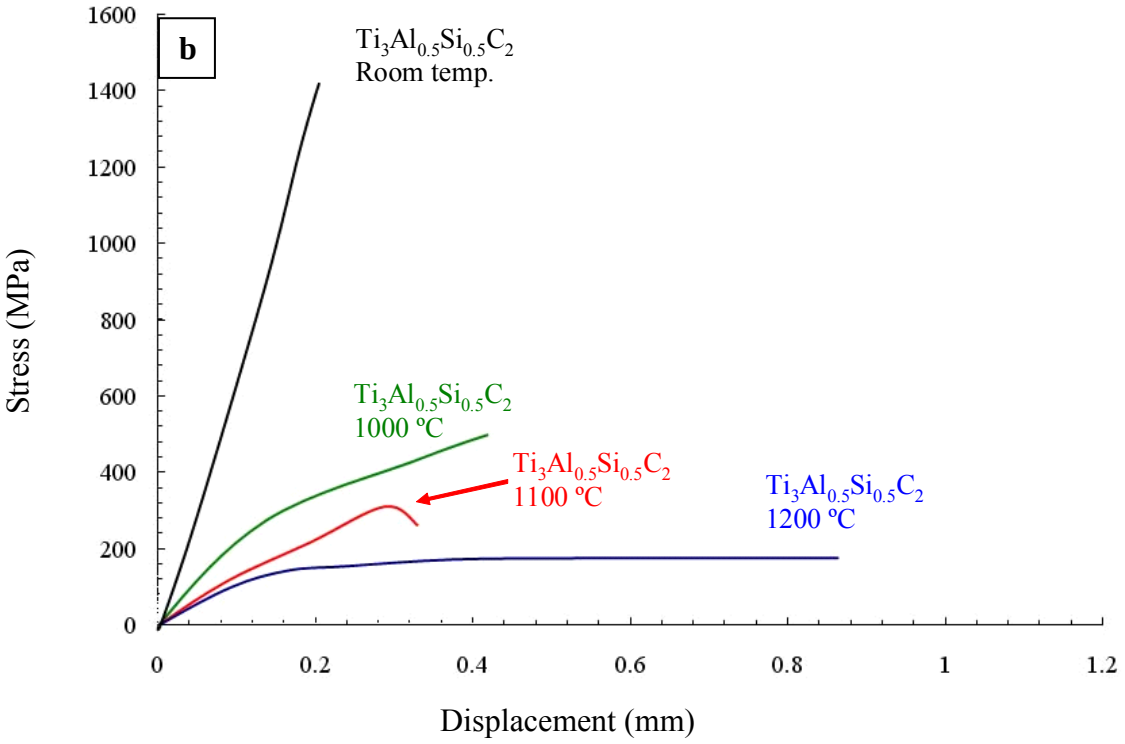

Figure 5.5 (*continued*)

Similar to all MAX phases tested to date [7, 11, 14, 15, 22, 60, 85, 87–89], the samples tested here go through a brittle to ductile transition at temperatures >1000 ºC. As shown in Fig. 5.6 the compressive strengths of the $Ti_3Si_{0.5}Ge_{0.5}C_2$ samples decrease from room temperature to ≈900 ºC at one rate, after which the softening is noticeably accelerated (Fig. 5.6). $Ti_3Si_{0.5}Al_{0.5}C_2$ behaves very similarly beyond ≈1000 ºC. By comparison to the Ti_3GeC_2 [15] and Ti_3AlC_2 [11] results (Fig. 5.6), it is fair to conclude that the brittle-to-ductile transition for $Ti_3Si_{0.5}Ge_{0.5}C_2$ is in the vicinity of 1050 ºC and that of $Ti_3Si_{0.5}Al_{0.5}C_2$ is around 1150 ºC. This comment notwithstanding,

it is hereby acknowledged that more high temperature testing is required to better understand the effect of composition on the high temperature mechanical properties.

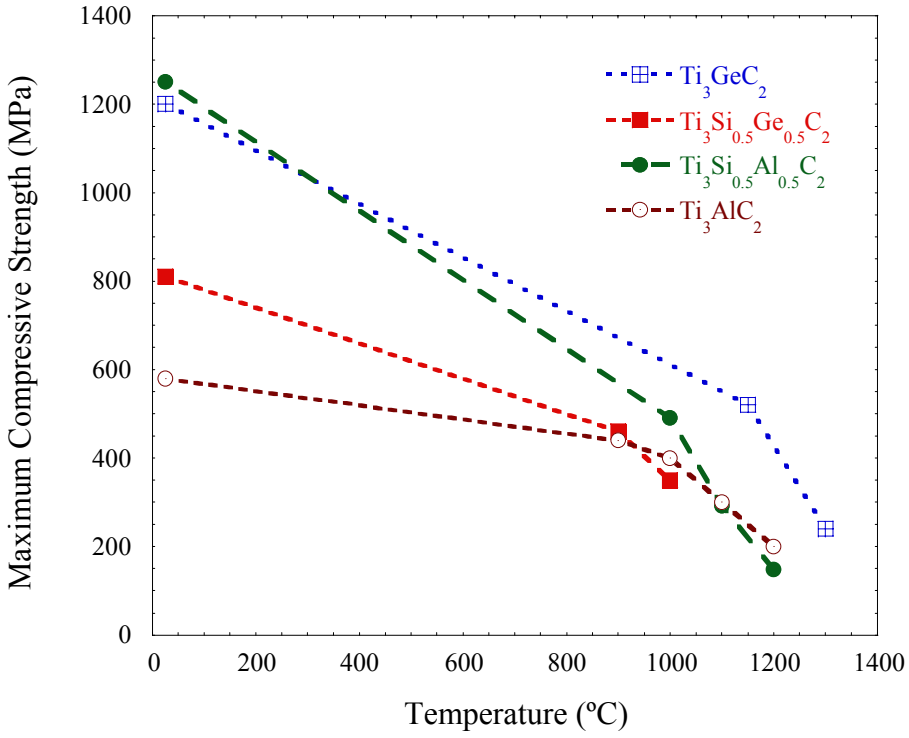

Figure 5.6: Ultimate compressive strength vs. temperature for A- site substituted solid solutions. Also plotted are corresponding values of Ti_3GeC_2 [15] and Ti_3AlC_2 [11].

The room temperature compressive strength in the Ti_3SiC_2-Ti_3GeC_2 system shows a monotonic decrease with increasing Ge content (Fig. 5.7).

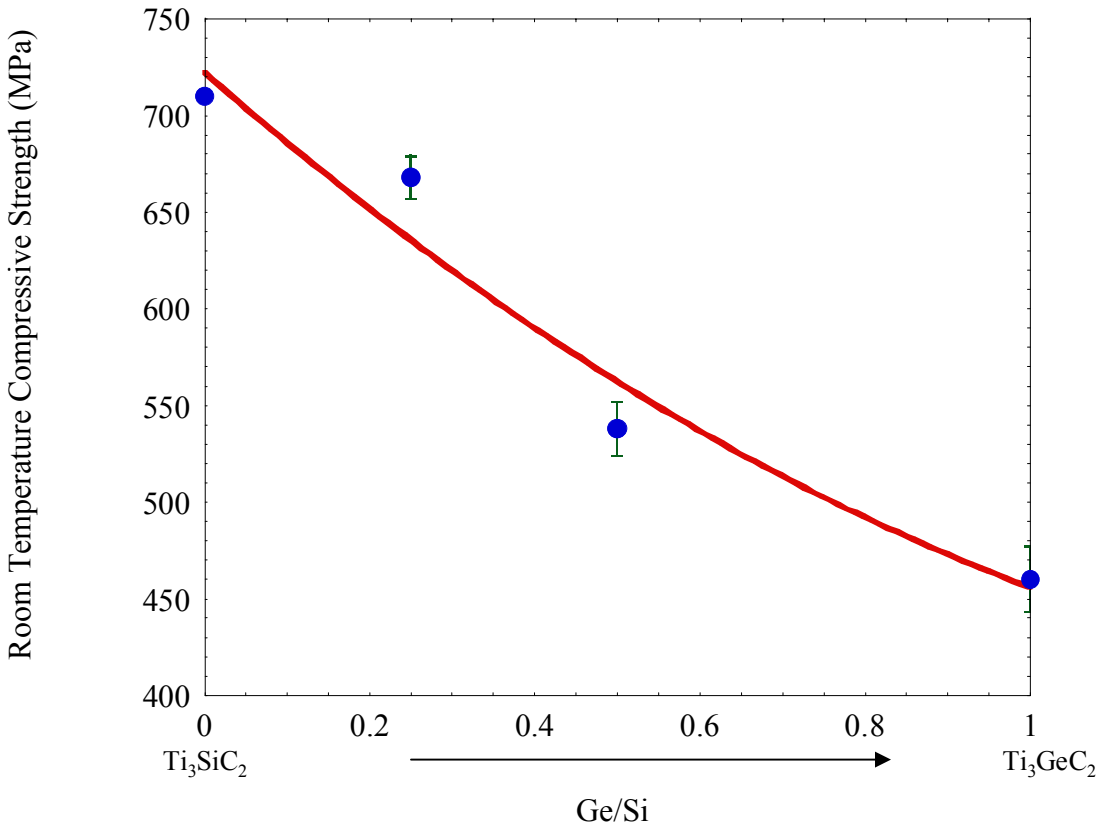

Figure 5.7: Effect of Ge content on room temperature compressive strengths in Ti_3SiC_2-Ti_3GeC_2 system.

It is important to note that, unlike say the yield points of metals, there is nothing intrinsic about the strengths of the MAX phases; the latter are quite dependent on microstructure, in general, and grain size in particular. This is especially true when it is appreciated that the strengths can be significantly reduced if only a few large grains are present. In other words, the strengths are not necessarily related to the average grain size, but to the largest grains. These comments notwithstanding, the trend seen in Fig.5.7 must be intrinsic for the simple reason that the strengths of the $Ti_3Si_{0.75}Ge_{0.25}C_2$ samples were higher than those of $Ti_3Si_{0.5}Ge_{0.5}C_2$, despite the fact that the average grain size of the former is almost double the latter. Note that this trend is also consistent with the hardness results (Fig. 5.2) in that Ti_3GeC_2 is the softest phase. Interestingly and in contradiction to the results shown in Fig. 5.7, the room temperature compressive strength of the FG $Ti_3Si_{0.5}Ge_{0.5}C_2$ samples (~810MPa) is lower than previous FG Ti_3GeC_2 samples (~1200MPa) [15]. The reasons for this state of affairs are not clear at this point, but are most probably related to the same arguments made above, namely phase purity, annealing and as important differences in microstructure. Here again, more work is needed to sort out some of the outstanding issues. Finally it is worth noting that the high strengths of the FG Ti_3GeC_2 samples reported previously [15] are consistent with their higher hardness. The room temperature compressive strength of FG $Ti_3Si_{0.5}Al_{0.5}C_2$ (1.25 GPa) was found to be very similar to that of FG Ti_3SiC_2 [1.2 GPa]. Given, that the hardness values of the two compounds are indistinguishable, this observation, however, is not surprising.

5.3.2 X -Site Substituted Solid Solutions

5.3.2.1 Vickers Microhardness

Figure 5.8 plots the Vickers hardness as a function of indentation load for $Ti_3Al(C_{0.5},N_{0.5})_2$ and $Ti_2Al(C_{0.5},N_{0.5})$. Also plotted are corresponding values of the end members Ti_3AlC_2 [11] and Ti_2AlC, Ti_2AlN obtained in this work. Here again, the Vickers microhardness values initially decrease with increasing applied load, but then asymptote at higher loads.

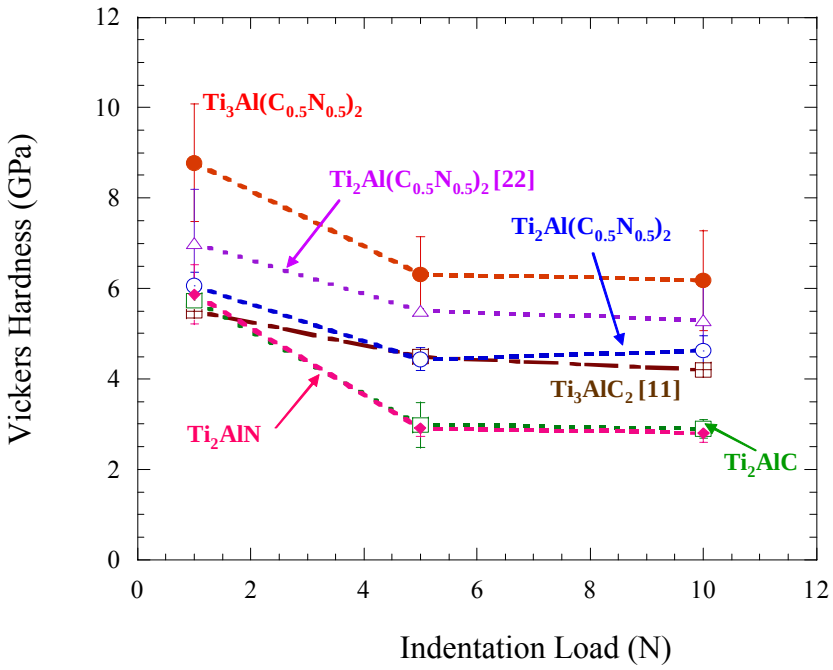

Figure 5.8: Vickers hardness versus indentation load for MG $Ti_3Al(C_{0.5},N_{0.5})_2$, $Ti_2Al(C_{0.5},N_{0.5})$. Also included are values of Ti_2AlC, Ti_2AlN obtained in this work and that of $Ti_2Al(C_{0.5},N_{0.5})$ [22] and Ti_3AlC_2 [11].

At comparable grain size the asymptotic value for $Ti_3Al(C_{0.5},N_{0.5})_2$ (6.2±1 GPa) and $Ti_2Al(C_{0.5},N_{0.5})$ (4.6±0.5 GPa) were found to be higher than the corresponding end members Ti_3AlC_2 (4.2±0.2 GPa) and Ti_2AlC (2.9±0.5 GPa), Ti_2AlN (2.8±0.2 GPa), which clearly indicates solid solution hardening. This is in good agreement with previous work [22] and with the higher shear moduli (3.3.3.2) and phonon conductivities (4.3.2.3) obtained for the X-site substituted solid solutions. It is to be noted here that the Vickers hardness of the solid solution $Ti_2Al(C_{0.5},N_{0.5})$ in this work is lower (Fig. 5.8) than that obtained previously [22]. The higher value in the latter case is most probably due to less clean matrix and the lower value reported in this work has to be considered more accurate as it probably represents a purer matrix.

5.3.2.2 Room and Elevated Temperature Compression Behavior

Figure 5.9 shows the high temperature behavior of MG X-site substituted solid solutions under compression.

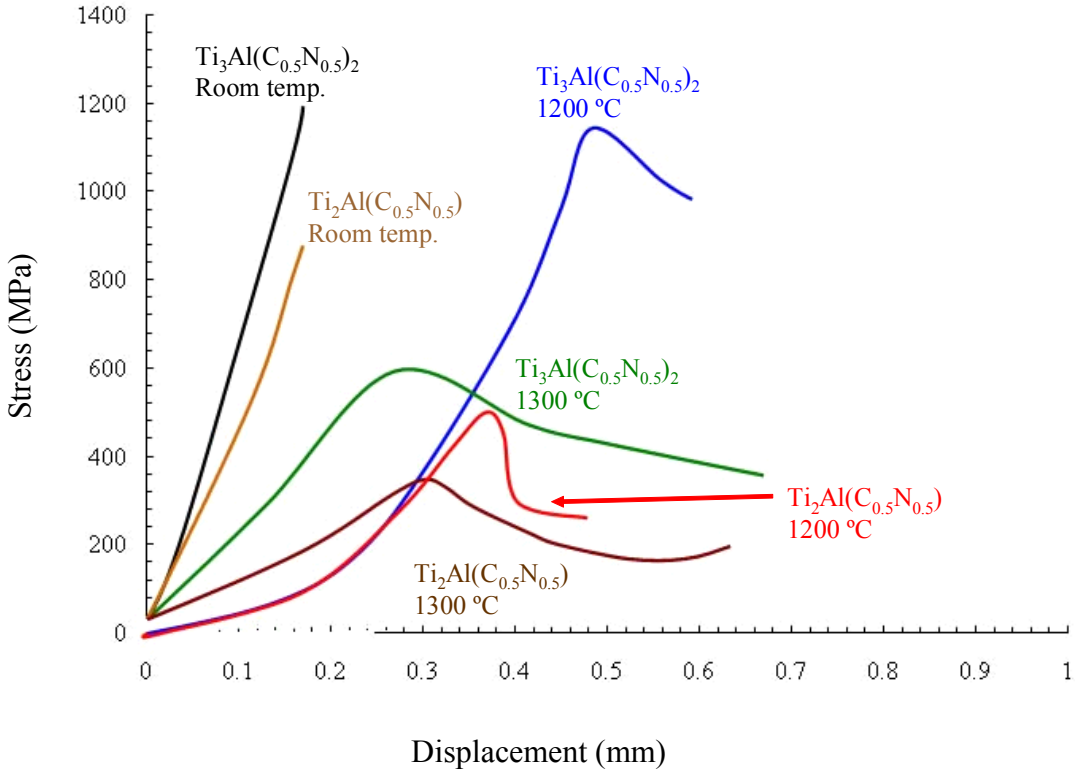

Figure 5.9: Temperature dependence of compressive stress-displacement curves for MG $Ti_3Al(C_{0.5},N_{0.5})_2$ and $Ti_2Al(C_{0.5},N_{0.5})$.

Like all other MAX phases, the solid solution compositions behave plastically at higher temperatures. However $Ti_3Al(C_{0.5},N_{0.5})_2$ (312) was stronger at higher temperatures than that of $Ti_2Al(C_{0.5},N_{0.5})$ (211). This indicates that in the family of isostructural MAX phases, a 312 solid solution composition with a higher number of M-X layers separating the A layers and thereby having a higher molar percentage of Nitrogen in the system tends to retain more strength at higher temperatures than a 211 solid solution composition, where the number of M-X layers separating the A layer and the corresponding molar percentage of Nitrogen is lower than that of 312. It is also worth mentioning that unlike most of the MAX phases reported to date, the solid solution composition $Ti_3Al(C_{0.5},N_{0.5})_2$ holds the room temperature strength up to almost 1200 ºC. However, beyond 1200 ºC, softening is noticeably accelerated. By comparison to the Ti_3AlC_2 [11] and Ti_2AlC, Ti_2AlN [22] results (Fig. 5.10), it is fair to conclude that the brittle-to-ductile transition for $Ti_3Al(C_{0.5},N_{0.5})_2$ is in the vicinity of 1250 ºC and that of $Ti_2Al(C_{0.5},N_{0.5})$ is around 1150 ºC.

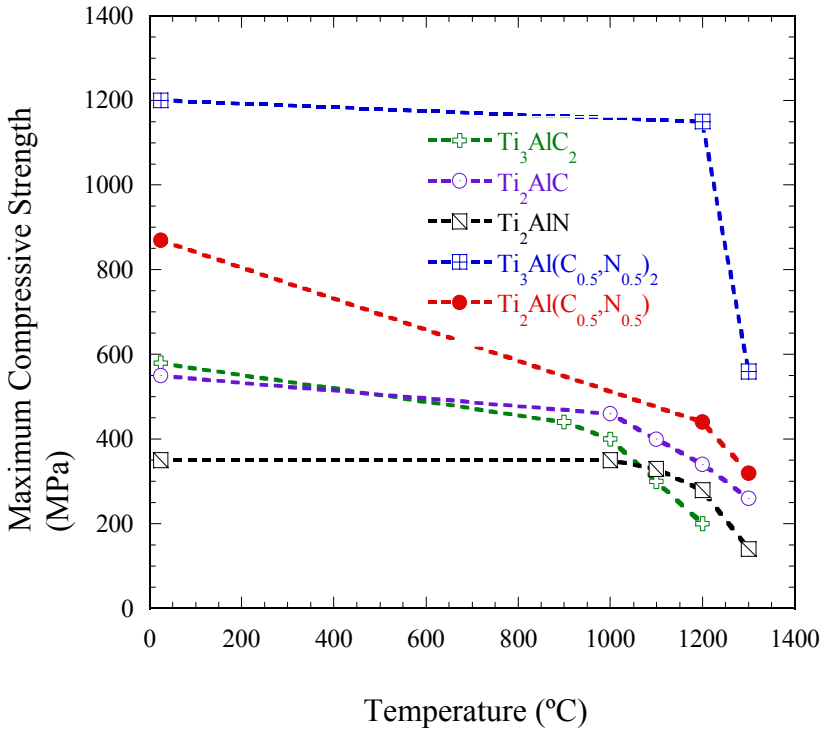

Figure 5.10: Ultimate compressive strength vs. temperature for X-site substituted solid solutions. Also plotted are corresponding values of Ti_3AlC_2 [11] and Ti_2AlC, Ti_2AlN [22].

The room temperature compressive strengths plotted as a function of composition clearly go through a maximum at the solid solution compositions in 312 and 211 systems, respectively (Fig. 5.11). The higher values of the room temperature compressive strengths of the solid solution are consistent with the higher hardness values. It is to be noted that since Ti_3AlN_2 does not exist, room temperature compressive strength of medium grained Ti_4AlN_3 [60] is plotted for the 312 system just to complete the comparison. Given, the structural similarity, it is reasonable to

assume that the room temperature compressive strength of Ti_3AlN_2, if existed, would have been very similar to that of Ti_2AlN and Ti_4AlN_3.

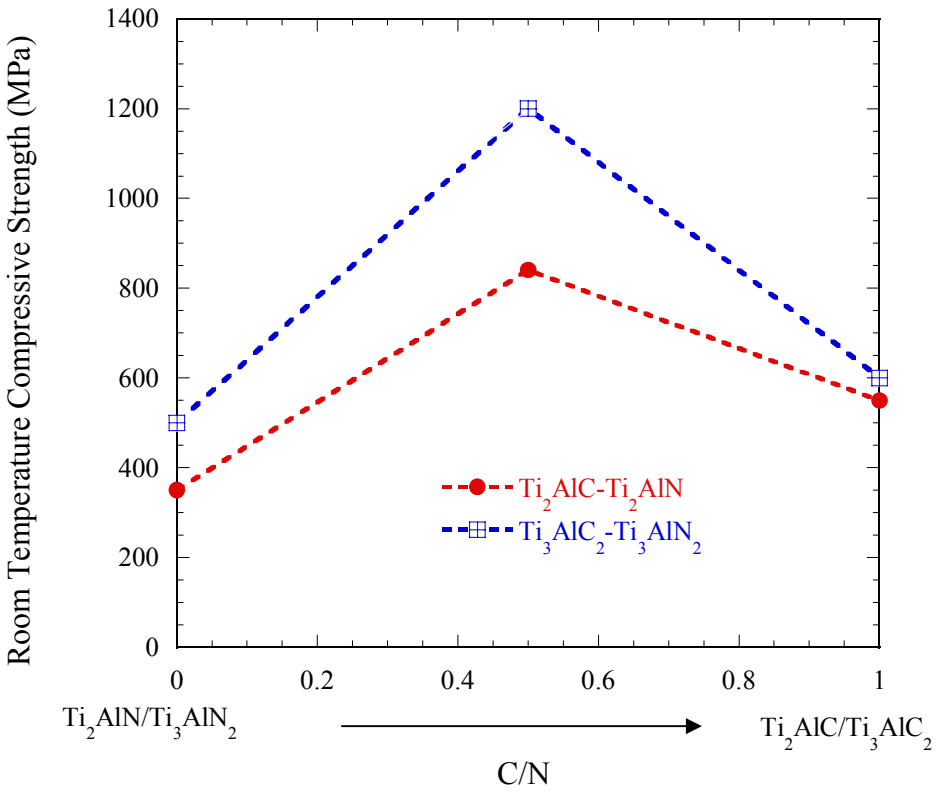

Figure 5.11: Room temperature compressive strength for X-site substituted solid solutions (medium grained) compared to that of the corresponding end members; Ti_3AlC_2 (medium grained) [11] and Ti_2AlC, Ti_2AlN (coarse grained) [22], and, Ti_4AlN_3 [60].

Since at comparable grain size, the solid solutions are stronger than the corresponding end members, it is reasonable to consider the strength in this case to be microstructure dependent rather than being intrinsic.

5.4 Conclusions

This chapter reports on the room and elevated temperature mechanical behavior of A- or X-site substituted solid solutions with emphasis on the Vickers microhardness, thermal shock resistance, damage tolerance and compressive strengths.

The hardness of $Ti_3Si_{0.5}Ge_{0.5}C_2$, $Ti_3Si_{0.75}Ge_{0.25}C_2$ (≈2.5±0.2 GPa) and that of $Ti_3Si_{0.5}Al_{0.5}C_2$ (~2.9±0.5 GPa) falls in between Ti_3SiC_2 (~3 ± 0.25 GPa) and Ti_3GeC_2 (~2.2 ± 0.5 GPa) indicating that solid solution strengthening is not operative in case of A site substitution. All the compositions explored in Ti_3SiC_2-Ti_3GeC_2 system were quite damage tolerant and thermal shock resistant. A 300N Vickers indentation in a 1.5mm thick, four-point bend bar decreases its strengths by anywhere from 25 to 35%. Quenching in water from 1000 ºC reduces the four-point flexural strength by 10 to 20%; i.e., it is not catastrophic. Notably, the post-quench flexural strength of the coarse-grained $Ti_3Si_{0.5}Ge_{0.5}C_2$ samples was ≈25% *higher* than the as-received bars. Increasing the Ge content in the Ti_3SiC_2-Ti_3GeC_2 system resulted in a decrease in the compressive strengths. This observation is in good agreement with the hardness results. The ultimate compressive strengths of fine-grained $Ti_3Si_{0.5}Ge_{0.5}C_2$ samples, decreased monotonically from room temperature to ≈950 ºC. And while failure was brittle at room temperature, above 1000 ºC the loss in strength was more severe, but

the deformation was more plastic. Similar behavior was observed for $Ti_3Si_{0.5}Al_{0.5}C_2$ around 1150 ºC.

Unlike the A-site, substitutions on the X-sites increased the hardness of the solid solutions considerably compared to that of the end members. The hardness values of $Ti_3Al(C_{0.5},N_{0.5})_2$ (6.2±1 GPa) and $Ti_2Al(C_{0.5},N_{0.5})$ (4.6±0.5 GPa) were found to be higher than the corresponding end members Ti_3AlC_2 (4.2±0.2 GPa) and Ti_2AlC (2.9±0.5 GPa), Ti_2AlN (2.8±0.2 GPa), which indicates solid solution hardening. The room temperature compressive strengths go through a maximum at the 50-50 compositions in both 312 and 211 system, which is consistent with the hardness results. Like all other MAX phases, softening was observed for the solid solution compositions at higher temperatures and the strength retained by the solid solutions were higher than the corresponding end members. Brittle to ductile transition was observed for $Ti_3Al(C_{0.5},N_{0.5})_2$ beyond 1200 ºC and that of $Ti_2Al(C_{0.5},N_{0.5})$ occurred at relatively lower temperature ~1150 ºC. The fact that $Ti_3Al(C_{0.5},N_{0.5})_2$ maintained higher strength and higher hardness than $Ti_2Al(C_{0.5},N_{0.5})$, indicates that the number of MX layers separating the A layers influences the mechanical properties in MAX family.

6: Effect of X-Site Substitutions on the Room Temperature Kinking Nonlinear Behavior under Compression

6.1 Introduction

Recently [63, 87, 90-94] it has been shown that the MAX phases, mica, graphite and most probably ice, can be classifies as kinking nonlinear elastic (KNE) solids. These solids deform primarily by kinking and the formation of kink bands. Kinking – a mechanism first reported by Orowan [95] in single crystals of Cd loaded parallel to the basal planes-has also been identified as the physical origin of the hysteretic, nonlinear elastic behavior exhibited by these solids [87, 90-94]. The loading-unloading stress-strain curves of KNE solids outline nonlinear, fully reversible, reproducible, closed hysteretic loops whose shape and extent of energy dissipated are strongly influenced by grain size, with the energy dissipated being significantly larger in the coarse-grained material [87]. These unique characteristics of the mechanical response of KNE solids are attributed to the formation and annihilation of incipient kink bands (discussed in more detail later).

The mechanical behavior of KNE solids can be attributed largely to the following known facts about these solids: i) Basal slip, and only basal slip, is operative at all temperatures [36, 96]. ii) Because they are confined to the basal planes, dislocations arrange themselves either in arrays (pileups) on the same slip plane, or in walls (tilt and twist boundaries) normal to the arrays [1, 36, 96, 97]. Dislocation interactions, other than orthogonal, are difficult and unlikely to occur. Hence dislocations can move back and forth reversibly and extensively. iii) Because of their high c/a ratios, twinning is unlikely, and has never been observed. Instead,

deformation occurs by a combination of glide and the formation of kink bands within individual grains [96, 97].

To date, no work exists on the effect of A- or X-site substitutions on the kinking nonlinear behavior of the MAX phases. This work, for the first time, addresses the influence of X-site substitutions on the kinking behavior of $Ti_2Al(C_{0.5},N_{0.5})$ (211) and $Ti_3Al(C_{0.5},N_{0.5})_2$ (312) solid solutions. The results are compared with those of Ti_3SiC_2 [87], Ti_3GeC_2 [this work] and Ti_2AlC [94]. The values of the remote shear stress needed to initiate kinking was obtained experimentally and compared to those obtained on the basis of a microscale model for KNE solids developed recently [90, 94]. This model, developed by Barsoum et al. [90] and later modified by Zhou et al. [94] is not a part of this dissertation. The sole purpose of the description of this model is to have a better understanding of the results reported later.

6.2 Microscale Models for KNE solids

In general the total strain ε_{tot}, at any stress σ, is comprised of a linear elastic component, viz. $\varepsilon_{LE} = \sigma/E$, where E is Young's modulus and a nonlinear elastic component ε_{NL}. The latter, in turn, is comprised of two components: one due to the formation of incipient kink bands, ε_{IKB}, the other to dislocation pileups, ε_{DP}. In contradistinction to other crystalline solids – where dislocations are *not* confined to the basal planes as they are in KNE solids – both strains are fully reversible up to strain levels that can be significantly larger than the elastic strain limits in conventional linear elastic crystalline solids.

If the total area under the stress-strain curve in loading a KNE solid to a stress level of σ is W, the energy stored due to the creation of dislocations – in the form of IKBs (U_{IKB}) and/or dislocation pileups, (U_{DP}) – is given by [90]:

$$U_{NL} = U_{IKB} + U_{DP} = W - W_d/2 - U_{LE} \tag{6.1}$$

where W_d and U_{LE} are, respectively, the energy dissipated per cycle and the stored linear elastic energy both per unit volume. How the various terms relate to a typical KNE stress/strain curve is shown schematically in Fig. 6.1. Experimentally ε_{NL}, W_d and U_{NL} are readily measurable. The rationale for dividing W_D by two is that approximately half the energy dissipation occurs during loading and half during unloading.

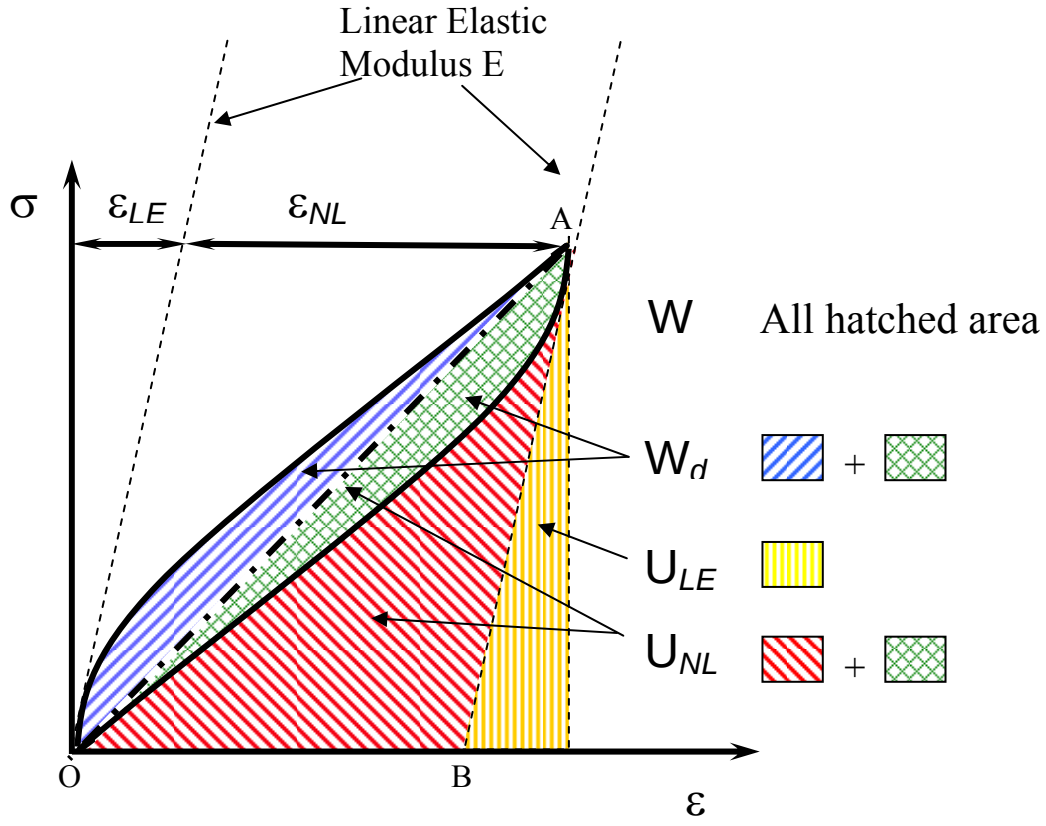

Figure 6.1: Schematic of a typical stress-strain curve for a KNE solid. The various parameters needed to describe the curve are labeled and color-coded. Note U_{NL} = area of triangle OAB.

Frank and Stroh [98], F&S, considered the growth of a subcritical kink band of dimensions, 2α and 2β, such that 2α >> 2β (Fig. 6.2). The critical kinking angle (or shear strain), γ_c, is given by [14]:

$$\gamma_c = \frac{b}{D} \approx \frac{3\sqrt{3}(1-\nu)\tau_{loc}}{2G} \tag{6.2}$$

where b is the Burgers vector. D is the distance between dislocations along 2α (Fig. 6.2). ν is Poisson's ratio; τ_{loc} is the local shear stress needed to form a dislocation pair, typically assumed to be ≈ G/30,-where G is the shear modulus [98].

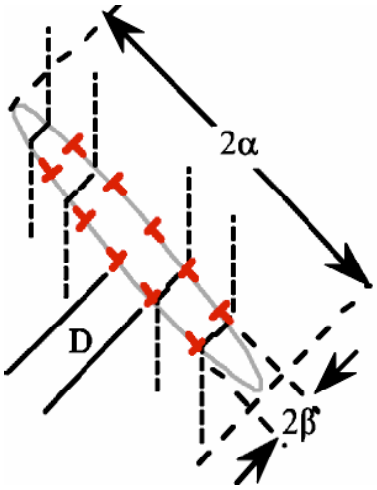

Figure 6.2: A thin elliptical subcritical kink nucleus with 2α >> 2β.

F&S showed that the remote shear stress, τ, needed to render a subcritical kink band unstable and grow depends on 2α and is given by [98]:

$$\tau > \tau_c \approx \frac{\sigma_c}{k_1} \approx \sqrt{\frac{2bG^2\gamma_c}{\alpha\pi^2}\ln\frac{b}{w\gamma_c}} \tag{6.3}$$

where τ_c and σ_c are the critical shear and uniaxial stresses, respectively. k_1 is a factor that relates the shear stress to the uniaxial stress. F&S modelled pure edge dislocations, which introduces a (1 - ν) term in the denominator of Eq. 6.3. This term was omitted here, and in the reminder of this chapter because in the MAX phases the dislocations, while perfect, are mixed and self organize in walls such that the screw components alternate, hence reducing their energy [96]. w is related to the dislocation width and is of the same order as the Burgers vector, b [98].

For a given IKB, 2β is related to α and stress according to [94, 98]:

$$2\beta \approx \frac{2\alpha(1-\nu)}{k_1 G\gamma_c}(\sigma-\sigma_t) \tag{6.4}$$

where σ_t is a threshold stress below which no kinking occurs. Note that in most cases, σ_t is given by Eq. 6.2. The IKB strain can be expressed as [94, 98]:

$$\varepsilon_{IKB} = \frac{2\pi\alpha\beta^2\gamma_c N_k}{k_2} \tag{6.5}$$

Combining Eqs. 6.4 and 6.5, it can be shown that:

$$\varepsilon_{IKB} \approx \frac{1}{k_1^2 k_2}\cdot\frac{2\pi(1-\nu)^2}{G^2\gamma_c}\cdot N_k\alpha^3\cdot(\sigma-\sigma_t)^2 \tag{6.6}$$

where N_k is the number of incipient kink bands per unit volume. k_2 represents a factor that relates the local IKB shear strain, at the grain level, to the macroscale uniaxial strain of the sample (see below).

Combining the fact that $U_{IKB} = ½\ \varepsilon_{IKB}\ (\sigma - \sigma_t)$ with Eq. 6.6, one obtains:

$$U_{IKB} = k_1\sqrt{k_2}\sqrt{\frac{G^2\gamma_c}{8\pi(1-\nu)^2 N_k\alpha^3}}\cdot\varepsilon_{IKB}^{1.5} \tag{6.7}$$

Previously it was shown that [90, 94]:

$$W_d = 2N_k\pi\beta^2\ \frac{2\alpha}{\mathrm{D}}\Omega \tag{6.8}$$

where Ω is the energy dissipated by a dislocation loop of unit length sweeping a unit area. Using Eq. 6.4 to eliminate β results in [94]:

$$W_d = \frac{4\pi\Omega N_k\alpha^3}{k_1^2 G^2\gamma_c b}\cdot(\sigma-\sigma_t)^2 \tag{6.9}$$

It is worth noting here that in F&S paper, σ_t in Eq. 6.4 was assumed to be zero. Consequently in previous work [90], σ_t in Eq. 6.4 was also assumed to be zero, which resulted in an expression in which W_d was proportional to $(\sigma^2 - \sigma_t^2)$. Later Zhou et al. [94] showed that Eq. 6.9 is a more accurate expression and should be the one used.

Lastly, multiplying Eq. 6.9 and the square of Eq. 6.7, rearranging, it can be shown that [90, 94]:

$$W_d = k_2\frac{2}{(1-\nu)^2}\frac{\Omega}{b}\varepsilon_{IKB} \tag{6.10}$$

This expression combines three macroscopic parameters (ε_{IKB}, W_d and k_2), two constants (b and ν) and one microscopic parameter, Ω. In the above equations, k_1 and k_2 are factors that are dependent on the sample's microstructure and can be assumed to be $k_1 \approx k_2 \approx 2$.

6.3 Experimental Details

Uniaxial compression (UC) tests were performed on cylindrical shaped specimens (9.7 mm in diameter and 31 mm high); the gauge length was 25 mm. Samples were electro-discharge machined and tested with no further surface preparation. The compression tests were performed using a hydraulic testing machine (MTS 810, Minneapolis, MN), supplied with a controller (Microconsoler 458.20, MTS), and a 50 kN capacity load cell. In all tests, a preload, that corresponded to a stress of about 1 ~ 2 MPa, was applied to keep the samples aligned. All the cyclic loading-unloading tests were performed in load-control mode at a loading rate of 2 kN/s. Strains were measured by a capacitance extensometer (MTS, Minneapolis, MN) with a range of 1% strain.

6.4 Results and Discussion

6.4.1 312 Systems

Figure 6.3 shows the cyclic compressive stress-strain curves of FG and CG Ti_3GeC_2. Similar to Ti_3SiC_2 [87], here also, microstructure dependent, nonlinear and closed hysteretic loops are observed.

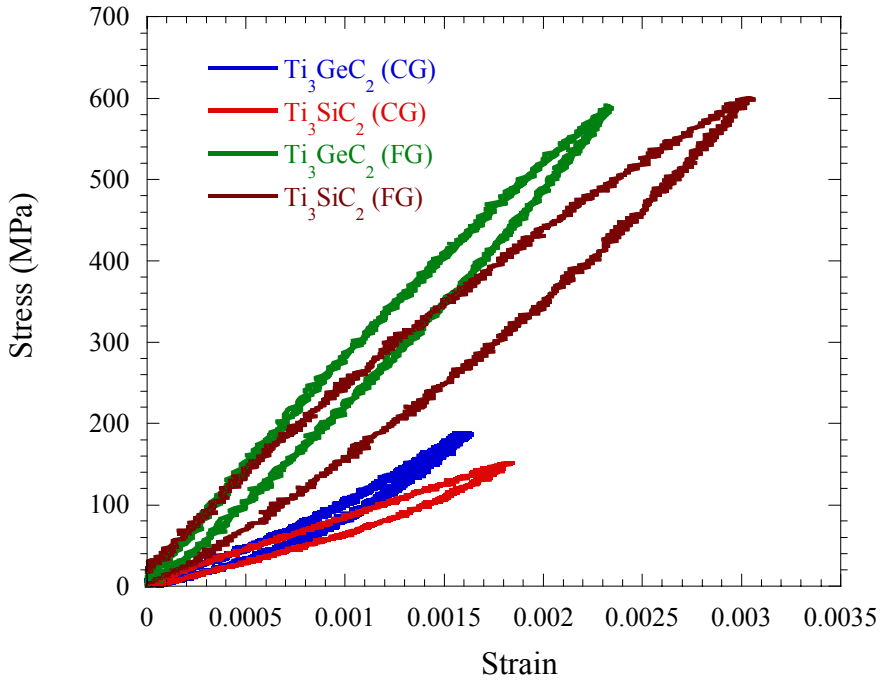

Figure 6.3: Stress-strain curves for FG and CG Ti_3GeC_2. Each loop represents three consecutive cycles for each microstructure. Also plotted are corresponding values for Ti_3SiC_2 [87] for the sake of comparison.

Typical cyclic stress-strain curves for FG Ti_3GeC_2 are shown in Fig. 6.4 (a). In the first cycle the sample was loaded to a stress of 300 MPa; in each successive cycle the stress was increased up to the maximum of 600 MPa. In case of medium-grained, MG $Ti_3Al(C_{0.5},N_{0.5})_2$, (Fig. 6.4 b) however, no loop was observed below 400 MPa.

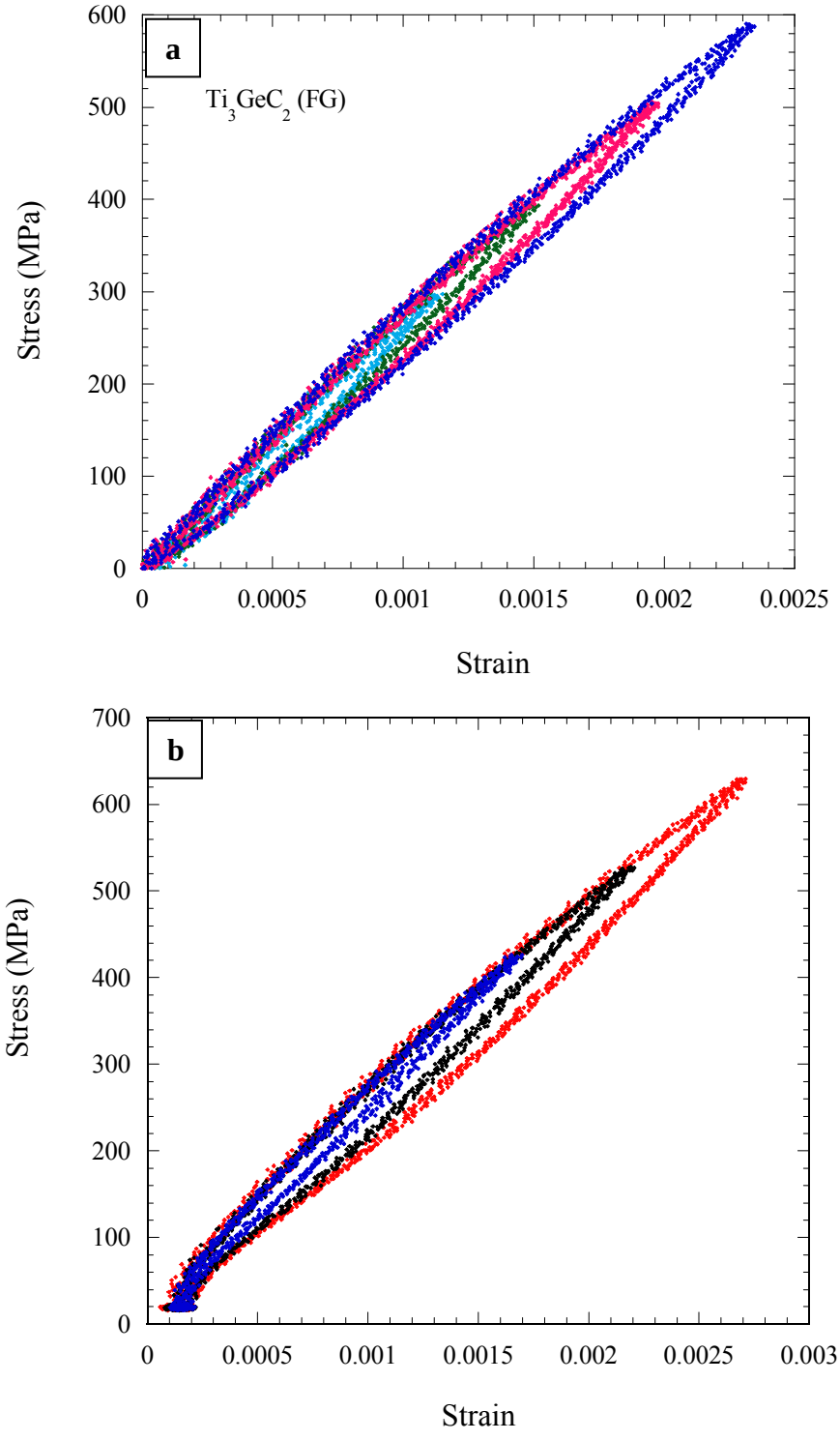

Figure 6.4: Stress-strain uniaxial cyclic compression results of (a) FG Ti_3GeC_2 and (b) MG $Ti_3Al(C_{0.5},N_{0.5})_2$.

Table 6.1 Material constants for Ti_3GeC_2, $Ti_3Al(C_{0.5},N_{0.5})_2$, $Ti_2Al(C_{0.5},N_{0.5})$ and Ti_3SiC_2 [1, 31, 43] and other values derived in this work to estimate σ_c and Ω/b.

Sample	G (GPa)	υ	b (Å)	*w*/b	γ_c (rad)	Grain thickness (μm)
Ti_3GeC_2	135	0.196	3.09	13	0.072	2
$Ti_2Al(C_{0.5},N_{0.5})$	122.6	0.182	3.023	5	0.072	4±2
$Ti_3Al(C_{0.5},N_{0.5})_2$	136.6	0.209	3.04	7	0.072	4±2
Ti_3SiC_2	143.8	0.200	3.0665	13	0.072	2

Figure 6.5 plots U_{NL} vs. $\varepsilon_{NL}^{1.5}$ obtained from the uniaxial compression stress-strain curves for FG Ti_3GeC_2, MG $Ti_3Al(C_{0.5},N_{0.5})_2$ and FG Ti_3SiC_2 [87]. In each case, least square fits yield values of R > 0.999.

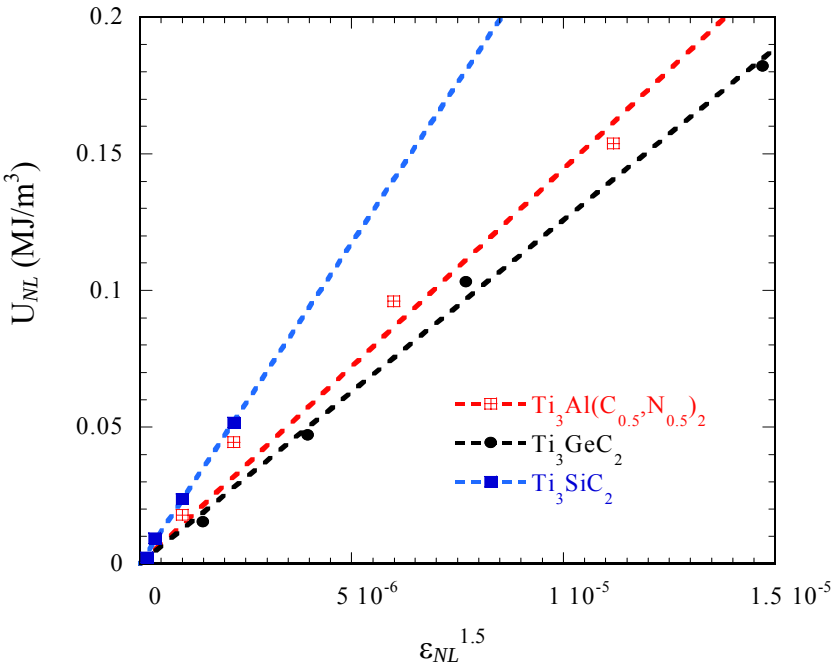

Figure 6.5: Plots of UNL vs. $\varepsilon_{NL}^{1.5}$ obtained from uniaxial compression stress-strain curves for FG Ti_3GeC_2, MG $Ti_3Al(C_{0.5},N_{0.5})_2$ and FG Ti_3SiC_2 [87].

If it can be assumed that $U_{DP} << U_{IKB} \approx U_{NL}$, and $\varepsilon_{IKB} \approx \varepsilon_{NL}$, and provided $N_k\alpha^3$ is not a strong function of stress, then according to Eq. 6.7, plots of U_{NL} vs. $\varepsilon_{NL}^{1.5}$ should result in straight lines. The actual plots (Fig. 6.5) are quite gratifying and bear this relationship out. As $\alpha^3 N_k$ is not a strong function of stress, then, according to Eq. 6.9, plots of $W_d^{1/2}$ versus σ, should also yield straight lines with x-axis intercepts that correspond to the threshold stresses. That such plots are indeed linear, for both FG Ti_3GeC_2 and MG $Ti_3Al(C_{0.5},N_{0.5})_2$, is evident from Fig. 6.6. In both cases, least squares fits yield values of $R > 0.99$.

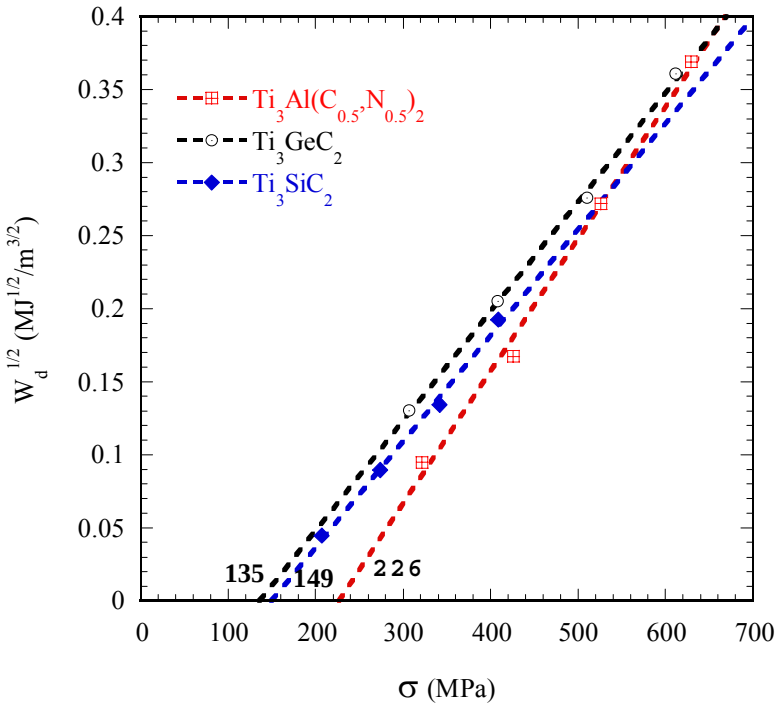

Figure 6.6: Plot of $W_d^{1/2}$ vs. σ obtained from uniaxial compression stress-strain curves for FG Ti_3GeC_2 and MG $Ti_3Al(C_{0.5},N_{0.5})_2$. Also plotted are corresponding values of Ti_3SiC_2 for the sake of comparison [87].

It is evident from Fig. 6.6 that substitution on the X-sites in the 312 system increases the threshold stress needed for the growth of a subcritical kink band. It is worth mentioning here, that x-axis intercept for the solid solution yields a higher value of threshold stress (which varies inversely with grain size according to Eq. 6.3) than that of Ti_3GeC_2 and Ti_3SiC_2, despite the fact that grain size of the former is larger than the latter. The experimentally determined value of σ_t decrease in the following order: $Ti_3Al(C_{0.5},N_{0.5})_2$ (226 MPa) > Ti_3SiC_2 (149 MPa) > Ti_3GeC_2 (135 MPa).

Applying Eq. 6.3 as per the microscale model and using the material constants listed in Table 6.1, critical kinking stress σ_c, of an average grain for $Ti_3Al(C_{0.5},N_{0.5})_2$ was calculated to be 239.7 MPa by assuming the value of adjustable parameter *w* as 7b. Applying the same equation for Ti_3GeC_2 and Ti_3SiC_2 and adjusting *w*~13b results in σ_c values of 123 and 127 MPa, respectively. This clearly indicates that substitution on the X-sites in the 312 MAX phases lowers the parameter *w* nearly by a factor of two, thereby decreasing the width of dislocations. As far as the author is aware, no one has ever reported about the compositional dependence of dislocation width for any MAX phase to date. This work for the first time shows that a correlation between X-site substitution and dislocation width even exists for the MAX family.

Finally, a plot of W_d vs. ε_{NL} (Fig. 6.7) also results in straight lines with values of R > 0.999, which is in good agreement with Eq. 6.10. The values of Ω/b calculated (assuming $k_1 = k_2 = 2$) decreases in the following order: $Ti_3Al(C_{0.5},N_{0.5})_2$ (51 MPa)> Ti_3SiC_2 (41 MPa)> Ti_3GeC_2 (39 MPa).

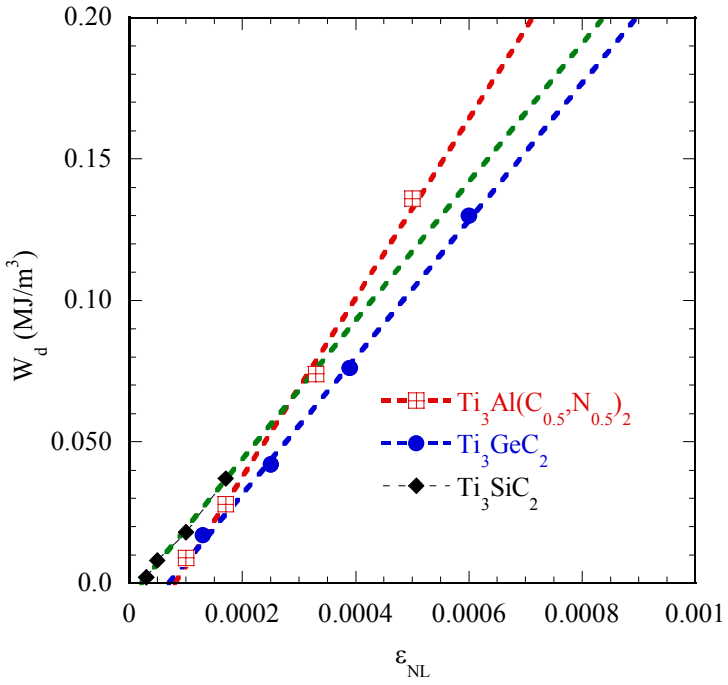

Figure 6.7: Plot of W_d vs. ε_{NL} for uniaxial compression of $Ti_3Al(C_{0.5},N_{0.5})_2$, Ti_3SiC_2 [90] and Ti_3GeC_2.

Based on the definition of Ω, it is reasonable to expect that Ω/b to be closely related to, if not identical to, the critical resolved shear stress (CRSS) of dislocations gliding along the basal planes. Here again, it is evident that substitution on the X-site significantly increases the CRSS.

6.4.2 211 Systems

Typical cyclic stress-strain curves for medium grained (MG-vide chapter 2 for detail) $Ti_2Al(C_{0.5},N_{0.5})$ are shown in Fig. 6.8 (a), while Fig. 6.8 (b) compares the hysteretic loops traced out by the solid solution composition and CG Ti_2AlC [94] at more or less similar stress levels.

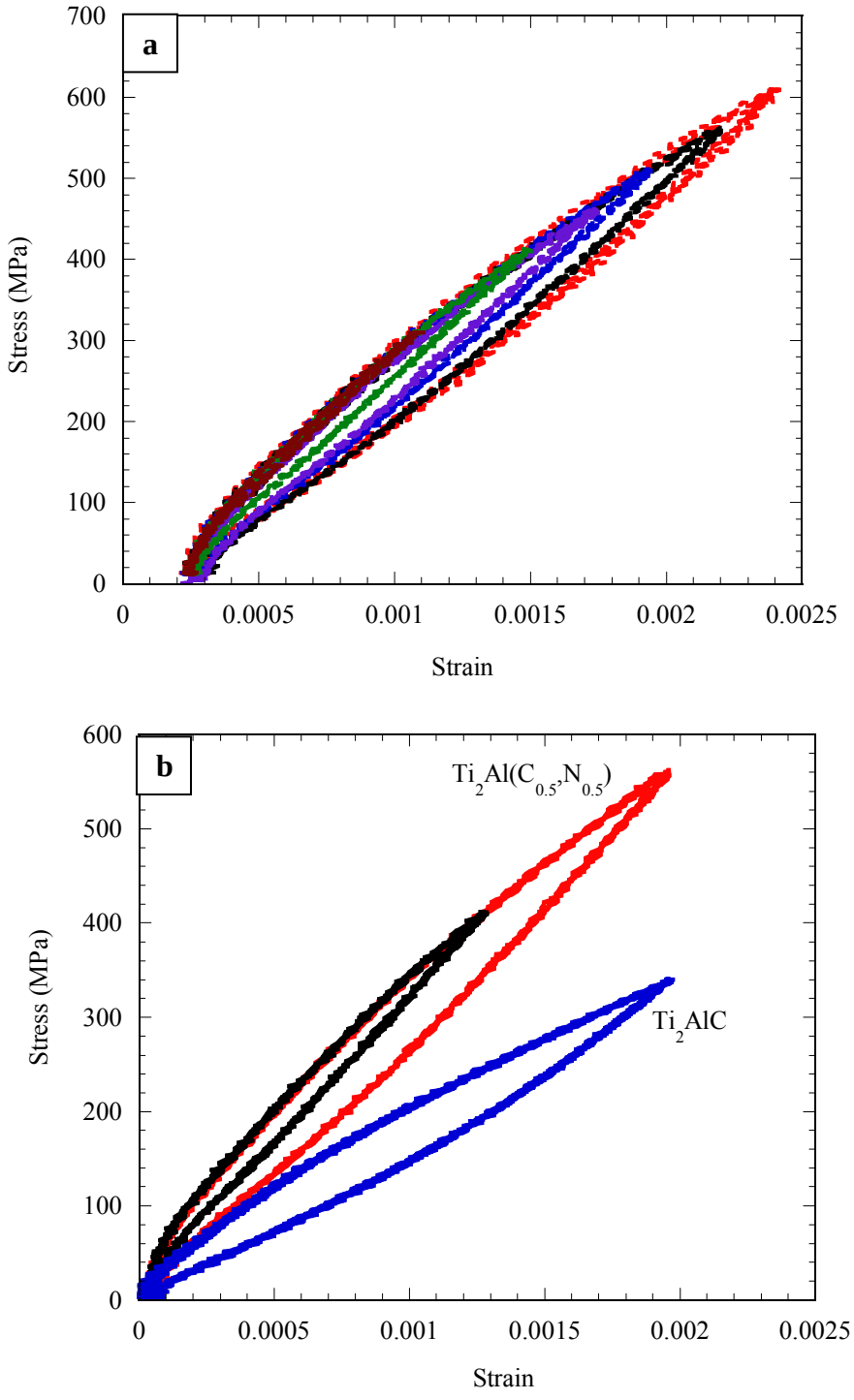

Figure 6.8: Stress-strain uniaxial cyclic compression result of, (a) MG $Ti_2Al(C_{0.5},N_{0.5})$, and, (b) The same compared to that of CG Ti_2AlC [94].

In the first cycle, the sample was loaded to a stress of 300 MPa, but no loop was observed (the brown line in Fig. 6.8 a); in each successive cycle the stress was increased up to the maximum of 600 MPa. Note that the slope of the solid solution loops upon initial unloading is higher than that of Ti_2AlC indicating higher stiffness.

Figure 6.9 plots U_{NL} vs. $\varepsilon_{NL}^{1.5}$ obtained from the uniaxial compression stress-strain curves for MG $Ti_2Al(C_{0.5},N_{0.5})$ and those of CG Ti_2AlC [94]. In each case, least square fits yield values of $R > 0.999$.

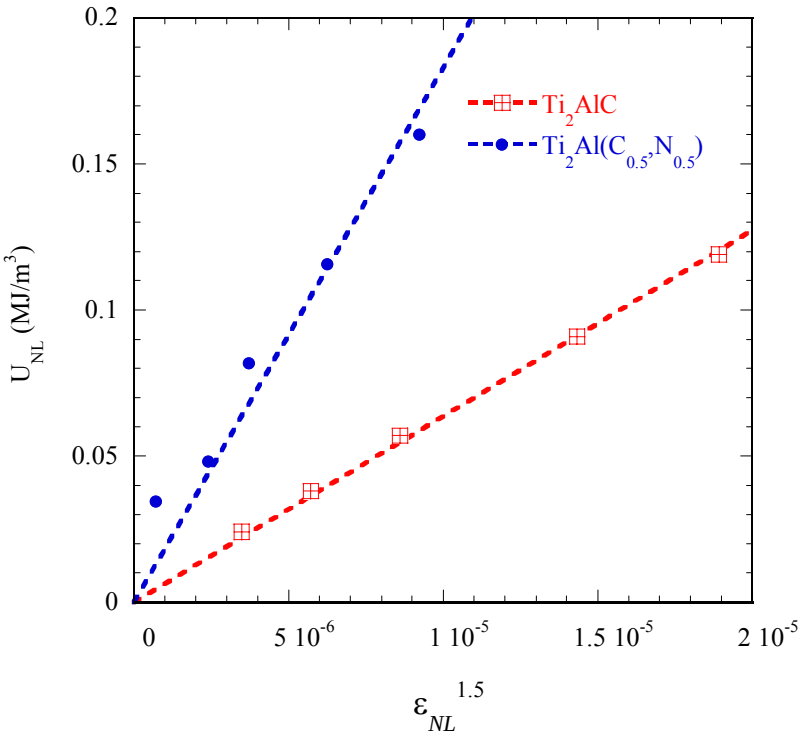

Figure 6.9: Plots of UNL vs. $\varepsilon_{NL}^{1.5}$ obtained from uniaxial compression stress-strain curves for MG $Ti_2Al(C_{0.5},N_{0.5})$ and that of CG Ti_2AlC [94].

Here again, applying a similar approach as that of section 6.4.1 and considering the fact that the plot of U_{NL} vs. $\varepsilon_{NL}^{1.5}$ is linear it is fair to assume that $\alpha^3 N_k$ is not a strong function of stress. Hence, a plot of $W_d^{1/2}$ versus σ, should yield straight lines with x-axis intercepts that correspond to the threshold stresses. Figure 6.10 shows that such a plot indeed is linear with values of $R > 0.99$.

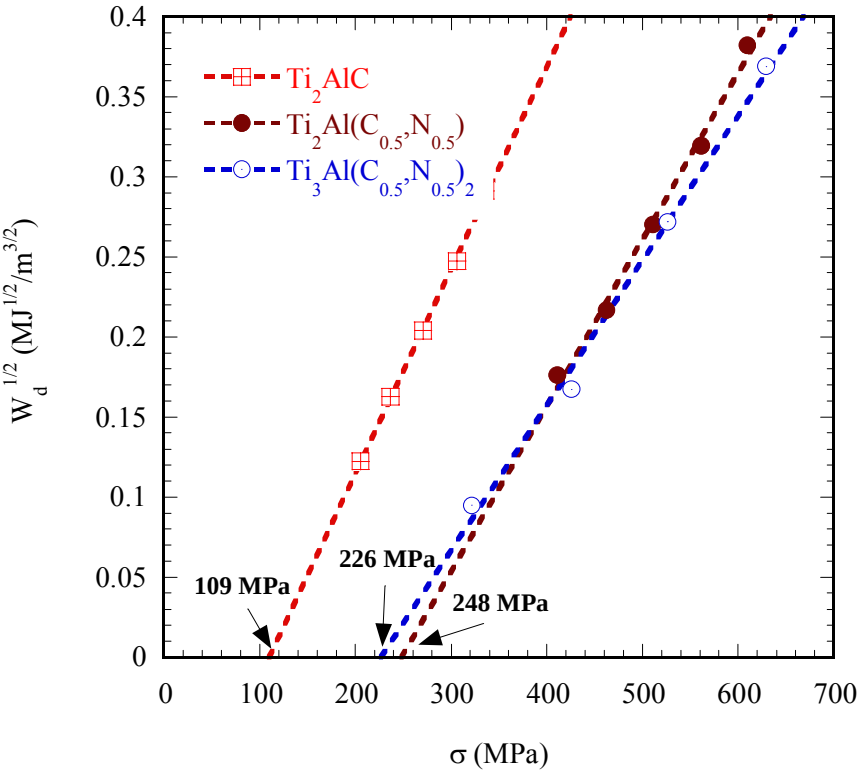

Figure 6.10: Plot of $W_d^{1/2}$ vs. σ obtained from uniaxial compression stress-strain curves for MG $Ti_2Al(C_{0.5},N_{0.5})$, $Ti_3Al(C_{0.5},N_{0.5})_2$. Also plotted are corresponding values of CG Ti_2AlC [94] for the sake of comparison.

Here again, like the 312 system, substitution on the X-site in 211 system increases the threshold stress needed for IKB formation.

The experimentally determined value of σ_t decreases in the following order: $Ti_2Al(C_{0.5},N_{0.5})$ (248 MPa)> $Ti_3Al(C_{0.5},N_{0.5})_2$ (226 MPa)> Ti_2AlC (109 MPa). The value of $Ti_3Al(C_{0.5},N_{0.5})_2$ is cited here just for the sake of comparison.. From the results, it appears that at comparable grain size (MG), a decrease in the number of M-X layers separating the A layers increases the threshold stress value. This comment, not withstanding, it is hereby acknowledged, that more work is needed to understand the effect of number of M-X layers/blocks on the threshold stress.

Here also, applying Eq. 6.3 as per the microscale model and using the material constants mentioned in Table 6.2 and assuming the adjustable parameter *w* as 5b, the critical kinking stress σ_c, of an average grain for $Ti_2Al(C_{0.5},N_{0.5})$ was calculated to be 269 MPa. Applying the same equation for Ti_2AlC results in *w* = 10b [94] and corresponding σ_c value as 100 MPa. This clearly indicates that substitution on the X-site in 211 systems lowers the parameter *w* by a factor of two and in turn reduces the dislocation width. This observation is in excellent agreement with the results obtained for the 312 systems.

A plot of W_d vs. ε_{NL} (Fig. 6.11) also results in straight lines with values of R > 0.999, which is in good agreement with Eq. 6.10. The values of Ω/b calculated (assuming $k_1 = k_2 = 2$) decreases in the following order: $Ti_2Al(C_{0.5},N_{0.5})$ (56 MPa)> $Ti_3Al(C_{0.5},N_{0.5})_2$ (54.5 MPa) > Ti_2AlC (24 MPa).

As expected, substitution on the X-sites in the 211 systems significantly increases the CRSS (Ω/b).This observation is also very similar to the behavior of 312 carbo-nitride.

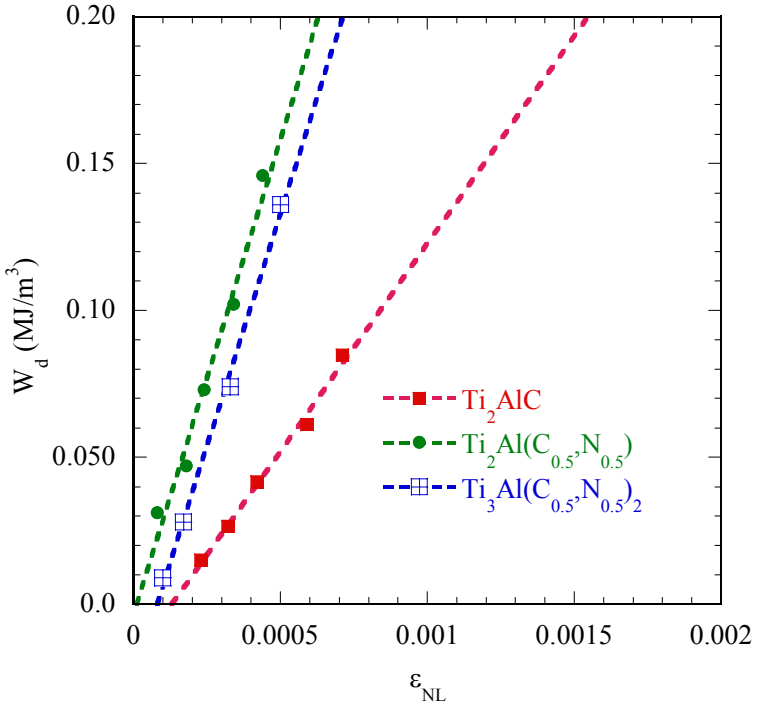

Figure 6.11: Plot of W_d vs. ε_{NL} for uniaxial compression of $Ti_2Al(C_{0.5},N_{0.5})$, $Ti_3Al(C_{0.5},N_{0.5})_2$ and Ti_2AlC [94].

6.5 Conclusions

The uniaxial compression results on Ti_3GeC_2 and $Ti_2Al(C_{0.5},N_{0.5})$, $Ti_3Al(C_{0.5},N_{0.5})_2$ solid solution compositions unequivocally show that all three compositions are KNE solids. Substitutions on the X-sites in both the 312 and 211 systems increases the threshold stress (σ_c), critical resolved shear stress (Ω/b), and lowers the parameter *w* by a factor of two which renders dislocation nucleation and motion more difficult.

7: Mechanical Damping Behavior

7.1 Introduction

By now it is fairly well established that MAX phases deform by a combination of glide and kinking [1, 7, 87, 88, 91, 96, 97, 99]. Basal, and only basal, slip is operative and dislocations are overwhelmingly arranged either in pileups on the same basal plane, or in walls. Dislocation interactions, other than orthogonal, are difficult, unlikely to occur and have never been observed. Unlike metals the dislocations do not entangle and work hardening in the classic sense, e.g. by the formation of dislocation forests, etc. has also not been observed. This does not imply that hardening does not occur. The hardening that does occur is a direct result of the formation of kink boundaries that effectively reduce the domain size. Most importantly, because the dislocations are restricted to the basal planes and do not entangle, they can move back and forth over significant distances. This results in the dissipation of large amounts of energy per loading cycle. The energy dissipated also *increases* as the square of the applied stress [87, 90].

As already discussed in Ch. 6, the MAX phases, and any other solid with a high ($> \approx 2$) c/a ratio, will deform, if at all, by the formation of incipient (IKB) and regular kink bands (KB). The reason this is deemed a sufficient, but *not* necessary, condition is simple: with high c/a ratios the lengths of the Burgers vectors of non-basal dislocations render them prohibitively expensive. Furthermore, twinning – other than basal twinning - is not an option [93]. These solids thus have only two mechanisms to relieve the stress: fracture and/or formation of kink bands, KBs. If the latter occurs, the solids can be best described as kinking nonlinear elastic, or KNE,

solids. The signature of a KNE solid is the formation of reversible hysteretic stress/strains loops during quasi-static loading-unloading cycles [87, 88, 99].

The detail of non-linear elastic behavior of KNE solids has already been described in Ch. 6. The non-linear elastic behavior of KNE solids, in general, and the MAX phases in particular, makes it difficult to accurately determine their elastic moduli from quasi-static stress-strain curves. This is especially true at elevated temperatures, i.e. above brittle-to-plastic transition temperature (BPTT). This is one reason the elastic properties of the MAX phases in Ch. 3 were determined by using either an Ultrasound Echo Pulse (UEP) technique or by Resonant Ultrasound Spectroscopy (RUS). In addition to the elastic constants, RUS also allows one to study the mechanical damping of a material under dynamic conditions as a function of temperature, grain size and deformation history.

Recently Barosum et al. [63] reported on the elastic properties of Ti_3SiC_2 determined from RUS and UEP, in the room temperature to 1573 K temperature range. It was observed that that while the elastic moduli decreased linearly with temperature up to 1573 K, the mechanical damping, Q^{-1}, was constant up to ≈ BPTT, above which it increased dramatically. Most importantly, the response of Ti_3SiC_2 at room temperature to the increasing driving voltage, i.e., increasing strain amplitude, resulted in a linear downshift in the frequencies of the resonance peaks, which is typical of non-linear mesoscopic elastic solids that play an important role in geology [100, 101]. As important modest (4 % strain) pre-deformation at elevated temperatures resulted in a more than an order of magnitude increase in the damping properties which led Barsoum et al. to conclude that the damping is due to the

interaction of dislocations segments with the ultrasound waver. The damping capabilities of MAX phases are orders of magnitude higher than typical structural ceramics, and comparable to those of some woods.

Under dynamic conditions Q^{-1} was also an order of magnitude lower than that obtained from quasi-static conditions and dependent on frequency, ω, and previous loading history, but *not* on grain size [63]. The non-linear behavior of Ti_3SiC_2 under dynamic conditions was thus attributed to the interaction of preexisting dislocation line segments with the ultrasonic waves and not due to the formation and annihilation of IKBs as in quasistatic conditions.

This chapter reports on the damping properties of Ti_3GeC_2 and $Ti_3Si_{0.5}Al_{0.5}C_2$ in the 300-1573 K temperature range using RUS and compares the results obtained with those of Ti_3SiC_2 and Ti_2AlC [28].

7.2 Experimental Details

The details of the experimental procedure have already been described in Ch. 3 (section 3.3.3.2). The internal friction, Q^{-1}, was determined from the RUS spectra assuming [64, 65, 67]:

$$Q_k^{-1} = \Delta \omega_k / \omega_{k0} \quad (7.1)$$

where ω_{k0} is the frequency associated to with k^{th} eigenmode and $\Delta \omega_k$ is the full width at half maximum, FWHM, of that mode.

7.3 Results and Discussion

When the temperature dependencies of Q^{-1} at select resonant frequencies for Ti_3SiC_2, Ti_2AlC, and $Ti_3Si_{0.5}Al_{0.5}C_2$ are plotted (Fig. 7.1) a clear and dramatic increase in Q^{-1} at ≈ 1273 K - that is independent of the eigenmode - is observed. For Ti_3GeC_2, Q^{-1} is again almost temperature independent up to ≈ 723 K for all eigenmodes; above this temperature, the Q^{-1} values increase significantly. This decoupling of real (E, μ) and imaginary components is unusual and implies that the loss mechanisms are decoupled from those responsible for the moduli – i.e. bond stiffnesses.

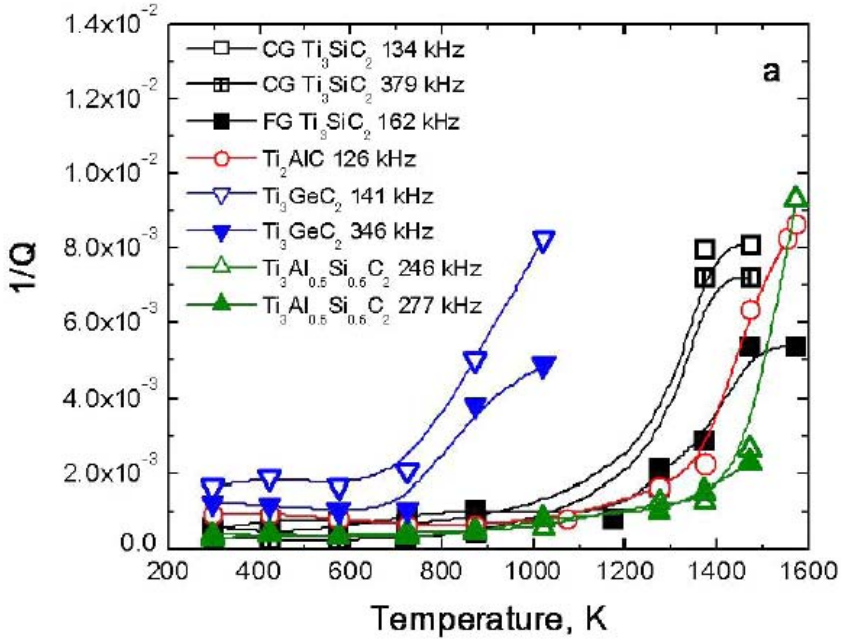

Figure 7.1: Q^{-1} vs. temperature for Ti_3GeC_2 and $Ti_3Si_{0.5}Al_{0.5}C_2$ for selected frequencies. Also plotted are the corresponding results of Ti_3SiC_2 and Ti_2AlC [28].

The effects of temperature on Q^{-1} are also evident in Arrhenius plots of Q^{-1} (Fig. 7.2). Up to ≈1273 K, Q^{-1} is almost temperature independent. Above that temperature the activation energies range from 70±11 kJ/mol to 115±23 kJ/mol. The activation energy of 29±2 kJ/mol for Ti_3GeC_2, is significantly lower than those determined for the other ternaries.

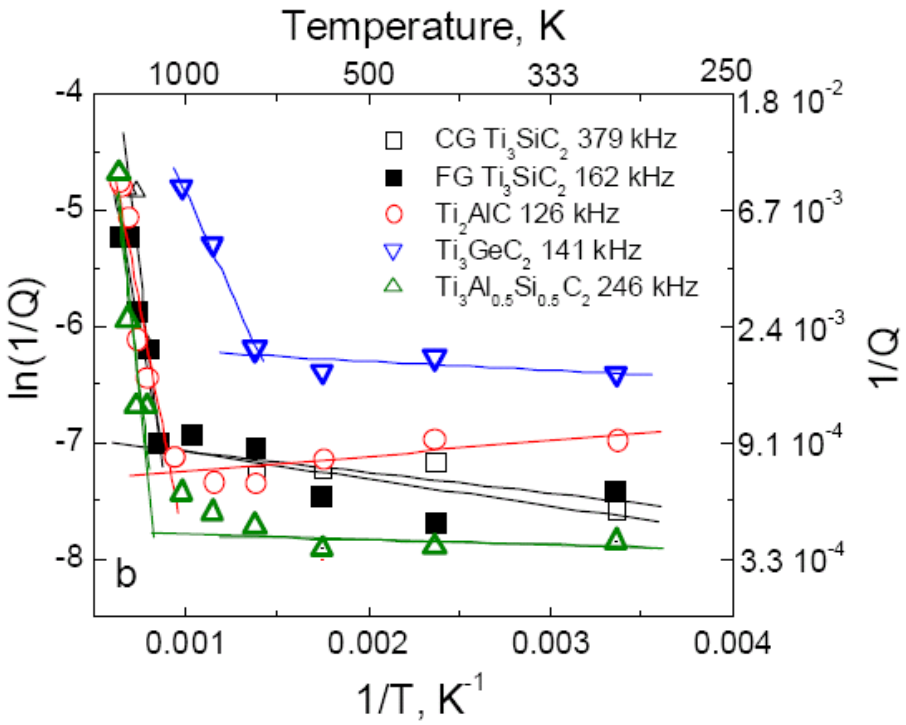

Figure 7.2: Arrhenius plots of $\ln Q^{-1}$ for selected frequencies.

The values of Q^{-1} measured in this work are several orders of magnitude higher than those of structural ceramics with comparable stiffnesses such as SiC and Si_3N_4; the values are comparable to some good damping metals.

The values of Q^{-1} measured herein are also at least an order of magnitude lower than those previously obtained at the higher stress/strain amplitudes and low frequencies of cyclic loading-unloading tests [87]. To understand this discrepancy in Q^{-1} it is crucial to underscore the differences between the results obtained in this work with those obtained in more classic mechanical tests such as cyclic compression and tension [87, 88].

First, the frequency range used in RUS (20-450 kHz) is orders of magnitude higher than the range used in mechanical testing. Second, and more important, the stresses and strains generated during RUS are orders of magnitude lower than those in typical mechanical testing [102]. This implies that ultrasound energy applied during RUS is insufficient to nucleate IKBs in the compositions explored here in. The evidence for this conclusion is multifold and can be summarized as follows:

(a) The fact that the elastic moduli (discussed in Ch. 3 under subsection 3.3.3) do not drop dramatically at ≈ 1173 K in the case of Ti_3SiC_2, $Ti_3Si_{0.5}Al_{0.5}C_2$, and Ti_2AlC as they do in tension [88], compression [87] or bending [22] implies that the plastic deformation during RUS is small. Recall this drop is attributed to the formation of KBs and dislocation arrays [36].

(b) As has been shown in Ch. 6 the threshold stress required to nucleate IKBs ranges from 100-250 MPa. Such stresses are certainly beyond what was generated in this work.

(c) It is well known that the threshold stress required to generate IKBs is microstructure dependent [87]. The threshold stress required for CG samples are much lower than that for FG samples which results in lower apparent moduli and higher damping for CG samples [87]. Since this behavior is not seen here, IKBs or KBs cannot be implicated.

(d) The weak dependence of Q^{-1} on grain size (Fig. 7.2), rules out grain boundaries as a source of damping.

Figure 7.3 shows a semi log plot of mechanical damping as a function of frequencies. This plot compares the mechanical damping of each composition at room temperature vs. high temperature. It also compares the damping behavior for fine and coarse grained samples of the same composition. The influence of deformation history (discussed in section 7.1) for Ti_3SiC_2 is also shown.

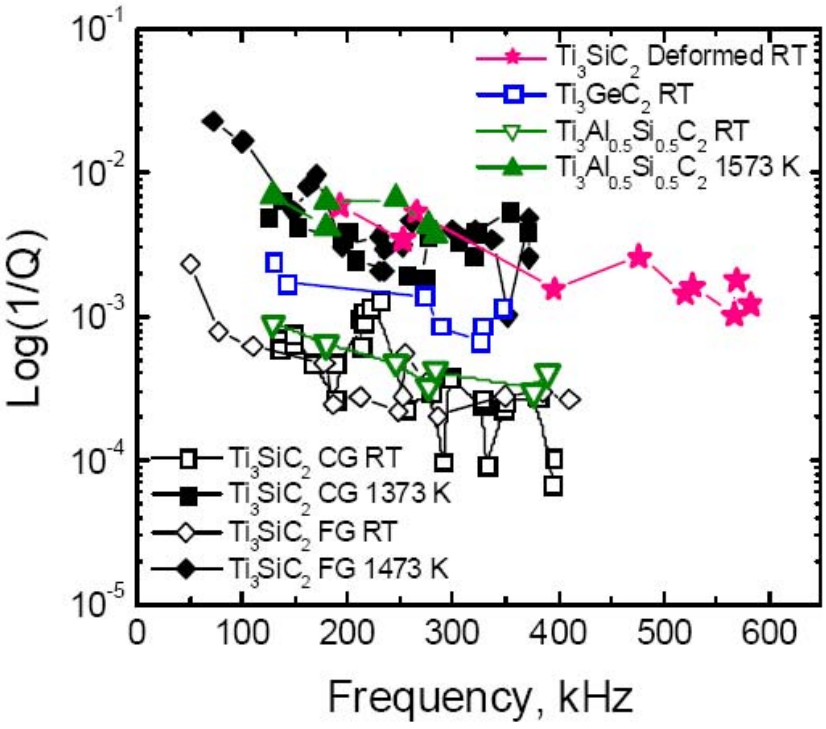

Figure 7.3: Q^{-1} vs. frequency at room and elevated temperatures.

At all frequencies Q^{-1} were about an order of magnitude higher at elevated temperatures than at room temperature for the three compositions depicted here- Ti_3SiC_2, Ti_3GeC_2 and $Ti_3Si_{0.5}Al_{0.5}C_2$ (Fig. 7.3). Comparing Q^{-1} for the fine and coarse grained Ti_3SiC_2 samples, it is evident that grain size has little or no influence on mechanical damping. Figure 7.3 also clearly shows that Q^{-1} is a strong function of deformation history- Q^{-1} for Ti_3SiC_2 pre-deformed at elevated temperature (4 % strain) followed by cooling down to room temperature is about a magnitude higher than that of FG or CG samples.

The very fact that the damping is a strong function of deformation history (Fig. 7.3) is compelling evidence that it is dislocation-based. The additional evidence for this is the fact that the 4% pre-deformation also results in a stiffening and hardening of the solid [87], which can only be accounted for by the presence of dislocations.

Since the ultrasound energy applied in RUS is insufficient to nucleate IKBs, the damping must be caused by vibration (string model) and/or movement (hysteretic model) of dislocation line segments [103] when they couple with the ultrasound energy. The increased damping for the deformed sample (Fig. 7.3) must thus be due to the increase in dislocation density [103].

It has to be emphasized that the relatively large variations in Q^{-1} with ω shown in Fig. 7.3 reflect the various eigenmodes of the vibrations. Those variations are not measurement noise and are quite typical of RUS results.

The dramatic increase in Q^{-1} with temperature is close to the brittle-to-plastic transition temperature, BPTT of Ti_3SiC_2 [7, 88], Ti_2AlC [22], and probably $Ti_3Si_{0.5}Al_{0.5}C_2$. The reason for the dramatic increase in Q^{-1} is not understood at this point and more work is needed. We only note here that whatever the process it is fully reversible; when the samples are cooled the original spectra are recovered. These comments notwithstanding there are two likely possibilities. The first is an increase in the mobilities of the dislocations. Note this increase in mobility is *not* long-range – since it does not result in plastic deformation - but a localized hopping in response to the ultrasound waves. In other words, the increase in damping is not caused by any

irreversible increase in dislocation density, such as formations of KB or dislocation arrays.

The second possibility is the creation of a large number of defects, such as vacancies, in the A-planes. The best evidence here is the case of Ti_3GeC_2 where Q^{-1} increases dramatically at a temperature, ≈ 723 K, which are considerably, lower than its BPTT [27]. It is worth noting here, that in this case the RT spectra are *not* recovered upon cooling. The presence of Ge droplets on the sample surface after RUS measurements up to 1273 K is consistent with such an interpretation. Furthermore, by now it is reasonably fairly well established that the A-group layers are relatively weakly bound to the $M_{n+1}X_n$ blocks and are thus the most reactive element in the MAX phases. For example, heating Ti_3SiC_2 in a C-rich atmosphere results in the loss of Si and the formation of TiC_x [104].

When the same compound is placed in molten cryolite [105] or molten Al [106] essentially the same reaction occurs: the Si escapes and TiC_x forms. In some cases, e.g. Ti_2InC, vacuum at elevated temperatures is sufficient to result in loss of the A-group element and the formation of TiC_x [107].

7.4 Conclusions

This work reports on the damping properties of Ti_3GeC_2 and $Ti_3Si_{0.5}Al_{0.5}C_2$ in the 300-1573 K temperature range using RUS and compares the results to those of Ti_3SiC_2 and Ti_2AlC [53]. The mechanical damping was found to be weak function of grain size and temperatures of ~1273 K $Ti_3Si_{0.5}Al_{0.5}C_2$, and ~ 700 K for Ti_3GeC_2, after which - for reasons that are not entirely clear it increases significantly.

8: Summary, Conclusions and Future Work

8.1 Summary and Conclusions

In this thesis we report on the synthesis and characterization of A- or X-site substituted MAX solid solutions. Most of the compositions synthesized in this work, with the exception of Ti_3GeC_2 and $Ti_2Al(C_{0.5}N_{0.5})$ were synthesized for the first time. More importantly, this work is focused on the understanding of how substitutions on the A- or X- site influence material properties. Some of the salient features of this work are:

(i) The existence of solid solubility in Ti-Si-Ge-C, Ti-Si-Al-C and in Ti-Al-C-N systems is established.

(ii) Substitution on the A-site, i.e. replacing Si by Ge or Al in general decreases the stiffness, thereby increasing the TEC in the system, with the exception of Ti_3GeC_2. This fact is well supported by the decrease in bulk, Young's and shear moduli for the solid solution compositions. Substitution on the X-sites on the other hand lowers the TEC and increases the shear and Young's moduli for the solid solution compositions indicating a solid solution hardening.

(iii) The solid solution softening effect mentioned above for A-site substitutions is further validated by a lower value of the Vickers microhardness values for the solid solution compositions than that of Ti_3SiC_2. The high temperature strengths under compression were also observed to decrease for the A-site substituted solid solutions. On the other hand,-the Vickers microhardness values of the X-site substituted

solid solutions was observed to be significantly higher than those of the end members. The high temperature compressive strength was also found to go up as well.

(iv) The residual resistivity ratio (RRR) of both A- and X-site substituted solid solution compositions were observed to be lower than the corresponding end members, which is indicative of solid solution scattering. This fact is further supported for the A-site substituted solid solutions, where a reduction in the phonon conductivity is also observed. The thermal and corresponding phonon conductivity for the X-site substituted solid solutions, on the other hand, were observed to be higher than the corresponding end members indicating considerable phonon contribution to entropy transport. A correlation between the shear moduli and phonon conductivity was also found in this case, indicating that the phonon conductivity is influenced by stiffness.

(v) The Seebeck coefficients of the A-site substituted solid solutions were observed to be low for a wide range of temperature (25-300 K) like the end members. This fact, combined with the weak dependence of Hall coefficients with temperature led to the conclusion that a two band model is necessary for analyzing the transport properties of the A site substituted solid solutions. Substitution on the X-sites on the other hand, increased the carrier concentration, with holes as the dominant carrier. High value of Seebeck and Hall coefficient suggests that a single band model is sufficient for analyzing the transport properties in this case.

(vi) Substitution on the X-site influenced the formation of incipient kink bands (IKBs) under compression, significantly. The threshold stress (σ_c), critical resolved shear stress (Ω/b) were observed to increase considerably, followed by a lowering of the parameter *w* by a factor of two and thereby decreasing the dislocation width.

8.2 Future Work

Based on the current results it is fair to conclude that substitution in the A- or X-sites in the MAX family influences their properties. However, it is too early to make a general statement about the effects of these substitutions as this awaits further works. In order to have a better understanding in this arena the following issues could be addresses in near future:

(i) To date, all the work on MAX solid solution indicates that hardening is only operative when substitution are on the X-sites. Before generalizing this statement more work is needed on different MAX systems. At this stage, it is not a bad idea to try to study the influence of all the three (Al, Ge, Si) A group elements in the 312 system.

(ii) Substitution on the X-sites in general improves the high temperature properties and increases the hardness. To date the compositions explored are $Ti_2Al(C_{0.5},N_{0.5})$ and $Ti_3Al(C_{0.5},N_{0.5})_2$. The ratio of C:N in each case is 0.5. To have a better understanding it is advisable to vary the C/N ratio and see the influence on material properties in the system.

(iii) The reason behind the dramatic increase in Q^{-1} beyond a certain temperature for all the MAX compositions studied to date, still remains elusive. Even though this work reports on the damping behavior of A-site substituted solid solutions derived from RUS analysis, to date, no work exists on the damping properties of the X-site substituted solid solutions.

(iv) It is encouraging to see the influence of X-site substitutions on the formation of IKBs. Since the X-site substituted solid solutions in general are harder and stiffer than the end members, it is fair to assume that the shear moduli are playing a role in increasing the threshold stress (σ_c) required for an average grain to kink. It would be useful to study the kinking behavior when it is decoupled from hardening. In other words, the kinking behavior of the A-site substituted solid solutions and compared to those with the end members will give a much better picture of the influence of solid solutions on kinking behavior.

List of References

1. Barsoum M.W, "The $M_{N+1}AX_N$ phases: A new class of solids: Thermodynamically stable nanolaminates", Prog. Solid State Chem., **28** (2000) 201-81.

2. Jeitschko W and Nowotny H, "Die Kristallstructur von Ti_3SiC_2-Ein Neuer Komplxcarbid Typ", Monatsh Chem., **98** (1967) 329-337.

3. Barsoum M.W and El-Raghy T, "Synthesis and characterization of remarkable ceramic: Ti_3SiC_2", J. Am. Cer. Soc., **79** (1996) 1953-1956.

4. Pampuch R., Lis J, Stobierski L, Tymkiewicz M, "Solid Combustion Synthesis of Ti_3SiC_2", J. Eur. Cer. Soc., **5** (1989) 283-291.

5. Du Y, Schuster J.C, Seifert H, Aldinger F, "Experimental Investigation and Thermodynamic Calculation of the Titanium-Silicon-Carbon System", J. Am. Cer. Soc., **83** (2000) 197-203.

6. Gilbert C.J, Bloyer D.R, Barsoum M.W, El. Raghy T, Tomsia A.P, Ritchie R.O, "Fatigue-Crack Grwoth and Fracture Properties of Coarse and Fine-Grained Ti_3SiC_2", Scripta Mater., **42** (2000) 761-767.

7. El. Raghy T, Barsoum M.W, Zavaliangos A, Kalidindi S.R, "Processing and Mechanical Properties of Ti_3SiC_2, Part II: Effect of Grain Size on Deformation Temperature", J. Am. Ceram. Soc., **82** (1999) 2855-2860.

8. Barsoum M.W, Yoo H.-I, Polushina I.K, Rud V. Yu, Rud V. Yu, El- Raghy T, "Electrical Conductivity, Thermopower and Hall Effect of Ti_3AlC_2, Ti_4AlN_3 and Ti_3SiC_2", Phys. Rev. B., **62** (2000) 10194-10199.

9. Pietzka M.A and Schuster J.C, "Summary of Constitution Data of the System Al-C-Ti", J. Phase Equilib. **15** (1994) 392.

10. Pietzka M.A and Schuster J.C, Concerted Action on Materials Science, in: Leuven, Proceedings, Part A, Commission of the European Communities, Brussels, Belgium, 1992.

11. Tzenov N, Barsoum M.W, "Synthesis and Characterization of Ti_3AlC_2", J. Am. Cer. Soc., **83** (2000) 825-832.

12. Wang X.H and Zhou Y.C., "Microstructures and Properties of Ti_3AlC_2 prepared by the Solid-Liquid Reaction Synthesis and Simultaneous in situ Hot Pressing Process", Acta Materialia., **50** (2002) 3141-3149.

13. Wolfsgruber H, Nowotny H and Benesovsky F, "Die Kristallstuktur von Ti_3GeC_2", Monatash. Chem., **98** (1967) 2401.

14. Barsoum M.W and El. Raghy T, "A progress report on Ti_3SiC_2, Ti_3GeC_2 and H-phases, M_2AX", J. Mater. Synth. Process., **5** (1997) 197-216.

15. Barsoum M.W, Brodkin D and El-Raghy T, "Layered Machinable Ceramics for High Temperature Applications", Scripta Mater., **36** (1997) 535-541.

16. Wang J.Y and Zhou Y.C, "First-Principles Study of Equilibrium Properties and Electronic Structure of $Ti_3Si_{0.75}Al_{0.25}C_2$ Solid Solution", J. Phys. Condens. Matter., **15** (2003) 5959-5968.

17. Zhou Y.C, Zhang HB, Liu MY, Wang JY, Bao YW, "Preparation of TiC free Ti_3SiC_2 with Improved Oxidation Resistance by Substitution of Si with Al", Mater Res. Innov., **8** (2004) 97-102.

18. Zhou Y. C, Chen J.X and Wang J.Y, "Strengthening of Ti_3AlC_2 by incorporation of Si to form $Ti_3Al_{1-x}Si_xC_2$ Solid Solutions", Acta Materialia, in press.

19. Jeitschko W, Nowotny H and Benesovsky F, "Kohlenstoffhaltige Ternare Verbindungen (H-Phase) ", Monatsh Chem., **94** (1963) 672.

20. Jeitschko W, Nowotny H and Benesovsky F, "Ti_2AlN eine Stickstoffhaltige H-Phase", Monatsh Chem., **94** (1963) 1198.

21. Barsoum M.W, Brodkin D and El-Raghy T, "Layered Machinable Ceramics for High Temperature Applications", Scripta Met. Mater., **36** (1997) 535-41.

22. Barsoum M.W, Ali M and El-Raghy T, "Processing and Characterization of Ti_2AlC, Ti_2AlN and $Ti_2Al(C_{0.5},N_{0.5})$ ", Met. Mater. Trans., **31 A** (2000) 1857.

23. Pietzka M.A and Schuster J.C, "Phase Equilibria in the Quaternary System Ti-Al-C-N", J. Am. Cer. Soc., **79** (1996) 2321.

24. Barsoum M.W, Farber L, Levin I, Procopio A.T, El-Raghy T and A. Burner, "HRTEM of Ti_4AlN_3; or $Ti_3Al_2N_2$ Revisited", J. Am. Cer. Soc., **82** (1999) 2545-2547.

25. Procopio A.T, El. Raghy T and Barsoum M.W, "Synthesis of Ti_4AlN_3 and Phase Equilibria in the Ti-Al-N System", Metal Materials. Trans. **31 A** (2000) 373-378.

26. Rawn C.J, Barsoum M.W, El-Raghy T, Procopio A.T, Hoffman C.M and Hubbard C, "Structure of Ti_4AlN_{3-x} – a Layered $M_{n+1}AX_n$ Nitride", Mater. Res. Bull., **35** (2000) 1785-1796.

27. Ganguly A, Zhen T and Barsoum M.W, "Synthesis and Mechanical Properties of Ti_3GeC_2 and $Ti_3(Si_xGe_{1-x})C_2$ (x = 0.5,0.75) Solid Solutions", J. of Alloys and Compds., **376** (2004) 287-295.

28. Radovic M, Barsoum M.W, Ganguly A, Zhen T, Finkel P, Kalidindi S.R and Lara-Curzio E, "On the Elastic Properties and Mechanical Damping of Ti_3SiC_2, Ti_3GeC_2, $Ti_3Si_{0.5}Al_{0.5}C_2$ and Ti_2AlC in the 300-1573 K Temperature Range", Acta Materialia (MS Accepted).

29. Manoun B, Saxena S.K, Hug G, Ganguly A and Barsoum M.W, "Synthesis and compressibility of $Ti_3(Al,Sn)C_2$ and $Ti_3Al(C_{0.5}N_{0.5})_2$" Phys. Rev. B.,(MS submitted).

30. ASTM E 112, American Society of Testing and Materials, West Conshohocken, PA.

31. El-Raghy T and Barsoum M.W, "Processing and Mechanical Properties of Ti_3SiC_2: Part I: Reaction Path and Microstructure Evolution", J. Am. Cer. Soc., **82** (1999) 2849-2854.

32. Nowotny H, "Struktuchemie Einiger Verbindungen der Ubergangsmetalle mit den elementen C, Si, Ge, Sn", Prog. Solid State Chem., H. Reiss Ed., **2** (1970) 27.

33. Wu E, Wang J, Zhang H, Zhou Y, Sun K and Xue Y, "Neutron Diffraction Studies of $Ti_3Si_{0.9}Al_{0.1}C_2$ Compounds", Mater. Lett., (2005).

34. Holm B, Ahuja R, Li S, Johansson B, J. Appl. Phys., **91** (2002) 9874.

35. Barsoum M.W and El-Raghy T, “Room Temperature Ductile Carbides”, Met. Mater. Trans., **30A** (1999) 363-369.

36. Barsoum M.W, Farber L, and El-Raghy T, “Dislocations, Kink Bands and Room Temperature Plasticity of Ti_3SiC_2”, Met. Mater. Trans., **30 A** (1999) 1727-1738.

37. Onodera A, Hirano H, Yuasa T, Gao N.F and Miyamoto Y, “Static Compression of Ti_3SiC_2 to 61 GPa”, Appl. Phys. Lett., **74** (1999) 3782.

38. Birch F, J. Geophys. Res., **83** (1978) 1257.

39. Drikamer H.G, Lynch R.W, Clendenen R.L and Perez- Alubuerne E.A, in Solid State Physics Vol. 19, edited by F. Seitz and D. Turnbull (Academic, New York, 1996), 135.

40. Chang R and Graham L.J, J. Appl. Phys., **37** (1966) 3778.

41. Jhi S. Hoon and Ihm J, “Electronic Structure and Structural Stability of TiC_xN_{1-x} alloys”, Phys. Rev. B., **56** (1997) 13826-13829.

42. Pampuch R, Lis J, Piekarczyk J and Stobierski L, “Ti_3SiC_2 –Based Materials Produced by Self-Propagating High Temperature Synthesis (SHS) and Ceramic Processing”, J. Mater. Synth. Process., **1** (1993) 93.

43. Finkel P, Barsoum M.W, and El. Raghy T, “Low Temperature Dependencies of the Elastic Properties of Ti_4AlN_3, $Ti_3Al_{1.1}C_{1.8}$ and Ti_3SiC_2”, J. Appl. Phys., **87** (2000) 1701.

44. Manoun B, Saxena S.K, Liermann H.P, Gulve R.P, Hoffman E, Barsoum M.W, Hug G and Zha C.S, Appl. Phys. Lett., **85** (2004) 1514.

45. Manoun B, Saxena S.K and Barsoum M.W, “High Pressure Study of Ti_4AlN_3 to 55 GPa”, Appl. Phys. Lett., **86** (2005) 101906.

46. Christensen A.N, Gerward L, Olsen J.S and Steenstrup S, Acta Chem. Scand., **40** (1990) 752.

47. Kim J.O, Achenbach J.D, Mirkarimi P.B, Shinn M and Barnett S.A, J. Appl. Phys., **72** (1992) 1805.

48. Wang Z, Zha S and Barsoum M.W, "Compressibility and Pressure induced Phase Transformation in Ti_3GeC_2," Appl. Phys. Lett., **85** (2004) 3453-3455.

49. Manoun B, Yang H, Gulve R.P, Saxena S.K, Ganguly A, Barsoum M.W, Liu Z and Zha C.S, "Infra red Spectrum and Compressibility of Ti_3GeC_2 to above 51 GPa" (MS Submitted).

50. Manoun B, Liermann H.P, Gulve R.P, Saxena S.K, Ganguly A, Barsoum M.W and Zha C.S, "Compression of $Ti_3Ge_{0.5}Si_{0.5}C_2$ to 53 GPa", Appl. Phys. Lett., **84** (2004) 2799-2801.

51. Greene R.G, Luo H and Ruoff A.L, Phys. Rev. Lett. **73** (1994) 2075.

52. Finkel P, Seaman B, Harrell K, Palma J, Hettinger J.D, Lofland S, Ganguly A, Barsoum M.W, Sun Z, Li Sand Ahuja R, "Electronic, Thermal and Elastic Properties of $Ti_3Si_{(1-x)}Ge_xC_2$ Solid Solutions", Phys. Rev. B, **70** (2004) 0851041-0851046.

53. Wang J.Y and Zhou Y. C., "Polymorphism of Ti_3SiC_2 ceramic: First-Principles Investigations", Phys. Rev. B, **69** (2004) 144108.

54. Barsoum M.W, El-Raghy T, Rawn C.J, Porter W.D, Wang H, Payzant A and Hubbard C, "Thermal Properties of Ti_3SiC_2", J. Phys. Chem. Solids., **60** (1999) 429-439.

55. Manoun B, Saxena S.K, Liermann H.P and Barsoum M.W "Thermal Expansion of Polycrystalline Ti_3SiC_2 in the 25 º-1400 ºC", J. Am. Ceram. Soc., **88** (2005) 3489-3491.

56. Zhou Y, Sun Z, Wang X and Chen S, J. Phys. Condens. Matter., **13** (2001) 10001.

57. Manoun B, Zhang F.X, Saxena S.K, Barsoum M.W and El. Raghy T "X-ray High Pressure Study of Ti_2AlN and Ti_2AlC" (MS Submitted).

58. Wang Q, Lengauer W, Koch T, Scheerer M, Smid I, "Hardness and Elastic Properties of $Ti(C_xN_{1-x})$, $Zr(C_xN_{1-x})$ and $Hf(C_xN_{1-x})$ ", J. of Alloys and Compds., **309** (2000) L5-L9.

59. Finkel P, Barsoum M.W and El. Raghy T, "Low Temperature Dependence of the Elastic Properties of Ti_3SiC_2", J. Appl. Phys., **85** (1999) 7123-7126.

60. Procopio A.T, Barsoum M.W and El. Raghy T, "Characterization of Ti_4AlN_3", Metal Materials. Trans. **31 A** (2000) 333-337.

61. Fisher E.S, D. Dever, "The Science and Technology and Applications of Titanium", edited by Jaffe R.I and Promise N.E (Pergamon, Oxford, 1968).

62. Gilman J.J, Roberts B.W, J. Appl. Phys., **32** (1961) 1405.

63. Barsoum M.W, Radovic M, Zhen T, Finkel P and Kalidindi S.R, "Dynamic Elastic Hysteretic Solids and Dislocations", Phys. Rev. Lett., **94** (2005) 085501-1.

64. Migliori A and Sarrao J.L, "Resonant Ultrasound Spectroscopy: Applications to Physics, Materials Measurements and Nondestructive Evaluation", John Wiley and Sons, New York (1997).

65. Migliori A, Sarrao J.L, Visscher W.M, Bell T.M, Lei M et al., "Resonant Ultrasound Spectroscopic Techniques for Measurements of the Elastic Moduli of Solids", Physica B, **183** (1993) 1-24.

66. Radovic M, Lara-Curzio E and Reiser L, "Comparison of Different Experimental Techniques for Determination of Elastic Properties of Solids", Mater. Sci. Eng., **368** (2004) 56-70.

67. Leisure R.G and Willis F.A, "Resonant Ultrasound Spectroscopy", J. Phys. Condens. Matter., **9** (1997) 601.

68. Alers G, in Physical Accoustics, edited by Mason W, Academic, New York III (1965) B.

69. Blackman M, in Handbuch der Physik, edited by Flugge S, Springer, Berlin (1955).

70. Dodd S.D, Cankurtaran M, James B, "Ultrasonic Determination of the Elastic Nonlinear Acoustic Properties of Transition Metal-Carbide Ceramics: TiC and TaC", J. Mater. Sci., **38** (2003) 1107.

71. Hannink R.H.J and Murray M.J, "Elastic Moduli Measurements of Some Cubic Transition Metal Carbides and Alloyed Carbides", J. Mater. Sci., **9** (1974) 223.

72. Finkel P, Hettinger J.D, Lofland S, El-Raghy T and Barsoum M.W, Unpublished Results.

73. Barsoum M.W, Rawn C.J, El-Raghy T, Procopio A.T, Porter W.D, Wang H and Hubbard C.R, "Thermal Properties of Ti_4AlN_3", J. Appl. Phys., **87** (2000) 8407-8414.

74. Pierson H, *Handbook of Refractory Carbides and Nitrides*, Noyes Publications, Westwood, NJ. 1996.

75. Neckel A, "Electronic Structure of Stoichiometric and Non-Stoichiometric TiC and TiN", in *The Physics of Carbides and Nitrides and Borides*, R. Freer Ed., Kluwer Academic Press, Amsterdam, 485 (1990).

76. Yoo H.-I, Barsoum M.W and El-Raghy T, "Ti_3SiC_2 Has Negligible Thermopower" Nature, **407** (2000) 581.

77. Finkel P, Hettinger J.D, Lofland S.E, Barsoum M.W and El-Raghy T, "Magnetotransport Properties of Ternary Carbides Ti_3SiC_2: Hall Effect, Magnetoresistance and Magnetic Susceptibility", Phys. Rev. B., **65** (2002) 035113.

78. Finkel P, Barsoum M.W, Hettinger J.D, Lofland S.E and Yoo H.-I, "Low Temperature Transport Properties of Nanolaminates Ti_3AlC_2 and Ti_4AlN_3", Phys. Rev. B., **67** (2003) 235108.

79. Hettinger J.D, Lofland S.E, Finkel P, Meehan T, Palma J, Harrell K, Gupta S, Ganguly A, El-Raghy T and Barsoum M.W, "Electrical Transport, Thermal Transport and Elastic Properties of M_2AlC (M=Ti, Cr, Nb and V) ", Phys. Rev. B., **72** (2005) 115120.

80. Ashcroft N.W und Mermin N.D, Solid State Physics, WB Sounders and Co. (1976).

81. Ho J.C, Hamdeh H.H and Barsoum M.W, J. Appl. Phys., **86** (1999) 3609.

82. Lofland S.E, Hettinger J.D, Harrell K, Finkel P, Gupta S, Barsoum M.W and Hug G, "Elastic and Electronic Properties of Select M_2AX Phases", Appl. Phys. Lett., **84** (2004) 508.

83. Tournaire R and Sierro J, C. R. Serie B (Sci. Phys.), **281** (1975) 317.

84. ASTM C1161-94, American Society of Testing and Materials, West Conshohocken, PA.

85. Salama I, El-Raghy T, Barsoum M.W, "Synthesis and Mechanical Properties of Nb_2AlC and $(Ti,Nb)_2AlC$", J. of Alloys and Compds., **347** (2002) 271-278.

86. El-Raghy T, Zavaliangos A, Barsoum M.W and Kalidindi S.R, "Damage Mechanisms around Hardness Indentation in Ti_3SiC_2", J. Am. Ceram. Soc., **80** (1997) 513-516.

87. Barsoum M.W, Zhen T, Kalidindi S.R, Radovic M and Murugaiah A, "Fully Reversible, Dislocation-based Compressive Deformation of Ti_3SiC_2 to 1 GPa", Nat. Mater. **2** (2003) 107-111.

88. Radovic M, Barsoum M.W, El-Raghy T, Wiederhorn S, Luecke W, "Effect of Temperature, Strain Rate and Grain Size on the Mechanical Response of Ti_3SiC_2 in Tension ", Acta Mater., **50** (2002) 1297-1306.

89. Radhakrishnan M.R, Williams J.J, Akinc M, "Synthesis and Stability of Ti_3SiC_2", J. of Alloys and Compds., **285** (1999) 85-88.

90. Barsoum MW, Zhen T, Zhou A, Basu S, Kalidindi S.R, "Microscale Modeling of Kinking Nonlinear Elastic Solids", Phys. Rev. B., **71** (2005) 134101.

91. Murugaiah A, Barsoum MW, Kalidindi SR, Zhen T. "Spherical Nanoindentations and Kink Bands in Ti_3SiC_2", J. Mater. Res., **19** (2004) 1139.

92. Barsoum MW, Murugaiah A, Kalidindi SR, Zhen T, Gogotsi Y, "Kink Bands, Nonlinear Elasticity and Nanoindentations in Graphite", Carbon, **42** (2004) 1435.

93. Barsoum MW, Murugaiah A, Kalidindi SR, Zhen T, "Kinking Nonlinear Elastic Solids, Nanoindentations, and Geology", Phys. Rev. Lett., **92** (2004) 255508.

94. Zhou A.G, Barsoum M.W, Basu S, Kalidindi S.R and El-Raghy T, "Incipient and Regular Kink Bands in Fully Dense and 10 vol. % Porous Ti_2AlC", Acta Materialia (MS Accepted).

95. Orowan E, "A type of plastic deformation new in metals", Nature **149** (1942) 643.

96. Farber L, Levin I and Barsoum M.W, "HRTEM Study of a Low- Angle Boundary in Plastically Deformed Ti_3SiC_2", Phil. Mag. Letters., **79** (1999) 4103-4112.

97. Farber L, Barsoum M.W, Zavaliangos A and El-Raghy T, "Dislocations and Stacking Faults in Ti_3SiC_2", J. Am. Ceram. Soc., **84** (1998) 1677-1681.

98. Frank FC, Stroh AN, "On the Theory of Kinking", Proc. Phys. Soc., **65** (1952) 811.

99. Barsoum M.W and Radovic M, "Mechanical Properties of the MAX phases", Encyclopedia of Materials Science and Technology, Eds. Buschow, Cahn, Fleming, Kramer, Mahajan Veyssiere, Elsevier Science (2004).

100. Guyer R.A, Tencate J and Johnson P, "Hysteresis and Dynamic Elasticity of Consolidated Granular Materials", Phys. Rev. Lett., **82** (1999) 3280.

101. Scalerandi M, Agostina V, Delsanto P.P, Van Den Abeele K and Johnson P.A, "Local Interaction Simulation Approach to Modeling Non-Classical, Nonlinear Elastic Behavior in Solids", J. Acoust. Soc. Am., **113** (2003).

102. Guyer R.A and Johnson P, "Nonlinear Mesoscopic Elasticity: Evidence for a New Class of Materials", Physics Today 30 (1999).

103. Schaller R, Fentozzi G and Gremaud G, Mechanical Spectroscopy Q^{-1} 2001 with Applications to Materials Science, Eds Trans Tech Pubs., Zurich (2001).

104. El-Raghy T and Barsoum M.W, "Diffusion Kinetics of the Carburization and Silicidation of Ti_3SiC_2", J. Appl. Phys., **83** (1998) 112-119.

105. Barsoum M.W, El-Raghy T, Farber L, Amer M, Christini R and Adams A, "The Topotaxial Transformation of Ti_3SiC_2 To Form a Partially Ordered Cubic $TiC_{0.67}$ Phase by the Diffusion of Si into Molten Cryolite", J. Electrochem. Soc., **146** (1999) 3919-3923.

106. El-Raghy T, Barsoum M.W and Sika M, "Reaction of Al with Ti_3SiC_2 in the 800-1000 ºC Temperature Range", Mater. Sci. Eng. A., **298** (2001) 174-178.

107. Barsoum M.W, Golczewski J, Seifert H and Aldinger F, "Fabrication, Electric and Thermal Properties of Ti_2InC, Hf_2InC and $(Ti,Hf)_2InC$", J. Alloys and Compds., **340** (2002) 173-179.

108. Shewmon P.G, Diffusion in Solids, McGraw-Hill Comp. 1963.

109. El-Raghy T and Barsoum M.W, J. Appl. Phys., **83** (1998) 112.

110. Cockeram B and Rapp R, Metal. Mater. Trans. A., **26** (1995) 777.

111. Hung L.S, Gyulai J, Mayer J.W, Lau S.S and Nicolet M.A, J. Appl. Phys., **54** (1980) 5076.

112. Revesz P, Gyimesi J, Pogany L and Peto G, J. Appl. Phys., **54** (1983) 2114.

Appendix A: Interdiffusion between Ti_3SiC_2-Ti_3GeC_2 and Ti_2AlC-Nb_2AlC diffusion couples.

A.1 Abstract

This work reports on the interdiffusion of Ge and Si in Ti_3SiC_2 and Ti_3GeC_2, as well as that of Nb and Ti in Ti_2AlC and Nb_2AlC. The inter-diffusion coefficient, D_{int}, measured by analyzing the diffusion profiles of Si and Ge obtained when Ti_3SiC_2-Ti_3GeC_2 diffusion couples are annealed in the 1473 to 1773 K temperature range at the Matano interface composition ($\approx Ti_3Ge_{0.5}Si_{0.5}C_2$) was found to be given by:

$$D_{int}\ (m^2s^{-1}) = (0.3\pm0.2)\ \exp -\ 350\pm3\ (kJ/mol)/RT$$

D_{int} increased with increasing Ge composition. At the highest temperatures, diffusion was halted after a short time, apparently by the formation of a diffusion barrier of TiC. Similarly the interdiffusion of Ti and Nb in Ti_2AlC-Nb_2AlC couples were measured in the 1723 to 1873 K temperature range. D_{int} for the Ti_2AlC-Nb_2AlC diffusion couples, at the Matano interface composition ($\approx (Ti_{0.5},Nb_{0.5})_2AlC$) was found to be given by:

$$D_{int}\ (m^2s^{-1}) = (12\pm3)\times10^3\ \exp -\ 591\pm5\ (kJ/mol)/RT$$

At 1773 K the diffusivity of the transition metal atoms were ≈ 7 times smaller than those of the Si and Ge atoms, suggesting the former are better bound in the structure than the latter.

A.2 Introduction

The unusual combination of properties of the MAX phases in general, and Ti_3SiC_2 and Ti_2AlC in particular, suggest they are potential candidates a number of

applications such as hot pressing tools, dies, heating elements, substitutes for superalloys in the chemical and petrochemical industry, automotive and possibly even aerospace. Before widespread applications are possible it is imperative to better understand the diffusion in these solids for a number of reasons. The first is practical since it would help diffusion bond these solids to each other and to other solids. Knowledge of the diffusion coefficients is also important when analyzing creep and/or sintering results. From a scientific point of view knowing the diffusivity of various atoms in a compound can enhance our understanding of its bonding characteristics.

The purpose of this paper is to report, for the first time, on the interdiffusion of Ge and Si in Ti_3SiC_2 and Ti_3GeC_2, as well as that of Nb and Ti in Ti_2AlC and Nb_2AlC. This was accomplished by setting up Ti_3SiC_2/Ti_3GeC_2 and Ti_2AlC/Nb_2AlC diffusion couples. For brevity's sake, the former couple will henceforth be referred to as the 312 couple; the latter as the 211 couple.

A.3 Experimental Details

Square, roughly 5 mm thick samples were electro-discharge machined. The ≈ 10 x 10 mm^2 surfaces to be diffusion bonded were mechanically polished down to 1 μm alumina and stacked on a graphite block, with a Ti_3GeC_2 sample sandwiched in between two polished Ti_3SiC_2 samples in the 312 couple. For the 211 couple a Nb_2AlC sample sandwiched in between two polished Ti_2AlC samples. Both sides of the Ti_3GeC_2 and Nb_2AlC samples were polished. The whole assembly was placed in a vacuum hot press and a graphite block – weighing ≈ 20 kg, used to enhance the diffusional bond - was carefully balanced on the stack. The hot press was heated - at a

rate of ≈ 773 K/hr - using graphite elements, under vacuum (10^{-2} torr) up to the desired temperature, and held for the desired soaking period before furnace cooling at a rate of ≈ 773 K/hr.

The bonded samples were cross-sectioned using a diamond wheel, mounted and polished down to 1 μm for microstructural characterization. Microanalysis was performed with a FESEM, (XL-30, FEI-Philips, Hillsboro, OR) equipped with an energy dispersive spectroscope, EDS (Edax Inc., Mahwah, NJ). Most measurements were carried out using an accelerating voltage of 30 KV.

The concentration, c vs. distance, x, profiles, obtained from the microanalysis were fit to determine the Matano interface and to calculate the interdiffusion coefficient, D_{int}, at the Matano interface and elsewhere assuming [108]:

$$D_{\text{int}}(c') = \frac{1}{2t}\frac{dx}{dc}\bigg|_{c=c'} \int_{c=0}^{c=c'} x\, dc \qquad \text{(A.1)}$$

The values of D_{int} were calculated from the Si, Ge, Ti and Nb concentration profiles. Note the sandwich configuration resulted in two interfaces for each anneal. At 1473 and 1573 K in the 312 couple, however, one side did not bond and so only one interface was analyzed. The error bars shown represent the average and standard deviations for the two interfaces and calculations of D_{int} from the Si and Ge profiles in the 312 system and the Ti and Nb profiles in the 211 system.

A.4 Results and Discussions

A.4.1 Ti_3SiC_2-Ti_3GeC_2 Couple:

Typical Si and Ge concentration profiles in the 312 couple that developed after 2 h and 8 h anneal at 1673 K are shown in Fig. A.1. The values are given as the atomic fractions of the A and B metals neglecting the carbon concentration which could not be measured accurately at the 30keV beam energy used. The Matano interface for the 8 h run is marked by vertical dashed lines. The other profiles were displaced to bring all the Matano interfaces to the same position.

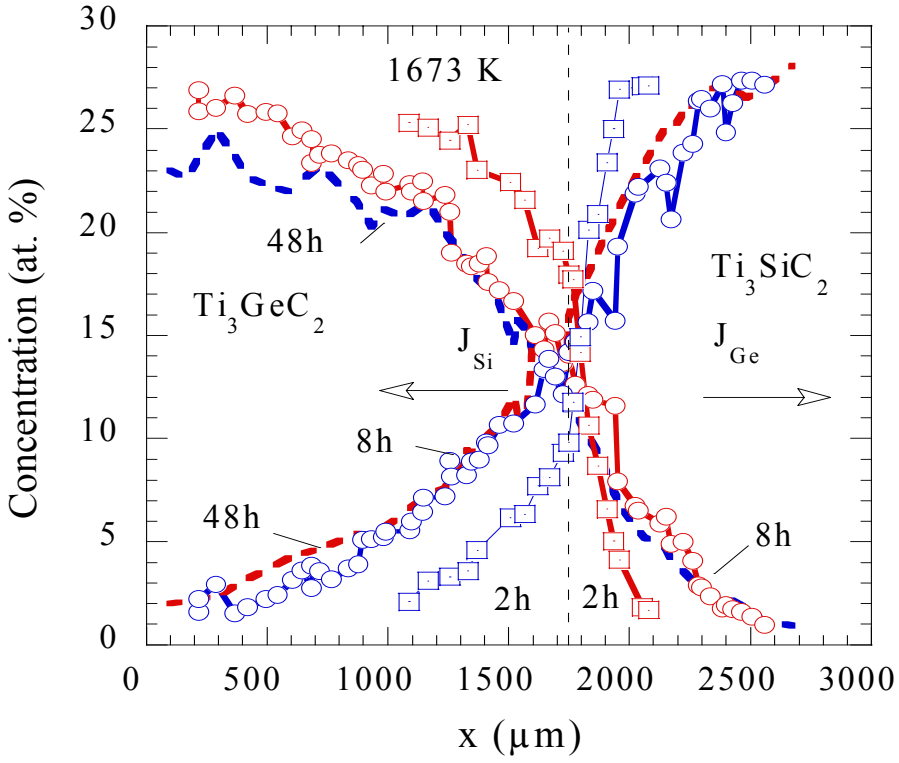

Figure A.1: Si (blue) and Ge (red) concentration profiles obtained after annealing at 1673 K for 2h, 8h and 48 h.

From the profile asymmetry, it is evident that in this system, D_{int}, is higher when the Si concentration is low, and vice versa. This observation is confirmed in Fig. A.2, which shows a semi-log plot of D_{int} as a function of $x'_{Si}/(x'_{Ge}+x'_{Si})$, where x_i is the molar concentrations of Si or Ge on the A atom lattice. In other words, $x'_{Si} + x'_{Ge} = 1$.

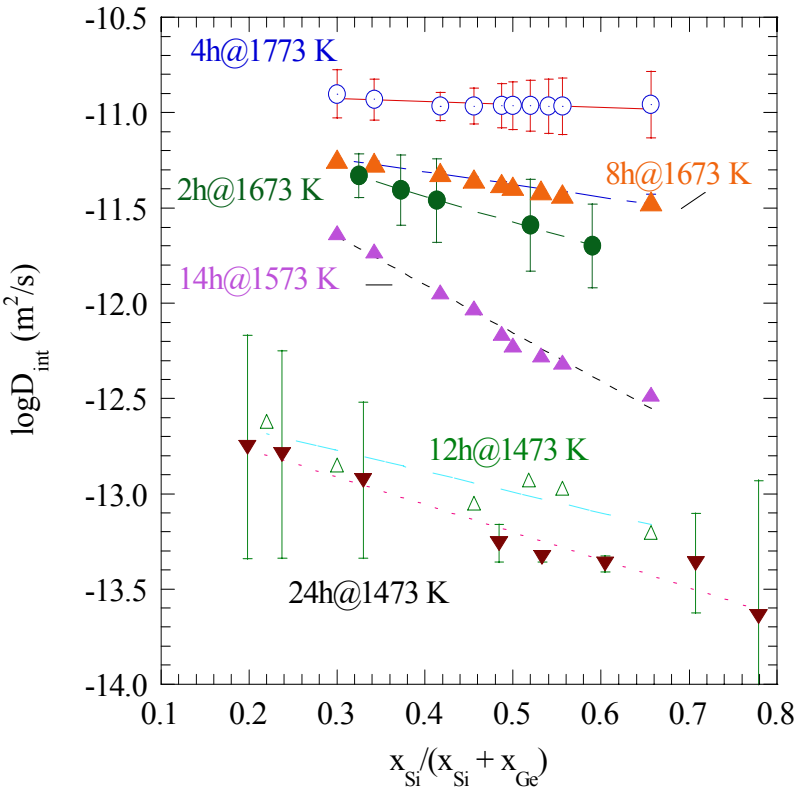

Figure A.2: Dependence of D_{int} on $x_{Si}/(x_{Si} + x_{Ge})$ in the 1473–1773 K temperature range. As defined here x_i is not the molar concentration of i in the ternary, but rather the molar concentration of Si or Ge in the basal planes. i.e. $x_{Si} + x_{Ge} = 1$

Table A.1 lists the interdiffusion coefficients measured at the Matano interface. At the Matano interface, the concentrations of Ti, Si and Ge in mol. %, - using the composition plots determined by EDS - were 72±1, 13±1 and 14.5±1, respectively. (Note that in determining the compositions, the EDS system was ignoring the C content in the ternary).

Table A.1 The time/temperature range and the corresponding values of the diffusion coefficients at the Matano interface for the 312 system.

Temp. (K)	Time (h)	log D_{int} (m^2/s) (at B-M)
1773	4	-11.0±0.12
1673	8	-11.4±0.1
1673	2	-11.7±0.2
1573	14	-12.0±0.02
1473	12	-12.9±0.2
1473	24	- 13.3±0.1

Surprisingly, the c vs. x profiles obtained after annealing for 48 h, at 1673 K (shown as dashed lines labeled 48 h in Fig. 8.1) were almost identical to the ones measured after an 8 h anneal at the same temperature. The reason for this state of affairs - also observed at 1773 K for 16 h - is not clear. Figure A.3 shows etched OM micrographs of the interface after annealing at 1673 K for 48 h. The white phase is TiC_x that results from the decomposition of Ti_3GeC_2 by the loss of Ge. Why the decomposition should result in a cessation of diffusion in unclear, but encapsulation of each grain in a TiC outer shell through which the Si and Ge atoms could not

diffuse - that is the formation of a diffusion barrier layer - is a possibility. It is clear that more work will be needed to understand this intriguing phenomenon.

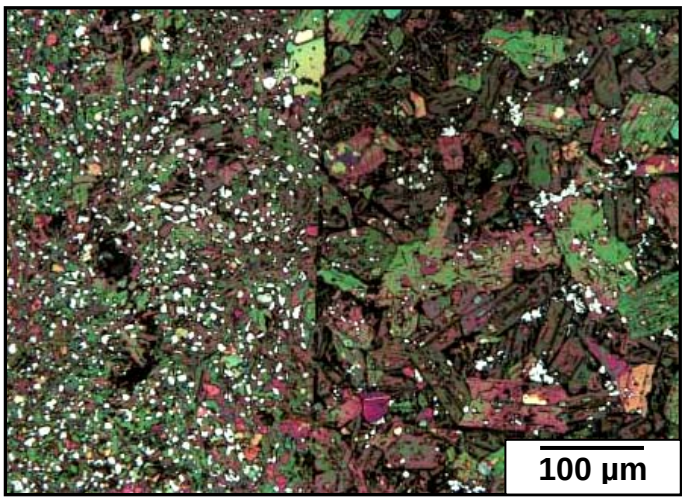

Figure A.3: Etched OM micrograph of a Ti_3SiC_2-Ti_3GeC_2 diffusion couple annealed at 1673 K for 48 h. The white phase on the left is TiC_x that forms as a result of Ge loss from Ti_3GeC_2. The left half of the couple is Ti_3GeC_2. Once the decomposition is observed the concentration profiles stop evolving.

A.4.2 Ti_2AlC-Nb_2AlC Couple:

The Ti and Nb concentration profiles in the 211 system, after 6 h, 18 h and 36 h anneal at 1773 K are shown in Fig. A.4. The Matano interface for the 6 h run is depicted by a vertical dashed line. The curves are displaced to coincide at the Matano interface.

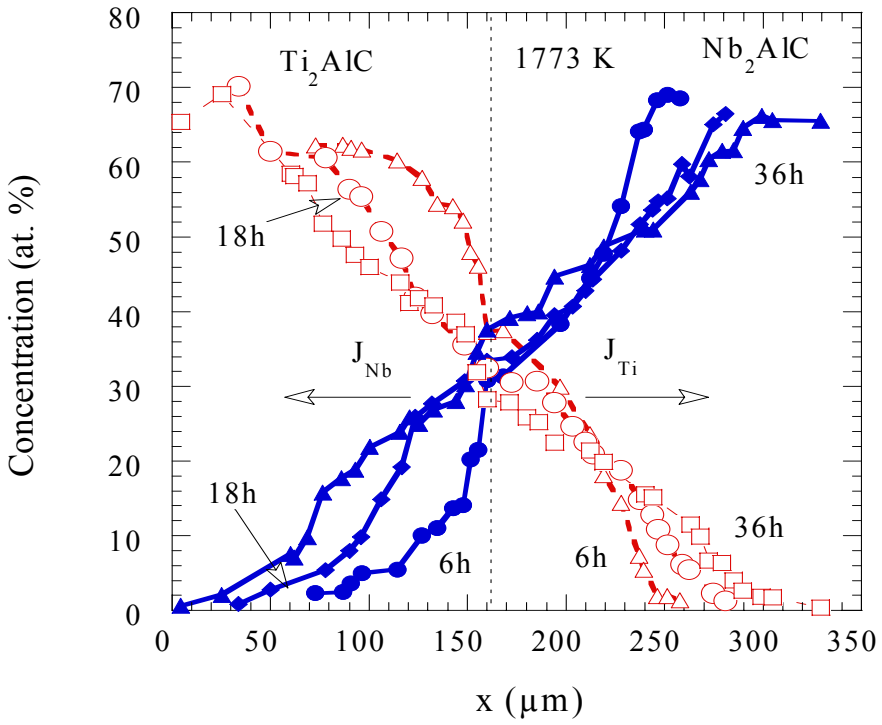

Figure A.4: Nb (blue) and Ti (red) concentration profiles obtained after annealing at 1773 K for 6h, 18h and 36 h

In this system, a weaker composition dependence of D_{int}, - here a function of $x'_{Ti}/(x'_{Ti} + x'_{Nb})$ - was observed (Fig. A.5). Here again $x'_{Ti} + x'_{Nb} = 1$.

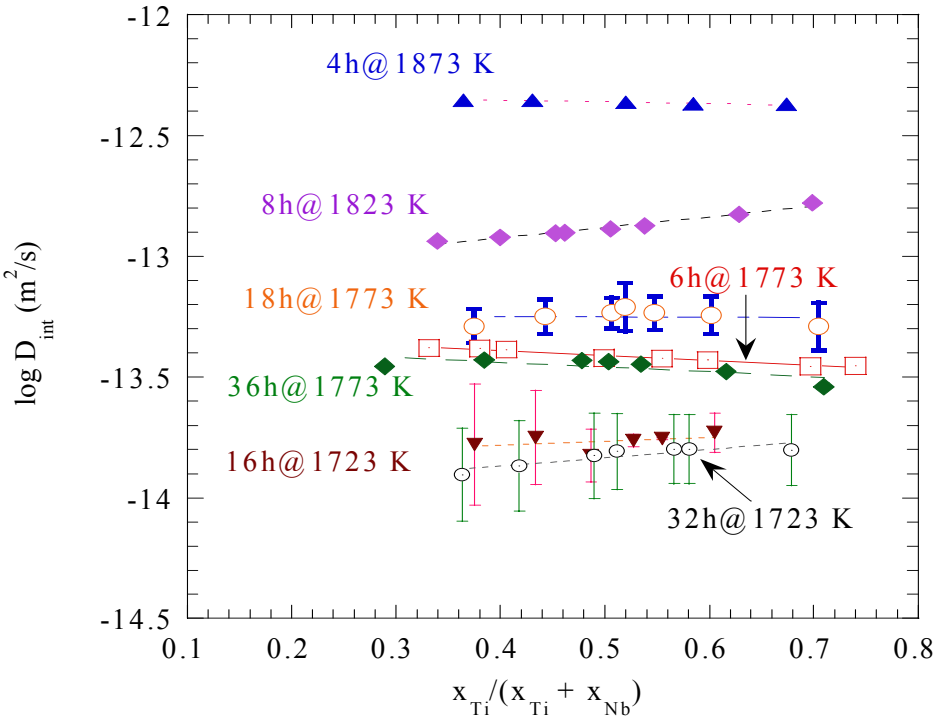

Figure A.5: Dependence of D_{int} on $x_{Ti}/(x_{Ti} + x_{Nb})$ in the 1723–1873 K temperature range.

Table A.2 lists the interdiffusion coefficients at the Matano interface determined herein. At the Matano interface, the concentrations of Ti, Nb and Al in mol. %, - determined by EDS - were 34±3, 34.1±2 and 32±2, viz. ≈ $(Ti_{0.5},Nb_{0.5})_2AlC$.

Table A.2 The time/temperature range and the corresponding values of the diffusion coefficients at the Matano interface for the 211 system.

Temp. (K)	Time (h)	log D_{int} (m^2/s) (at B-M)
1873	4	-12.36±0.04
1823	8	-12.9±0.05
1773	6	-13.43±0.05
1773	18	-13.24±0.1
1773	36	-13.27±0.05
1723	16	- 13.76±0.03
1723	32	-13.8±0.15

Most intriguingly, as shown in Fig. A.6, the concentration profiles obtained at 1873 K showed the penetration of *only* Ti into the Nb_2AlC matrix (the Matano interface is marked by vertical dashed line); the Nb did *not* penetrate into the Ti_2AlC matrix. Similar behavior was observed at 1823 K.

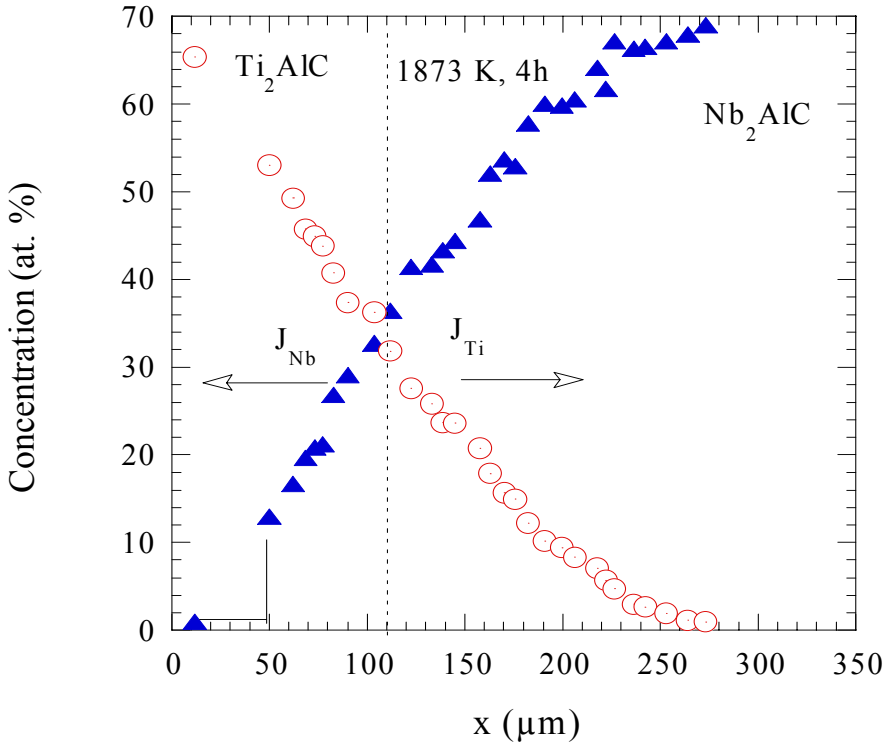

Figure A.6: Nb (blue) and Ti (red) concentration profiles obtained after annealing at 1873 K for 4h. The mechanical interface, located at ≈ 50 μm, does not correspond to the Matano interface.

The penetration depth of Ti in the Nb_2AlC matrix scaled, as expected, with the square root of time at 1873 K (140 μm after a 4 h run; 260 μm after 16 h) and was marked by the formation of a localized Nb-Al-C layer deep in the Nb_2AlC matrix (Fig. A.7a). The diffusion coefficient of Nb, based on the position of this layer from the original interface was calculated to be $(1.3\pm0.1) \times 10^{-12}$ m^2/s. Note that in Fig. A.6, for reasons that are not clear, the mechanical interface, located at ≈ 50 μm, does not correspond to the Matano interface. Figure A.7 b shows etched OM micrographs of the interface after annealing at 1873 K for 4 h. The white layer is TiC_x that results from the dissociation of Ti_2AlC by the loss of Al.

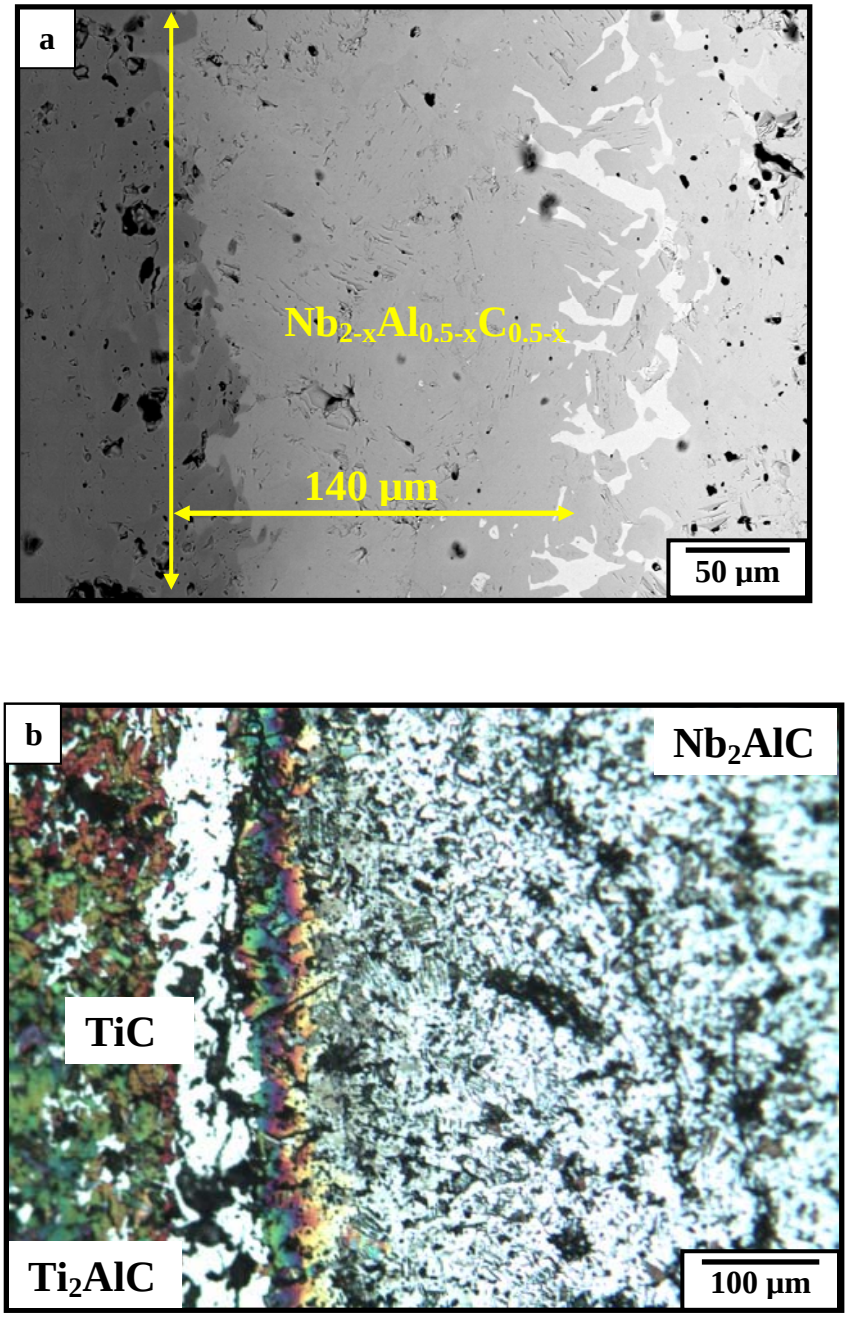

Figure A.7 (a) Backscattered SEM micrograph of a Ti_2AlC-Nb_2AlC diffusion couple annealed at 1873 K for 4 h showing the formation of localized layer $Nb_{2-x}Al_{0.5-x}C_{0.5-x}$ (b) Etched OM micrograph of the same couple. The thick white layer is TiC_x that forms as a result of Al loss from Ti_2AlC.

It appears that even though the Ti atoms are mobile enough to penetrate the TiC_x layer barrier and diffuse into the Nb_2AlC matrix, the Nb atoms are not. It thus appears that the following reaction could be occurring:

$$x\ Ti + (1.5 - x)\ Nb_2AlC = (Ti_{x/2},Nb_{(1-x)/2})_2AlC + Nb_{2-x}Al_{0.5-x}C_{0.5-x} \quad (A.2)$$

The exact C-content of the Nb-Al-C layer that forms is difficult to quantify. The Nb/Al ratio was found to be 58±3:35±1. Note that in this case, the Nb is rejected from the interface and accumulates deep in the Nb_2AlC phase. In other words, the Nb is diffusing up its concentration gradient.

As noted above, at 1723 and 1773 K, symmetric diffusion is observed. In this case a localized Nb-Al-C layer is also observed but near the original interface. At that location the Ti content of the Nb-Ti 211 solid solution is relatively high (~ 20 at. %). A possible reaction could be:

$$Ti_2AlC + x\ Nb_2AlC = (Ti,Nb)_2AlC + Nb_{2x-2}Al_xC_x \quad (A.3)$$

Here again the exact C-content of the Nb-Al-C layer that form is difficult to quantify. The Nb/Al ratio, however, was found to be 25.5±0.4:71±1. In this case, no dissociation of the Ti_2AlC was observed and subsequently there was no formation of TiC_x at the interface. This observation signifies that Ti_2AlC is stable up to 1773 K in a vacuum atmosphere at least up to 36 h.

A.5 Arrhenius Plot for 312 and 211 systems

A linear regression fit to an Arrhenius plot of D_{int} at the Matano interface in the 312 system (Fig. 8.8) results in the following expression:

$$D_{\text{int}}(m^2/s) = 0.3 \pm 0.2 \exp \frac{-350 \pm 3\,(kJ/mol)}{RT} \tag{A.4}$$

where R and T have their usual meanings. Figure 3 also plots the diffusion coefficient of Si in $TiSi_2$ reported in literature [112-115]. And while the absolute values of diffusivities are comparable at the lower temperatures, the activation energies obtained here are greater by a factor of between 1.6 to 2.3.

The Arrhenius plot of D_{int} at the Matano interface for 211 system (Fig. A.8) is expressed by:

$$D_{\text{int}}(m^2/s) = (12 \pm 3) \times 10^3 \exp \frac{-591 \pm 5\,(kJ/mol)}{RT} \tag{A.5}$$

At 1773 K, the absolute values of interdiffusion coefficients of the A group elements are ≈ 7 times higher than those of the M group. Similarly, the activation energies for the diffusion of the M-elements are greater by a factor of 1.7. Both observations indicating that M-X bonds are stronger than the M-A bonds as indirectly surmised from other types of experiments [105, 106].

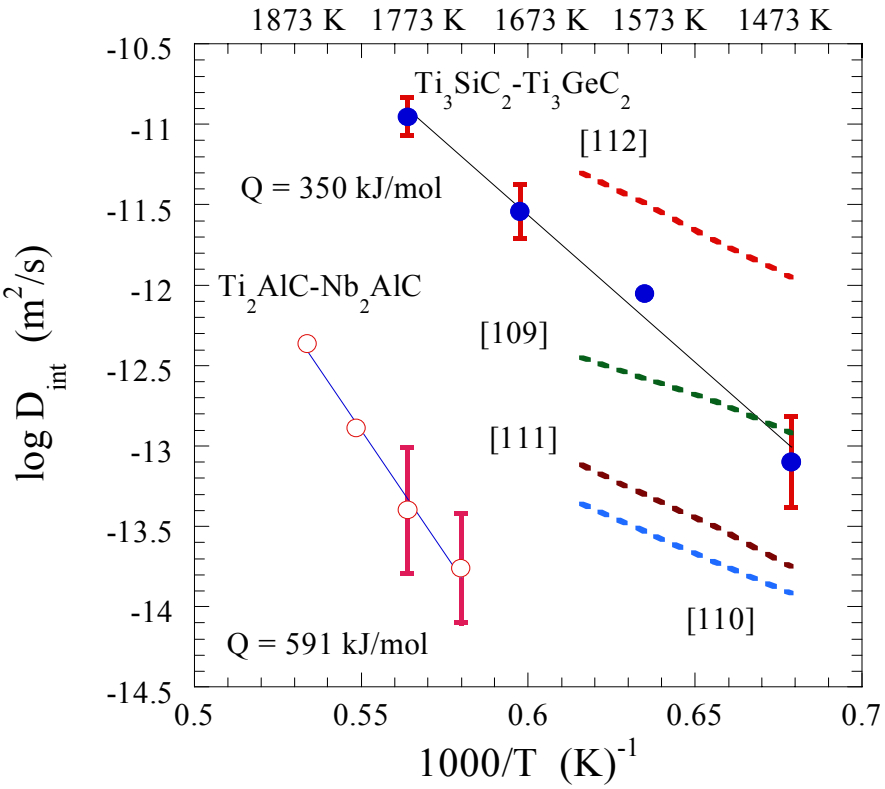

Figure A.8: Arrhenius plot of the interdiffusion coefficient, D_{int}, at the Matano composition ≈ $Ti_3Ge_{0.5}Ge_{0.5}C_2$ for 312 and ≈ $(Ti_{0.5}, Nb_{0.5})_2AlC$ for 211 system, respectively. Also shown are the Si diffusion coefficients in $TiSi_2$ reported in literature [109-112].

A.6 Conclusions:

Based on the concentration profiles obtained herein, it appears that that Ti_3SiC_2-Ti_3GeC_2 form a complete range of solid solutions, between 1473 to 1773 K and Ti_2AlC-Nb_2AlC also form a complete range of solid solutions, between 1723 to 1773 K temperature ranges. At comparable temperatures, the absolute values of the

diffusivities of the A group elements are found to be ≈ 7 times higher than those of the M group element. The activation energies for the diffusion of the M-elements are also greater by a factor of 1.7. Both observations indicating that the M-X bonds are stronger than the M-A bonds.

Appendix B: Synthesis of $Ti_3(Al_{1.0}Sn_{0.2})C_2$

To fabricate Ti_3AlC_2 powders, Ti (-325 mesh, 99.5 %, Alfa Aesar, MA), Al (-325 mesh, 99.5 %, Alfa Aesar, MA) and graphite (- 300 mesh, 99%,, Alfa Aesar, MA) powders were mixed with Sn (-325 mesh, 99.8%, Alfa Aesar, MA) to result in a $Ti_3AlSn_{0.2}C_2$ nominal composition. The powders were ball milled, and then placed in a graphite-element heated vacuum furnace, heated at ≈ 500 °C/h up to 1400 °C and held at that temperature for 1 hr. The resulting powders were predominantly single phase.

Vita

Adrish Ganguly

DOB: 03/30/1976

Citizenship: India

Education

Ph.D. in Material Science & Engineering, Drexel University, Philadelphia, PA, February 2006.

B.Sc. in Ceramic Science and engineering, College of Ceramic Technology, Government of West Bengal, University of Calcutta, July 1999.

Experience

Graduate Research Fellow, Dept. of Materials Engineering Drexel University, Philadelphia, PA, August 2001- present.

Guest Researcher, PML, Max Planck Institute fur Metallforschung, Stuttgart, Germany, March-July, 2001.

Publications

Nine peer reviewed journal papers and twelve conference presentations.